Advances in geoarchaeological site formation research by integrating geophysical methods, direct push sensing techniques and stratigraphic borehole data

- case studies from central Europe and the western Peloponnese around ancient Olympia -

---

Dissertation

zur Erlangung des Grades

Doktor der Naturwissenschaften

im Promotionsfach Geographie

am Fachbereich Chemie, Pharmazie und Geowissenschaften

der Johannes Gutenberg-Universität Mainz

Lea Marit Obrocki

geb. in Gießen

Mainz, April 2019

Berichterstatter
1. Gutachter
2. Gutachter

Tag der mündlichen Prüfung:
17. Juni 2019

Abstract

Knowledge on the structure and spatial distribution of near surface sediments is essential for geoarchaeological research. The local sedimentary record preserves information on past landscape formation processes, climate evolution and human-environment interactions. Therefore, the application of different geo-scientific methods for the analysis of such geoarchives enables the reconstruction of palaeoenvironmental conditions for different time slices. The PhD thesis at hands presents a multi-methodological approach for geo-scientific research combining non-invasive geophysical and minimal-invasive direct push (DP) methods with standard sediment coring. The information value of these methods is discussed at the example of four case study sites. As main research topics differ from each case study, the methodological spectrum is adjusted correspondingly. In particular, the questions are clarified how the joint interpretation of different methods facilitate data processing and how obtained DP results may help to simplify tracing specific sediment signatures and deciphering geomorphological characteristics. Furthermore, the thesis deals with the issue how geophysical models can be improved by the integration of high-resolution DP data.

In the framework of the first case study, electrical resistivity tomography (ERT) was carried out to detect and localize Mycenaean chamber tombs at three different locations in the surrounding of ancient Olympia (western Peloponnese, Greece). ERT data were first calibrated based on specific ERT signals of known and partly excavated chamber tombs at the Mycenaean necropolis of Mageiras-Kioupia. In a second step, calibrated ERT procedures were used to identify the position of unknown chamber tombs at two different other sites. ERT measurements were supplemented by ground penetrating radar (GPR) at the Epitalio site. Based on the combination of GPR and calibrated ERT data, a most probably Mycenaean cemetery consisting of a number of buried chamber tombs was localized at the Epitalio site. In contrast, ERT data helped to recognize that there are no chamber tombs at the Dartisa plateau as assumed before.

The novel application of DP techniques in Geoarchaeology and Quaternary Science is shown by the example of investigations in a floodplain area in central Europe and two lagoonal environments in the western Peloponnese. The joint interpretation of ERT data, sediment core data and *in situ* DP electrical conductivity (DP EC) data at Großkrotzenburg (River Main, Central Europe) allowed the reconstruction of the local palaeotopography and estimation of a possible Roman harbour situation at the floodplain of the River Main at Großkrotzenburg (Hesse, Germany). Furthermore, the application of DP EC and sediment coring reveals that the overall floodplain evolution was mainly controlled by flood events. Two periods of major flooding were found, namely during late Medieval (1435-1484 cal AD) and Modern times (1646-1792 cal AD). These periods are chronologically highly consistent with the AD 1480, AD 1573 and AD 1784 flood events known by historical reports.

The methodological spectrum was complemented by using the direct push hydraulic profiling tool (DP HPT) and direct push cone penetration tests (DP CPT) within two case studies at the shores of the Gulf of Kyparissia (western Peloponnese, Greece). The Gulf of Kyparissa is directly exposed to the Hellenic Arc and Trench system and therefore represents one of

the seismically most active regions in Europe. Geomorphological and sedimentary signatures of past tsunami impacts were found within previous studies focusing on the Kaiafa Lagoon (Koster et al. 2015) and the former Mouria Lagoon (Willershäuser et al. 2015a). Using an advanced menthodological approach, DP measurements were now carried out at both sites to test the usability of DP data for tracing high-energy sediment layers. Both, DP HPT and DP CPT data, revealed *in situ* high-resolution stratigraphic information of allochthonous sand sheets. Furthermore, DP data allowed the detection of erosional contacts, fining upward sequences and rip up clasts. These sedimentary signatures are related to high-energy tsunami sediment transport. Moreover, DP data showed two separate tsunami impulses. Radiocarbon age control at the Kaiafa lagoon allowed the identification of these tsunami layers as candidates for the AD 551 and AD 1303 earthquake and tsunami events. Based on regression analysis between DP and grain size data, DP data were used to trace sand sheets along transects, hundreds of meters long. Finally, DP data were combined with surface-based geophysical data. At the Kaiafa Lagoon, the integrated interpretation of DP HPT, DP CPT and ERT allowed the projection of point information to spatial dimensions. At the former Mouria Lagoon, seismic CPT (DP SCPT) data were coupled with surface-based seismic reflection data resulting in a depth conversion of seismic profile data. In this way, seismic reflection data was depth-correlated with DP parameters and grain size distribution so that the sedimentary subsurface architecture could be interpreted even beyond the maximum coring depth.

The results of the present PhD study underline that the application of a multi-methodological approach in geo-scientific research strongly improves our understanding of site formation processes within space and time. Further, the use of DP techniques within the framework of sedimentological and geomorphological investigations is documented by the analysis of single DP parameters, a statistical combination of DP and sedimentary data and the integration of DP data in surface-based geophysical models. The diversity of the DP methods as well as integrated geophysical and geochemical parameters significantly increase the precision of stratigraphic data. If DP data is once calibrated by sediment core data, combined DP techniques allow for a cost- and time-efficient collection of large stratigraphic data sets.

Zusammenfassung

Für die Geoarchäologie und Quartärforschung sind Kenntnisse über die Struktur und räumliche Verteilung der oberflächennahen Sedimente unerlässlich. Die Sedimentabfolge speichert Informationen über landschaftsformende Prozesse, die Entwicklung des Klimas und die Interaktion zwischen Menschen und Umwelt. Der Einsatz von geowissenschaftlichen Methoden zur Analyse eines solchen Geoarchives ermöglicht es daher, Paläoumweltbedingungen zu verschiedenen Zeitscheiben zu rekonstruieren. Die vorliegende Dissertation stellt einen multimethodischen Ansatz vor, bei dem nicht-invasiven geophysikalische und minimal-invasiven Direct Push (DP)-Methoden mit klassischen Bohrungen kombiniert werden. Die Aussagekraft der unterschiedlichen Methoden sowie in ihrer Kombination wird anhand von vier Fallbeispielen mit unterschiedlichen geowissenschaftlichen und geoarchäologischen Fragestellungen diskutiert. Das Methodenspektrum wurde daher an den jeweiligen Forschungsschwerpunkt angepasst. Insbesondere sollen die Fragen geklärt werden inwieweit die Kopplung unterschiedlicher Methoden die Datenauswertung erleichtert und inwieweit DP Technologien die Detektion spezifischer Sedimenteigenschaften und geomorphologischer Merkmale im Untergrund erleichtern. Darüber hinaus beschäftigt sich die Arbeit mit der Möglichkeit zur Verbesserung der Datenverarbeitung durch die Integration hochaufgelöster DP Daten in geophysikalische Modelle.

Im Rahmen der ersten Fallstudie wurden geoelektrische Widerstandsmessungen (*electrical resistivity tomography*, ERT) zur Detektion und Lokalisierung von mykenischen Kammergräbern an drei Standorten in der Umgebung des antiken Olympias (westliche Peloponnes, Griechenland) durchgeführt. Die ERT Daten wurden zunächst anhand von bekannten und teilweise ausgegrabenen Kammergräbern der mykenischen Nekropole in Mageiras-Kioupia kalibriert. Die kalibrierten ERT Daten dienten der Lokalisation bislang unbekannter Kammergräber an zwei weiteren Standorten. Das Methodenspektrum wurde in Epitalio durch den Einsatz von Bodenradar (*ground penetrating radar*, GPR) Untersuchungen ergänzt. Die Kombination aus GPR und kalibrierten ERT Daten ermöglichte die Prospektion eines wahrscheinlich mykenischen Friedhofs in Epitalio, bestehend aus mehreren Kammergräbern. In Dartisa hingen konnte der Verdacht auf die Existenz von Kammergräbern mit Hilfe der kalibrierten ERT Ergebnissen falsifiziert werden.

Der neuartige Einsatz von DP-Technologien in der Geoarchäologie und Quartärforschung wird am Beispiel von Untersuchungen in einem Auengebiet in Mitteleuropa und zwei Lagunen-landschaften an der westlichen Peloponnes gezeigt. Die Kombination aus ERT Daten, Bohrungen und DP *in situ*-Messung der elektrischen Leitfähigkeit (DP EC) erlaubten die Rekonstruktion der Paläogeographie sowie eine Einschätzung des bestmöglichen Standortes für einen römischen Hafen im Bereich der Mainaue von Großkrotzenburg (Hessen, Deutschland). Weiterhin belegen die Sedimentkerne und DP-Untersuchungen, dass die Landschaftsentwicklung im Bereich der heutigen Mainaue maßgeblich durch extreme Hochwasserereignisse gesteuert wurde. Es konnten zwei Überschwemmungsperioden im späten Mittelalter (1435-1483 cal AD) und der Neuzeit (1646-1792 cal AD) identifiziert werden, welche korrelat zu den historischen Hochwasserereignissen in AD 1480, AD 1573 und AD 1784 sind.

Das Methodenspektrum wurde für die Untersuchungen am Golf von Kyparissia (westliche Peloponnes, Griechenland) durch den Einsatz von hydraulischem Direct Push-Verfahren (*hydraulic profiling tool*, DP HPT) und Direct Push Cone Penetrometer Test (*cone penetration test*, DP CPT) erweitert. Der Golf von Kyparissa gehört, aufgrund seiner direkten Exposition zum Hellenischen Tiefseegraben, zu der seismisch aktivsten Region Europas. Geomorphologische und sedimentologische Belege für Paläotsunami-Ereignisse im Bereich der Kaiafa Lagune (Koster et al. 2015) und der ehemaligen Mouria Lagune (Willershäuser et al. 2015a) konnten durch jüngere Studien erbracht werden. Mit Hilfe eines fortschrittlichen methodischen Ansatzes wurde die Eignung von DP-Methoden für die Identifikation von hochenergetischen Sedimenten am Beispiel dieser beiden Untersuchungsgebiete getestet. Die Ergebnisse zeigen, dass sowohl die DP HPT als auch die DP CPT Daten hochaufgelöste stratigraphische Information liefern, welche bspw. die Mächtigkeit allochthoner Sandlagen abbildet. Weiterhin können basierend auf den DP-Daten basale Erosionsdiskordanzen, nach oben abnehmenden Korngrößenzusammensetzung (*fining upward*) sowie feinkörnige Erosionsgerölle identifiziert werden. Diese sedimentologischen Merkmale können mit der hohen Strömungsdynamik während eines Tsunami-Ereignisses assoziiert werden. Darüber hinaus zeigen die DP Daten zwei trennbare Tsunami-Impulse. Radiokohlenstoffdatierungen aus Sedimentbohrungen der Kaiafa Lagune belegen, dass der Zeitraum tsunamigener Überschwemmung mit hoher Wahrscheinlichkeit mit den Tsunami- und Erdbeben-Ereignissen in AD 551 und AD 1303 in Verbindung steht. Basierend auf einer Regressionsanalyse von DP Daten und Korngrößenzusammensetzung konnte die Sandalge entlang von Transekten über mehrere hundert Meter hinweg verfolgt werden. In einem letzten Schritt wurden die DP Daten mit oberflächenbasierten geophysikalischen Daten kombiniert. An der Kaiafa Lagune erlaubte die integrierte Interpretation von DP HPT, DP CPT und ERT Ergebnissen eine Übertragung der punktförmigen Information der Sedimentabfolge in die Fläche. Im Bereich der ehemaligen Mouria Lagune wurde die oberflächenbasierte Reflektionsseismik mit einer Messung des seismischen CPTs (DP SCPT) gekoppelt. Dies erlaubte eine Zeit-Tiefen Tranformation der seismischen Laufzeiten. Auf diese Weise ist eine tiefen-exakte Korrelation der seismischen Profildaten mit DP-Daten und Korngrößenzusammensetzung gelungen, so dass die räumliche Verteilung von Sedimentstrukturen bis in Tiefen unterhalb der maximalen Bohrteufe interpretiert werden konnte.

Die Ergebnisse dieser Dissertation zeigen, dass ein multimethodischer Ansatz das Verständnis von landschaftsverändernden Prozessen in Raum und Zeit deutlich steigert. Der Nutzen von DP Verfahren für sedimentologische und geomorphologische Untersuchungen konnte anhand detaillierter Analysen der einzelnen DP Parameter, einer statistischen Auswertung kombinierter DP und sedimentologischer Daten sowie der Integration von DP Daten in oberflächenbasierte geophysikalische Modelle bestätigt werden. Desto vielfältiger das Spektrum der DP Methoden und damit geophysikalischer und geochemische Parameter ist, je präziser kann eine stratigraphische Interpretation der Daten durchgeführt werden. Wenn DP-Daten einmal mit Hilfe von sedimentologischen Daten kalibriert wurden, ermöglicht der Einsatz kombinierter DP Technologien eine schnelle und kosteneffektive Datenerhebung stratigraphischer Datensätze.

Table of contents

List of figures

List of tables

1. Introduction

1.1 Advanced geophysical approaches and sediment studies in Geoarchaeology and Quaternary Sciences

Geoarchaeology describes a variety of research fields applying geoscientific methods within archaeological contexts. The main issue is to improve our understanding of site formation processes and environmental evolution within the complex system of man-environment interactions (Waters 1992, Rapp & Hill 1998). Thereby, aspects of Quaternary Geology and Geography (including Physical and Human Geography, Geomorphology, Biogeography, Geoecology) are combined with aspects of Archeology and History (Rapp & Hill 1998, Brückner 2007, Brückner & Vött 2008). The Quaternary is characterized by global environmental changes that mainly formed the present landscapes (Holliday 2001, Leser 2009). Moreover, the Quaternary spans the time of human evolution pending the development of modern cultures and societies (Holliday 2001). Therefore, the subject of Geoarchaeology is the complex interrelation of human and environment and the reconstruction of palaeolandscapes. This includes natural processes of landscape formation (e.g. climatic variations, tectonic movements, sea level changes, extreme events) and direct as well as indirect anthropogenic forces on landscape changes (e.g. river regulation and harbour installations, soil erosion and increased flood risk) (Frederick 2001, Goldberg & Macphail 2006, Herget 2007). Furthermore, landscape reconstruction is crucial to connect cultural, economic and social evolution with natural factors (Schröder & Hauptmann 2008). Geoarchaeology gained increasing recognition already in the 1960s but it is only since the 1980s and 1990s that Geoarchaeology has taken over an important and steadily increasing role in Physical Geography and Geosciences (Rapp & Hill 1998, Shahack-Gross 2017). During the past decades, numerous scientific articles were published combining archaeological and geo-scientific research (e.g. Stein 2001, Eitel 2006, Dikau et al. 2007, Morley & Goldberg 2017, Herget 2017, Goldberg & Aldeias 2018).

The analysis of near surface sediments allows for the reconstruction of palaeoenvironmental conditions as the sedimentological record of a certain area preserves different signals reflecting geomorphological dynamics, soil formation processes, vegetation changes and climate conditions (Brückner 2007, Dikau et al. 2007, Wunderlich 2007). Thus, knowledge of the spatial distribution of different sediment types is essential for site characterization and the identification of effects triggering landscape changes. According to the specific issue to be addressed in this study, different geomorphological, sedimentological and geophysical methods can be used to analyse varying geoarchives. A general distinction is made between non-invasive geophysical methods and minimal-invasive logging techniques such as sediment coring or direct push (DP) logging (e.g. Dietrich & Leven 2006, Goldberg & Macphail 2006, Schrott & Hecht 2007, Bumberger et al. 2015).

Sediment coring (manual or mechanical drilling) allows for an exploration of the near surface with a nearly gapless vertical resolution for the existing material (Bumberger et al. 2015). Thus, layer boundaries of different sediment units can be derived exactly within the overall stratigraphic record. Furthermore, this method enables sampling of sediments, organic material or artifacts embedded in the sediment, for additional sedimentological,

geophysical, geochemical or geochronological analysis necessary for facies interpretation and the development of chronostratigraphies (e.g. Vött et al. 2006, Kadereit et al. 2006, Brückner 2007, Goldberg & Macphail 2008, Wunderlich et al. 2012). However, sediment coring commonly used for site characterization has some disadvantages. In case of a complex and heterogeneous underground, it is very cost-intensive and time-consuming to cover all sediment structures by a large number of sediment cores (performing coring transects or grids). Moreover, standard coring applications entail the risk of sediment contamination and compaction during the drilling process. Therefore, correlation of adjacent sediment sequences might be difficult, especially when corresponding sediment sections are missing due to core loss (Hausmann et al. 2018).

The application of direct push (DP) *in situ* sensing can significantly improve our understanding of site formation processes studied within the framework of Quaternary and geoarchaeological research (Leven et al. 2011). DP techniques provide the acquisition of several parameters with high depth accuracies in a cm-scale (Dietriech & Leven 2006, Demuth et al. 2015, Hausmann et al. 2018). Beside the high-resolution of data collection, DP logging is the most direct form to record stratigraphic data since the disturbance of stratigraphic information is reduced to a minimum (Fischer et al. 2016a, Wunderlich et al. 2018a). Different sensors are mounted directly at the tip or near the tip of a direct push probe constantly measuring e.g. tip resistance, sleeve friction, electrical resistivity, shear wave velocities, water injection pressure, fluorescence quantum, gamma radiation, wavelength of specific intensities or an image signal (Bumberger et al. 2005, Leven et al. 2011, Demuth et al. 2015). DP techniques have commonly been used for geotechnical and hydrogeological issues as they allow for the estimation of different sediment and soil types and material consolidation (Lunne et al. 2002, Köber et al. 2009, Leven et al. 2011, Hausmann 2013). Despite the high potential of DP data for stratigraphic and sedimentological investigations, this method has only been rarely applied in geomorphological (Amorosi & Marchi 1999, Schmelzbach et al. 2011, Styllas 2014) and geoarchaeological studies (Koster et al. 2016, Fischer et al. 2016a, Hausmann et al. 2018, Wunderlich et al. 2018a, Hadler et al. 2019). However, the efficiency of DP techniques is clearly shown by some studies. For example, Fischer et al. (2016a) showed the strong correlation between grain size and DP electrical conductivity (DP EC) data. Missiaen et al. (2015) and Hausmann et al. (2018) present a detailed reconstruction of prehistoric palaeotopographies using Cone Penetration Testing (DP CPT) in combination with DP EC and colour logging, respectively. Compared to standard coring procedures, DP sensing is time-saving and the maximum investigation depth can be increased (Leven et al. 2011, Fischer et al. 2016a). Therefore, the application of DP techniques clearly allows the reduction of the number of sediment cores required for collecting data in a complex setting as the relevant sediment units can be easily mapped by DP logging. However, coring and DP sensing provide only point information with regard to the stratigraphy at the study site (Dietrich & Leven 2006, Hausmann 2013, Wunderlich et al. 2018a). As mentioned above, further stratigraphic information can be collected by time- and cost-efficient DP sensing. Wunderlich et al (2018a) suggest at least five DP EC logs with a maximum space of 24 m to interpolate layer boundaries derived from DP EC logs for a case study near ancient Ostia. However, considering small-scale

stratigraphic variations or the detection of buried archaeological structures, a combination of direct (minimal-invasive) and non-invasive surface-based geophysical methods is favorable (Dietrich & Leven 2006).

Shallow geophysical methods help to detect different geophysical parameters such as the dielectric constant, electrical resistivity or wave velocities revealing layer boundaries or anomalies within the subsurface. These parameters can give straight-forward lithological information but may also document different water contents and/or changes in salinity and density (Schrott & Hecht 2007, Schrott & Sass 2008). Therefore, the calibration of geophysical data derived from coring or comparable stratigraphic information is highly recommended (Schrott & Hecht 2006, Fischer et al. 2016a, Wunderlich et al. 2018b). By this, for instance the thickness of sediment packages of interest or the bedrock topography can be assessed. Additionally, natural structures (e.g. course and extent of river channels, fault zones) as well as buried artificial structures can be detected prior to archaeological excavations (e.g. Casten 2008, Hausmann et al. 2013, Vött et al. 2015, Finkler et al. 2018a, Hadler et al. 2018). However, the use of non-invasive geophysical methods always depends on local site-specific factors. For example, seismic prospection provides a higher penetration depth and structural resolution compared to other methods. However, the successful detection of seismic waves depends on the increase in density with each consecutive underlying sediment layer and data acquisition and interpretation is more complex (Schrott & Sass 2008, Rabbel 2006). Furthermore, the presence of torrents, strong wind or rainfall or nearby road traffic may prevent the detection of seismic waves due to background noise in the seismic record. Ground Penetrating Radar (GPR) is well suited to distinguish between different sediment units of varying origin. However, the penetration depth of GPR measurements is often limited in wet, silty or clayey material due to high attenuation values, also documented by increased electrical conductivity. Moreover, the application of GPR measurements in forests is not advisable due to air wave reflection in the root zone that cannot always be differentiated from ground information. A great advantage of Electrical Resistivity Tomography (ERT) measurements is the flexible usability in different types of terrains regarding topography, subsurface conditions and vegetation cover. A high variability in penetration depth and resolution can be chosen according to the aim of research (Schrott & Sass 2008). However, the resolution of ERT measurements decreases with increasing depth and an exact detection of layer boundaries and thin layers is rarely possible (Fischer et al. 2016a). Therefore, combining different non-invasive methods and stratigraphic information deduced from sediment cores has become state of the art for landscape reconstructions to overcome the limitations and to verify and cross-check the results of each individual method (Bates et al. 2007, Hausmann et al. 2013, Van Dam 2012, Rabbel et al. 2015, Hausmann et al. 2018).

A step forward in the methodological development is the combination of surface-based geophysical models and sediment coring with DP logging to improve the data processing of geophysical models (Bates et al. 2007, Werban et al. 2007, Paasche et al. 2009, Fischer et al.

2016a, WUNDERLICH et al. 2018a, 2018b).

1.2 Study aims and research outline

The present study focuses on the joint application of non-invasive and minimal-invasive methods within the framework of different case studies. Based on four different types of geoarchives, the PhD thesis at hands deals with the following study aims:

(i) to select site-specific geophysical methods and combine surface-based geophysiacal prospection with DP in situ logging,

(ii) to improve knowledge on stratigraphic architecture by the qualitative and quantitative (statistic) use of DP data,

(iii) to integrate DP data into geophysical approaches,

(iv) to identify the best-possible idea of site formation processes based on geophysical and DP approaches, and

(v) to evaluate the application of DP techniques in Geoarchaeology and Quaternary Sciences – pros and cons.

Tab. 1.1 shows an overview of non-invasive and minimal-invasive methods used in this thesis. Due to the easy applicability in different types of terrains and the fast mapping of relevant near surface structures, ERT measurements were used at every study site as a tool for initial site characterization. Furthermore, the application of ERT allows onsite decision for the selection of further surface-based geophysical methods depending on site conditions and specific objectives. Moreover, the direct access to ERT depth sections in the field enables the estimation of maximum coring depth and appropriate logging sites for detailed direct explorations. Following this approach, the required number of minimal-invasive investigations can be estimated to collect a representative data density at each study site. Based on calibration of DP logs by sedimentary information derived from traditional drilling, DP techniques are used to analyze the sedimentary record for wide areas and to detect small-scale heterogeneities within the stratigraphy. In addition, integrated data interpretation of surface-based geophysical data coupled with DP *in situ* information are tested within the current study.

The thesis is divided in three main chapters, each of which presents a separate paper published in international journals. The methodological spectrum was selected according to the specific research issue and consequently enlarged from Chapter 2 to Chapter 5. Chapter 2 provides a surface-based geophysical approach to differentiate between natural bedrock material and man-made chamber tombs in the surroundings of ancient Olympia (western Peloponnese, Greece). ERT data were calibrated by the physical signal of known chamber tombs at a Mycenaean necropolis. It was also possible to distinguish between intact and collapsed cavities based on geophysical measurements. In a second step, the potential of collected data to detect unknown cemeteries and to estimate the size of buried chamber tombs is discussed in detail.

	Prospection Method	Measured Parameter	Interpretation	References (selected)
Non - invasive methods	Electrical Resistivity Tomography (ERT)	apparent electrical resistivity	sediment composition, sediment thickness, internal structure, differentiation of air filled cavities and soild rocks, archaeological remains	Berktold et al. 2005, Ernstson & Kirsch 2006, Hecht 2007, Ullrich et al. 2007, Schrott & Sass 2008, Wunderlich et al. 2013
	Ground Penetrating Radar (GPR)	electromagnetic pulse relfection	sediment composition, sediment thickness, layer boundaries, differentiation of air filled cavities and soild rock, archaeological remains, aqifers	Blindow 2006, Conyers 2013, Harry 2008, Kwamme 2001, Van Dam Schlager 2000
	Seismic	compressional wave velocity (V_P), shear wave velocity (V_S)	sediment thickness, internal structure, differentiation of air filled cavities and soild rocks, elastic behavior, archaeological remains, aquifers	Casten 2008, Hecht 2007, Rabbel 2006, Rabbel et al. 2016, Schrott & Sass 2008
Minimal - invasive methods	Sediment Coring	sediment type and related analysis (e.g. grain size, mineralogical composition, chemical composition, water content, palaeontological analysis)	layer boundaries, sediment genesis, facies determination,	Barsch et al. 2000, Goldberg & Mcphail 2006, Leven et al. 2011, Schreiner & Kreysing 1998, Vött et al. 2002
	Electrical Conductivity Logging (DP EC)	electrical conductivity	sediment composition, clay mineral content, sediment thickness, layer boundaries, aquifers	Campanella & Wemees 1990, Bumberger et al. 2005, Fischer et al. 2016a, Dietrich & Leven 2006, Harington & Hendry 2005, Leven et al. 2011, Schulmeister et al. 2003
	Hydraulic Profiling Tool (DP HPT)	electrical conductivity, hydraulic pressure, water injection rate, hydraulic conductivity	sediment composition, layer boundaries, aquifers, static ground water level	Dietrich & Leven 2006, Dietrich et al. 2008, Geoprope 2015, Körber et al. 2009, Lessoff et al. 2010, McCall et al. 2010, 2011, 2014
	(Seismic) Cone Penetration Testing (DP SCPT)	tip resistance, sleeve friction, pore pressures, compressional wave velocity (V_P), shear wave velocity (V_S)	sediment composition, layer boundaries, elastic behavior, variations in consistency bulk density	Baginska et al. 2013, Bumberger et al. 2005, Eslami & Fellenius 2004, Lunne et al. 2002, Robertson et al. 1990, 2009, 2016, Robertson et al. 1986

Tab. 1.1: Overview of applied methods including surface-based geophysical methods, sediment coring and direct push techniques.

Chapter 3 deals with the floodplain evolution and the localization of a harbour situation associated with the Roman fort at Großkrotzenburg (Hesse, Germany, central Europe). The reconstruction of the palaeogeography is realized by applying a range of geo-scientific methods. Effects of historical floods and man-made river regulation on the preservation of

stratigraphic information and archaeological artifacts are presented and discussed.

In Chapter 4 a methodological investigation is presented with regard to the applicability of DP techniques to detect sediment layers associated with tsunami impact at the Gulf of Kyparissa. The section is divided in two case studies. The first is located at the eastern shore of the Kaiafa Lagoon and the second in the area of the former Mouria Lagoon. At both sites, the potential of DP techniques to recognize small-scale features of high-energy sediment transport within the sediment record is evaluated. DP data were then coupled with surface-based geophysical data to assess the extension of tsunami inundation at the Kaiafa Lagoon and to improve data processing and interpretation by coupling non-invasive and borehole seismic data at the former Mouria Lagoon.

In Chapter 5, the main results of the research chapters (Chapters 2 to 4) are summarized and discussed. An evaluation of combined non-invasive and minimal-invasive methods and in particular the integration of DP techniques for site characterization and data processing is given. Also, the chapter demonstrates perspectives of the application of DP *in situ* sensing in Geoarchaology and Quaternary Sciences beyond the scope of the PhD thesis at hands.

Chapter 6 gives a summary and final conclusions on the findings of this thesis.

1.3 The study areas

The necropolis of Mageiras-Kioupia (western Peloponnese, Greece) came to light in 2007 when widespread fires burnt the area. Until 2010, eight chamber tombs, carved into the local bedrock, were found by the responsible Ephorate of Antiquities at Olympia. Most of these tombs are nowadays excavated and well cleaned but some are still filled with loose bedrock material due to collapsed cavities. Therefore, the key site at Mageiras-Kioupia (Fig. 1.1A) provides perfect conditions to calibrate ERT data as a basis for the detection and localization of further chamber tombs at different sites. This approach was applied to a hill near the village Epitalio and to the so called Dartisa plateau (Fig. 1.1A). Both sites are of high archaeological interest regarding past human activity in the surroundings of the cult site of ancient Olympia which is located only 12 km away. Similar to Mageiras-Kioupia, the Epitalio and the Dartisa sites are characterized by the hilly landscape out of sand- and siltstones belonging to the Vounargon Stage, Upper Pliocene in age (IGME 1982). The selection of these two areas were made based on a previous archaeological survey that gave evidence for human impacts and settlement activities.

The joint interpretation of non-invasive and minimal-invasive methods was tested at a floodplain area of the River Main (Hesse, Germany) and two lagoonal environments in the coastal lowlands of the Gulf of Kyparissa (western Peloponnese, Greece). The Holocene floodplain at Großkrotzenburg is directly connected to a Roman fort built at the edge of the Pleistocene lower terrace of the River Main (Fig. 1.1B). Floodplain areas are the result of both, accumulation and erosional processes and archaeological artifacts are often covered by fluvial sediments, are dislocated or even destroyed by younger fluvial activity. However,

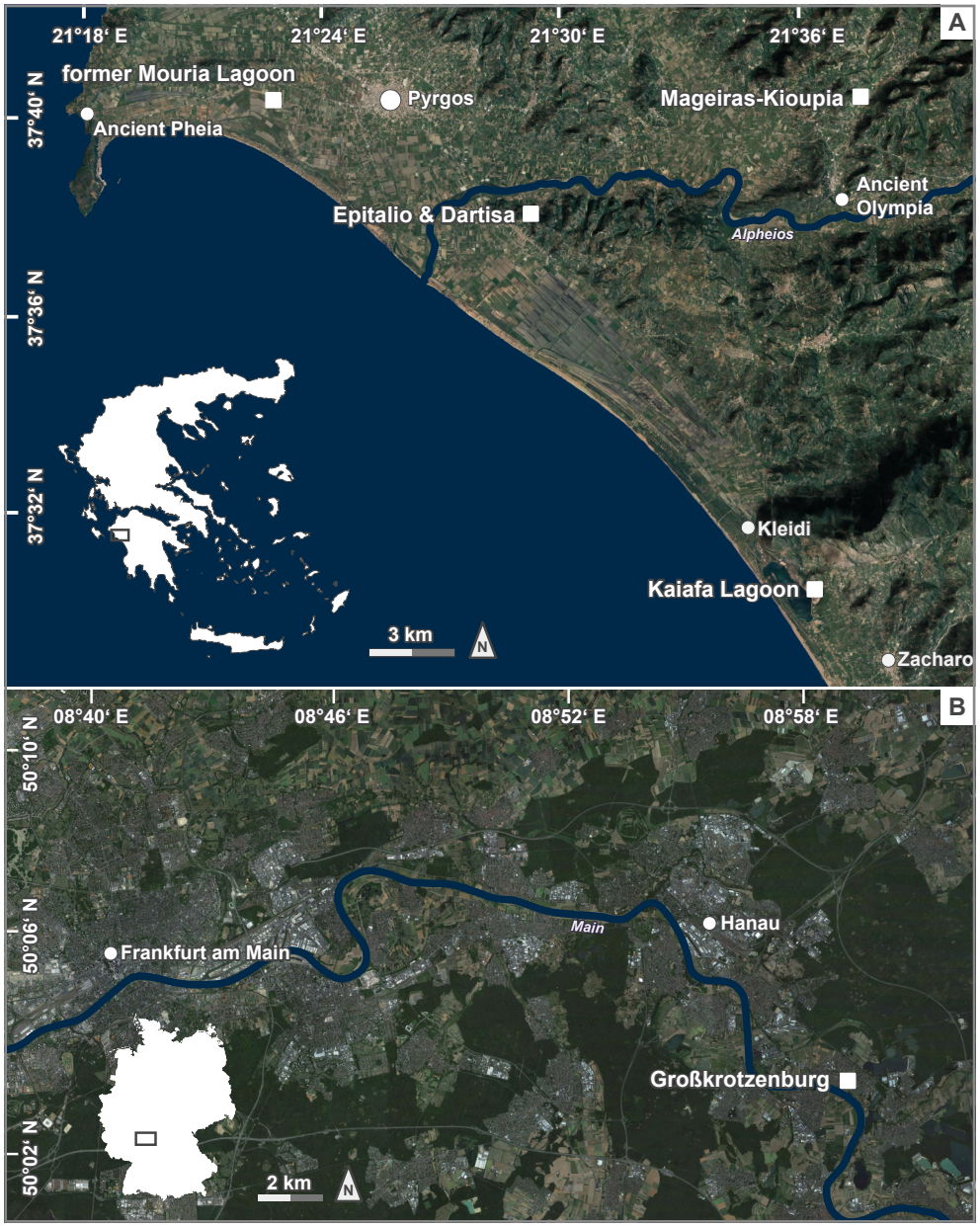

Fig. 1.1: Topographical overview of the study areas. A) Northern Gulf of Kyparissia and the western Peloponnese with the locations of Mageiras-Kioupia, Epitalio and Dartisa (Chapter 2) and the Kaiafa Lagoon and former Mouria Lagoon (Chapter 4), B) Downstream section of the River Main with the location of Großkrotzenburg (Chapter 3).

the sedimentary sequence of a floodplain preserves information on changing environmental conditions allowing for a reconstruction of the palaeolandscape and past fluvial conditions for different time slices (Brown 1997). The archaeological situation of the Roman fort at Großkrotzenburg is well understood since the area has been intensely excavated since the end of the 19th century. The finding of a Roman brick manufacture and the vicinity to the river lead to the assumption that there must have been a harbour site connected to the Roman fort. However, any evidence for harbour installations and knowledge about the environmental

conditions during Roman times are missing so far. Archaeological excavations in wetland areas such as a floodplain are very complicated and costly due to the impact of groundwater (Doran 2013). In contrast, the high groundwater level provides perfect conditions for the use of DP techniques. Moisture content can be neglected within the saturated zone and DP EC values are primally a function of the clay content (Hausmann et al. 2018). Therefore, a cost-efficient and minimal-invasive approach of combined geoarchaological methods was carried out at the floodplain of Großkrotzenburg to understand the floodplain evolution and to search for a preferable harbour situation.

Similar to the Großkrotzenburg floodplain, the geoarchives at the Kaiafa Lagoon and the former Mouria Lagoon are also characterized by high groundwater stands. The Kaiafa Lagoon is located in the coastal lowlands of the southern Gulf of Kyparissia (Fig. 1.1A) close to the Classical acropolis of Samikon and the prehistorical Bronze Age settlement of Kleidi. Thus, landscape formation processes of the wider area are of great geoarchaological interest. The Gulf of Kyparissia is directly exposed to the Hellenic Arc and Trench system and therefore represents one of the seismically most active regions in Europe (Sachpazi et al. 2000, Bonhoff et al. 2005). Recent studies document that repeated tsunami innundation of the coasts of the gulf controlled the landscape evolution during the Holocene (Vött et al. 2011, 2015, 2018a, Röbke et al. 2013, Willershäuser et al. 2012, 2015a, Koster et al. 2015). These findings are supported by the data published by Koster et al. (2015) for the eastern shore of the Kaiafa Lagoon. The authors describe multiple fan-like sand structures as washover fans formed by tsunami impact between 540 cal AD and 1274 cal AD (Koster et al. 2015). Consequently, the Kaiafa Lagoon is an optimal setting to analyze the potential of DP techniques for small-scale sedimentary features such as signatures of high-energy transport. Additional to DP EC measurements, this was tested using DP HPT and DP CPT logging combined with surface-based ERT measurements. DP HPT investigations within the saturated zone provide EC, hydraulic pressure and hydraulic conductivity values as a base to better understand site formation processes (Schulmeister et al. 2003, Sellwood et al. 2005). DP CPT investigations in the saturated zone result in more reliable data (Robertson 2009, 2016).

The former Mouria Lagoon is located at the northern Gulf of Kyparissia between the Kap Katakolo and the mouth of the River Alpheios (Fig. 1.1A). The lagoonal basin has been completely drained since the 1960s and is nowadays intensely used as agricultural land (Pillay 1966). Similar to the Kaiafa Lagoon, the landscape evolution of the former Mouria Lagoon was strongly influenced by several high-energy palaeotsunami events (Willershäuser et al. 2015a). In addition, recent geoarchaological studies indicate that tsunami inundations not only destroyed the nearby ancient harbour of Pheia but even affected the sanctuary of ancient Olympia upstream the River Alpheios (Vött et al. 2011, 2018a, Vött 2013). These findings underline the need of palaeotsunami research to improve our knowledge on tsunami impact especially with regard to risk assessment and risk mitigation. The former Mouria Lagoon was selected to test DP techniques in combination with surface-based seismic measurements. This stratigraphic setting guarantees the increase of density with depth and therefore works as an optimal reflector for seismic investigations.

2 Detection and localization of chamber tombs in the environs of ancient Olympia (Peloponnese, Greece) based on a combination of archaeological survey and geophysical prospection[1]

Abstract. Mycenaean chamber tombs are composed of air-filled burial cavities and therefore can be detected by non-invasive geophysical methods. In this work, an electrical resistivity tomography (ERT)-based approach was used to detect graves at three different sites in the surrounding of ancient Olympia. We collected ERT data at the necropolis of Mageiras-Kioupia, where a number of chamber tombs had already been located and partly excavated, in order to ground-truth the ERT response for chamber tombs in different states of preservation. Near the village of Epitalio, a preceding archaeological survey discovered remains of a chamber tomb in mid-slope position of a larger hill. There, we applied the ERT-approach calibrated at Mageiras-Kioupia to the tomb and detected ten more tomb candidates at this site. In addition to ERT, we carried out ground penetrating radar (GPR) studies. In general, GPR data are highly consistent with ERT results. We were thus able to localize an unknown, most probably Mycenaean cemetery where no systematic archaeological information previously existed. In the third area of investigation, the Dartisa plateau, no potential chamber tomb comparable to the ones excavated and measured at Mageiras-Kioupia and Epitalio were identified.

2.1 Introduction

This study is part of the interdisciplinary Olympia-Area-Survey-Project on the structure, interdependency and change of spatial networks emanating from the cult site of ancient Olympia in order to gain diachronic knowledge of past human activity in this area.

The article will focus on finding traces of ancient burial places. The investigation of tombs has always been an important subject in archaeological studies as they prove specific human presence and activity within an investigated area. Moreover, burial practices mirror social and political structures of the local society (Mee & Cavanagh 1984, Karkanas et al. 2012). In case where ancient tombs are found intact, they often contain burial gifts of great importance, for example weapons, jewelry, vessels, and tools that are related to the social, economic and political background of the buried individuals and their related group (Boyd 2002, Wright 2008, Karkanas 2012). In this context, we investigated three sites of archaeological interest, located in the environs of the lower Alpheios River (western Peloponnese, Greece) with a combination of detailed archaeological survey and geophysical prospection. Non-destructive techniques represent the best possible approach to detect the position of graves and to determine relevant architectural structures as they do not impact the landscape and are very coast- and time-efficient. Geophysical methods provide valuable non-invasive tools to detect the near-surface stratigraphy and subsurface structures such as artifacts and tombs (e.g. Ellwood 1990, Bevan 1991, Butler 2008, Witten 2014, Nero et al. 2016, Sarris et al. 2017, Chen et al. 2018, Malfitana et al. 2018, Deiana et al. 2018a, Tsokas et al. 2018).

[1]This chapter is based on the paper by Obrocki, L., Eder, B., Gehrke, H.-J., Lang, F., Vött, A., Willershäuser, T., Rusch, K., Wilken, D., Hatzi-Spiliopoulou, G., Kolia, E.-I., Vikatou, O. (2019): Detection and localization of chamber tombs in the environs of ancient Olympia (Peloponnese, Greece) based on a combination of archaeological survey and geophysical prospection. – Geoarchaeology, in press: 1-13.

Based on the results of the preceding intensive archaeological survey in the study area, we used electrical resistivity tomography (ERT) techniques to verify already known chamber tombs and to search for unknown tombs in the surroundings of ancient Olympia (Elis, western Greece). The latter was supported by Ground Penetrating Radar (GPR) at one selected site. Both methods are widely used for archaeological prospection and the detection of buried tombs (e.g. Malagodi et al. 1996, Conyers 2006, Tonkov & Loke 2006, Astin et al. 2007, Doolittle & Bellantoni 2010, Papadopoulos et al. 2010, Orlando et al. 2013, Bigman 2014, Hansen et al. 2014, Deiana et al. 2018b). Many Mycenaean chamber tomb cemeteries have been found in the region of Elis in the past, also in the wider area of the sanctuary of ancient Olympia (Fig. 2.1). Pottery dates the use of these tombs generally to the period from the end of the 15th century BC to the beginning of the 11th century BC, although the period of use might vary from site to site. All Mycenaean tombs in the surroundings of the cult site of Olympia show the typical characteristics of chamber tombs that are cut into soft rock material: the chamber contains a varying number of burial pits used for primary and secondary burials, the doorway (stomion) that is often blocked with stones, and the entrance passage (dromos) varying in width and length (Fig. 2.2C) (Waldbaum 1966, Dickinson 1983, Karkanas et al. 2012, Vikatou 2012a).

Fig. 2.1: Topographic overview of the wider study area showing a section of Elis with the Alpheios and Kladeos rivers, sites of Mycenaean chamber tombs (white boxes, after Vikatou 2012a), areas of surface survey (hatched area) and the location of the three study sites, each with the position of ERT transects (white arrows) and the GPR area; (A) Mageiras-Kioupia site, (B) Epitalio site, (c) Dartisa site. See text for further explanations. Map modified after Google Earth aerial images, 08/2017; Aerial photograph of the Dartisa site by T. Willershäuser.

One of our study sites is the cemetery of Mageiras-Kioupia, situated near the village of Mageiras only 3 km to the north of ancient Olympia (Fig. 2.1A). The necropolis represents the most important and richest Mycenaean cemetery of the entire Elis region and came to light after the fires of 2007 that hit the area (Vikatou 2012a). Excavations followed and until 2010 eight chamber tombs were investigated. The tombs contained four warrior burials of different chronologies spanning the Mycenaean palatial and post-palatial periods. They contained valuable grave goods include swords and other items of weaponry as well as jewelry. Until the time when the tombs were found, the area was considered as sparsely populated during Mycenaean times. Therefore, these finds are of great importance for understanding the Mycenaean period in Elis and prove the existence of a high-ranking group within the Alpheios valley close to the later sanctuary of Zeus at Olympia (Vikatou 2012a). The tombs that belonged to warriors, buried with their weapons (arrowheads, Naue II type swords, greaves and helmet remnants), are characterized by their larger dimensions and elaborate constructions. The largest, monumental warrior grave possessed a richly decorated burial site of a warlord-ruler of the LH III A period, which was richly furnished, apart from weapons, with golden jewelry (necklaces, diadems, rings, seals etc., see Vikatou 2012a, Vikatou 2012b, Vikatou 2012c, Vikatou 2012d, Vikatou 2013, for weapons see Vikatou and Jung 2018). This grave is characterized by a 17 m long dromos (Vikatou 2012a). All investigated tombs at Mageiras-Kioupia are oriented parallel to the NE-SW running Kladeos River and carved into the southern slope of a prominent ridge out of sand- and siltstones belonging to the Vounargon Stage, Upper Pliocene in age (Fig. 2.2) (IGME 1980).

Another two study sites are located to the north of the village of Epitalio. The village lies at the very fault scarp marking the western fringe of the hilly country extending to the west and southwest of Olympia. Exposed to the west, it directly faces the coastal lowlands of the former Agoulenitsa Lagoon and the open waters of the Gulf of Kyparissia. Similar to the Mageiras-Kioupia site, the local bedrock is made out of a sequence of Tertiary siltstone and sandstone belonging to the Vounargon Stage of the Upper Pliocene (IGME 1980).

With respect to the study site near Epitalio (Fig. 2.1B), the entrance of a collapsed small chamber tomb was discovered within the course of the preceding archaeological survey. The discovery led to the assumption that more chamber tombs may be found in the vicinity. At the study site Dartisa, which is located on top of the natural plateau following the fault scarp towards the east, a shallow hill indicates possible man-made changes of the natural topography (Fig. 2.1C).

2.2 Material and methods

The archaeological and historical exploration of (past) landscapes requires appropriate methodological approaches. The specific archaeological method for exploring archaeological aspects of landscape history is the surface survey. Using the survey method, superficially visible archaeological and architectural remains are systematically detected. The Olympia-Area-Survey-Project applies the method of the intensive grid survey. This means that the prospecting area is surveyed systematically and no pre-selection has been made regarding

potential find spots. A regular grid of fields to 100 m x 100 m divides the investigation area and provides the basis for prospection. Every grid cell is surveyed by the field-walkers in tracks with 10-12 m distance between each track whereby the visible finds on the surface are recorded quantitatively. All significant objects in connection with the settlement history in the surroundings of Olympia are collected as samples for further analysis. Architectural remains are measured on site and documented graphically as well as photographically (Lang 2002).

Our study presents results of geophysical investigations that were carried out in three different areas by the team of the Johannes Gutenberg-Universität Mainz (Germany). In a first step, we collected ERT data at places where Mycenaean chamber tombs had already been located and partly excavated. This was done to obtain a characteristic ERT response for chamber tombs in different preservation states (study site Mageiras-Kioupia) in the present sand- and siltstone marl surroundings of the Vounargon Stage of Upper Pliocene age (IGME 1980). Different sediments and bedrock material are characterized by different ranges of electrical resistivity due to differences in mineral composition and water content (Loke 2012, Ullrich et al. 2007). The lower the clay mineral content and the lower the pore water content, the higher is the electrical resistivity and vice versa. Subsurface areas filled with air therefore yield extremely high resistivities in contrast to the natural bedrock and overlying sediments and soils. In general, cavities can only be measured by ERT as second order effects, because a cavity provides infinite resistivity. Thus, the electric current flows around the cavity, creating an integral effect on the potential distribution, resulting in increased electrical resistivity in the surrounding of the cavity (Putiška et al. 2016, Csibri et al. 2018). In this case, ERT results show big vertical and horizontal anomalies centering the air-filled structure (Cardarelli et al. 2010, Orlando et al. 2013). Intact Mycenaean chamber tombs with preserved chambers are still filled with air and therefore easily discoverable by the use of non-invasive ERT techniques.

After investigating the resistivity patterns of intact Mycenaean tombs at Kioupia, we transferred these experiences to other, selected areas of the Olympia Area-Survey Project (study sites Epitalio and Dartisa) in order to verify potential chamber tombs. However, the roofs of Mycenaean chamber tombs are often collapsed and the chambers filled with different types of sediment, accumulated or dumped with irregular geometries (Karkanas et al. 2012, Nero et al. 2016). In such cases, the difference in resistivity between the collapsed tomb and the surrounding material will be smaller and the lateral and vertical resistivity gradients will be much smoother so that it might be difficult to detect unknown tombs below the surface.

Electrical resistivity tomography (ERT) measurements were conducted along transects using a Syscal R1 Plus Switch 48 multi-electrode system (IRIS Instruments). We applied a Wenner-Schlumberger electrode configuration that represents a good compromise in the effort to achieve similar resolutions both in the vertical and horizontal direction (Loke 2012). A total of 10 ERT profiles were measured in this study. On the basis of varying topography and accessible space at the different study sites, we choose an electrode spacing of 2 m (94 m of profile length) at the Mageiras-Kioupia site (ALP ERT 149-152), 1 m (47 m of profile length) (ALP ERT 197, 199, 200) and 2 m (94 m of profile length) (ALP ERT 198) at the Epitalio site and 0.75 m (35.25 m of profile length) at the Dartisa site (ALP ERT 239, 241, 242). ERT transects were

mostly arranged parallel to the slope with the aim of achieving a transverse section of known and/or potential chamber tombs. ERT field data were inverted using the RES2DINV software tool and the least square inversion method (Loke et al. 2003). In some cases where resistivity differences appeared very high, we applied a model refinement to double the blocks in the model. To ensure the overall comparability of all ERT depth sections, all data were displayed using the same logarithmic contour values for electrical resistivity, given in ohm.m. We are aware that, on a detailed scale, resistivity values are dependent on the electrode spacing, but resistivity values of cavities are significantly larger than those of the surrounding bedrock material, in each and every case, and therefore give reliable information on where a chamber can be expected. The positions and absolute elevations of ERT electrodes were measured by means of a differential GPS type Topcon HiPerPRO FC-250 to include the topography into the inversion results. At Mageiras-Kioupia, one excavated chamber tomb was measured by terrestrial laser scan (TLS) using a Topcon GLS 1500 with a minimum accuracy of +/- 20 mm and total number of 9.3 billion points. Altogether, two scans were fitted together and calibrated by targets to achieve highest and accurate overlapping and the coloring was set to RGB values. Surfaces colored in dark blue are low reflective, green colored areas have medium reflectivity and red color marks highly reflective surfaces. In addition to ERT measurements, GPR studies were carried out at the Epitalio site by the team of the Christian-Albrechts-Universität Kiel where ERT results indicate highest resistivity anomalies. GPR is a very useful tool to map the spatial extent of subsurface archaeological structures with a higher resolution compared to ERT techniques (Shabaan et al. 2009). However, GPR depends very much on site conditions and is most useful in homogenous and resistive environments (Jones 2008, Orlando et al. 2013, Booth et al. 2015). A GPR antenna sends a high frequency (MHz) electromagnetic impulse into the subsoil and records reflections generated at interfaces. The travel time of the reflection and the speed of electromagnetic waves in solid media can be used to derive the depth of the reflection interfaces (Koppenjan 2009, Sarris et al. 2017).

GPR measurements were performed with a SIR 4000 recording unit (GSSI) and a 400 MHz antenna along linear profiles. The antenna was pulled along the profile, while sending an electromagnetic impulse 100 times per second and recording signals reflected at subsurface interfaces with different dielectric permittivity. Positioning was collected using a Leica RTK-DGPS system. When measuring in a linear manner, multiple parallel profiles are performed and interpolated throughout the desired measuring area. This results in a reflection amplitude data cube that can be cut horizontally into time slices. Such time slices hold the reflection amplitude of a certain travel time interval. If the wave-velocity of the area is known, time slices can be transformed to depth slices.

Measurements were performed with a profile spacing of 0.3 m. GPR data processing was realized using the MATLAB software and comprised the following steps:

(1) Universal Transverse Mercator coordinates were assigned to each profile, (2) 8 cm bins were formed along each profile and the traces of each bin were averaged, (3) the onset of the direct wave to time was adjust to ‘zero’, (4) the direct wave was suppressed by subtracting the mean trace of each profile from the binned traces, (5) the velocity of electromagnetic waves (12 cm/ns) was determined by fitting hyperbolae to selected diffractions in various

radargrams, (6) the processed data of all profiles were sorted with respect to coordinates in order to form a joint data volume and performing 2D data binning on a grid of 15 cm x 15 cm, (7) a trace normalization was preformed using the median of each trace, (8) 3D semblance based coherence filtering was undertaken after Milkereit & Spencer (1989), which suppresses non coherent reflection events and also works as a 3D interpolation tool, interpolating data gaps of up to 6 bins, (9) a 3D fresnel volume migration with a constant velocity of 12mc/ns was performed (Buske et al. 2009) and finally (10) depth slices were calculated by summing up the absolute values of reflection amplitudes for each bin in intervals of 24 cm thickness every 12 cm, beginning at a depth of 24 cm.

2.3 Results

2.3.1 Mageiras-Kioupia

In the Kladeos valley, where the Mageiras-Kioupia cemetery (Vikatou 2012a) is located, we realized three ERT transects. ERT transects ALP ERT 149, ALP ERT 150 and ALP ERT 151 are arranged in a fan-shaped order from NW to SE direction more or less parallel to the length axis of the necropolis hill. Each of these ERT transects crossed at least one chamber tomb that was already excavated (Figs. 2.1A, 2.2).

In general, transect ALP ERT 149 yielded a depth section showing a lower zone with low to intermediate electrical resistivity values (< 100 ohm.m) and an upper zone of high resistivity values (100-700 ohm.m) (Fig. 2.3). The maximum vertical increase of electrical resistivity, where the vertical resistivity gradient is strongest, marks the border between siltstone at the base and porous sandstone on top. The latter reaches the ground surface and locally outcrops at the recent surface where the soil cover is missing. It is striking that the lower part of the depth section shows a clear and regular pattern whereas the upper part is characterized by many vertical and horizontal resistivity anomalies. We labeled strong resisistivity anomalies with ‘A’ (resistivity > 1000 ohm.m) and weaker resisistivity anomalies with ‘B’ (resistivity 500-1000 ohm.m). Highest electrical resistivity values (> 1550 ohm.m) were measured for a dromos, which was partly excavated (Figs. 2.3, 2.4C). A large chamber, unearthed so far and only accessible via the stomion of the tomb, became visible connected to this dromos showing electrical resistivity values between 750 and >1550 ohm.m (marked with no. 1A, Fig. 2.3). The dimension and shape of this chamber no. 1A as well as the associated dromos and stomion were measured and visualized by means of TLS. The floor area measures 5 m x 5 m (Fig. 2.4A). Fig. 2.4A allows to neatly differentiate between the characteristic elements of the chamber tomb and helped to identify a looting shaft directly aiming at the stomion. It seems as if the bulb of extremely low resistivity values depicted in the depth section of ALP ERT 149 directly adjacent to chamber tomb and dromos is an inversion artifact caused by the inversion model (Loke et al. 2003). Additionally, we detected two areas of anomaly type ‘B’ along transect of ALP ERT 149, approximately some 4-5 m below surface: the first anomaly lies between 34 m and 42 m (marked with no. 2B, Fig. 2.3) and the second lies between 58 m and 64 m (marked with no. 3B, Fig. 2.3).

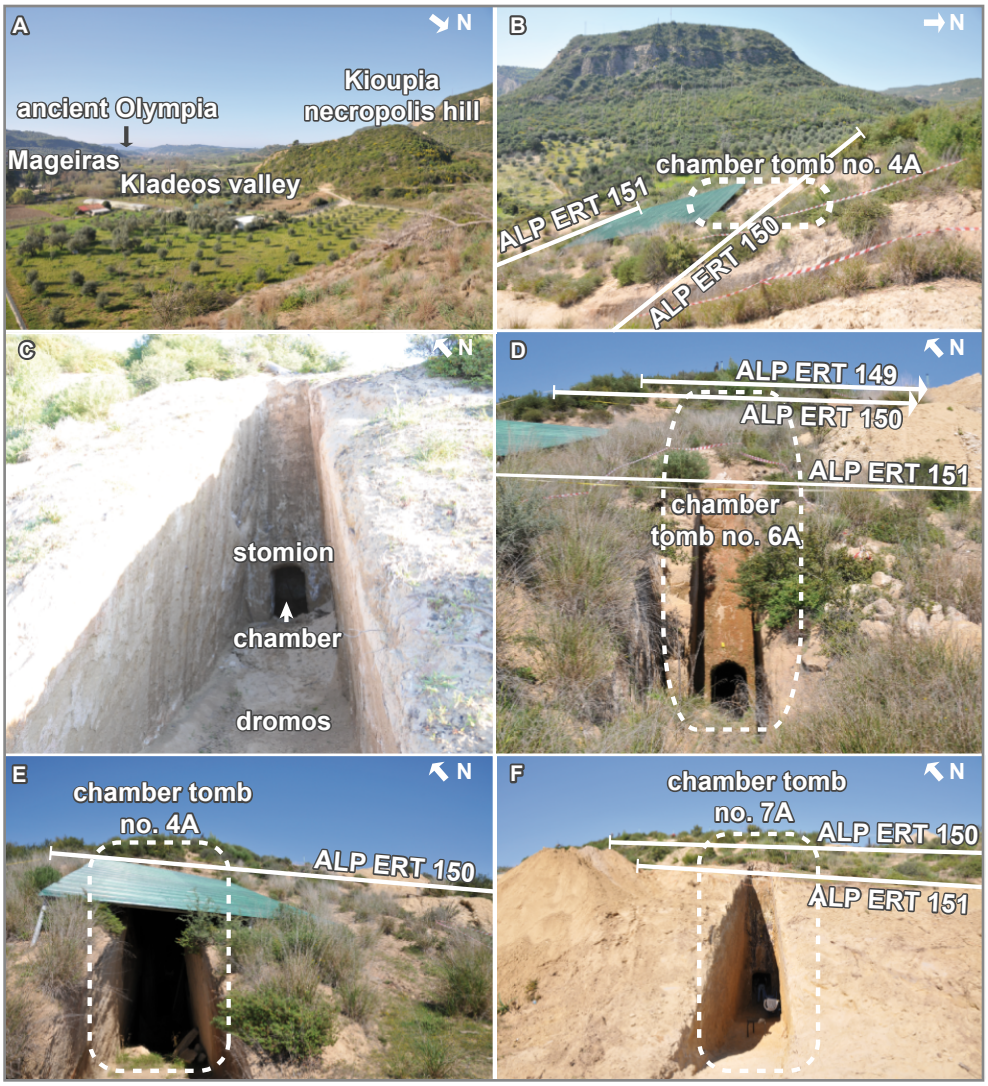

Fig. 2.2: Mageiras-Kioupia necropolis hill and excavation of selected chamber tombs. (A) Mageiras-Kioupia cemetery hill and view to the Kladeos valley, (B) Location of chamber tomb no. 4A at transect ALP ERT 150, (C) Insight view of an excavated chamber tomb at Mageiras-Kioupia with the typical dromos, stomion and chamber, (D) Entrance of chamber tomb no. 6A, of which the associated chamber is visible in the depth section of ERT ALP 150, (E) Entrance of chamber tomb no. 4A, of which the associated chamber is visible in the depth section of ERT ALP 150, (F) Entrance of chamber tomb no. 7A, of which the associated chamber is visible in the depth section of ERT ALP 150. Excavated chamber tombs and possible chamber tomb depicted in the ERT data are marked with dotted lines. Photos by A. Vött.

Similar results were found for ERT transects ALP ERT 150 and ALP ERT 151 situated a few meters downhill of transect ALP ERT 149. At transect ALP ERT 150 highest electrical resistivity values were measured for the excavated chamber that was recently discovered and accessible via the dromos at the time of ERT measurements (> 1200 ohm.m, marked with no. 4A; Figs. 2.2B, 2.2E, 2.3). The depth section of transect ALP ERT 151 revealed highest electrical resistivity values for two open dromoi (Figs. 2.2D, 2.2F). The first is located between 22 m

and 26 m directly opposite of a eak resistivity anomaly of transect ALP ERT 150 (marked with no. 6; Fig. 2.3). The second dromos lies between 58 m and 62 m and again directly opposite of an area of anomaly type 'B' at the depth section of ALP ERT 150 (marked with no. 7B; 2.3). Therefore, our ERT depth sections at Mageiras-Kioupia revealed maximum electrical resistivity values of type 'A' where adjacent excavations unearthed original chamber tombs, still intact and filled with air. However, further areas with increased resistivity values of type 'B' were found at a comparable depth level some 15-20 m distant from each other all along the transects. They probably represent further chamber tombs, still unearthed, and possibly filled with unstructured material, such as loose sediments and soil with a comparatively high portion of air-filled pores and thus a comparably low compactness.

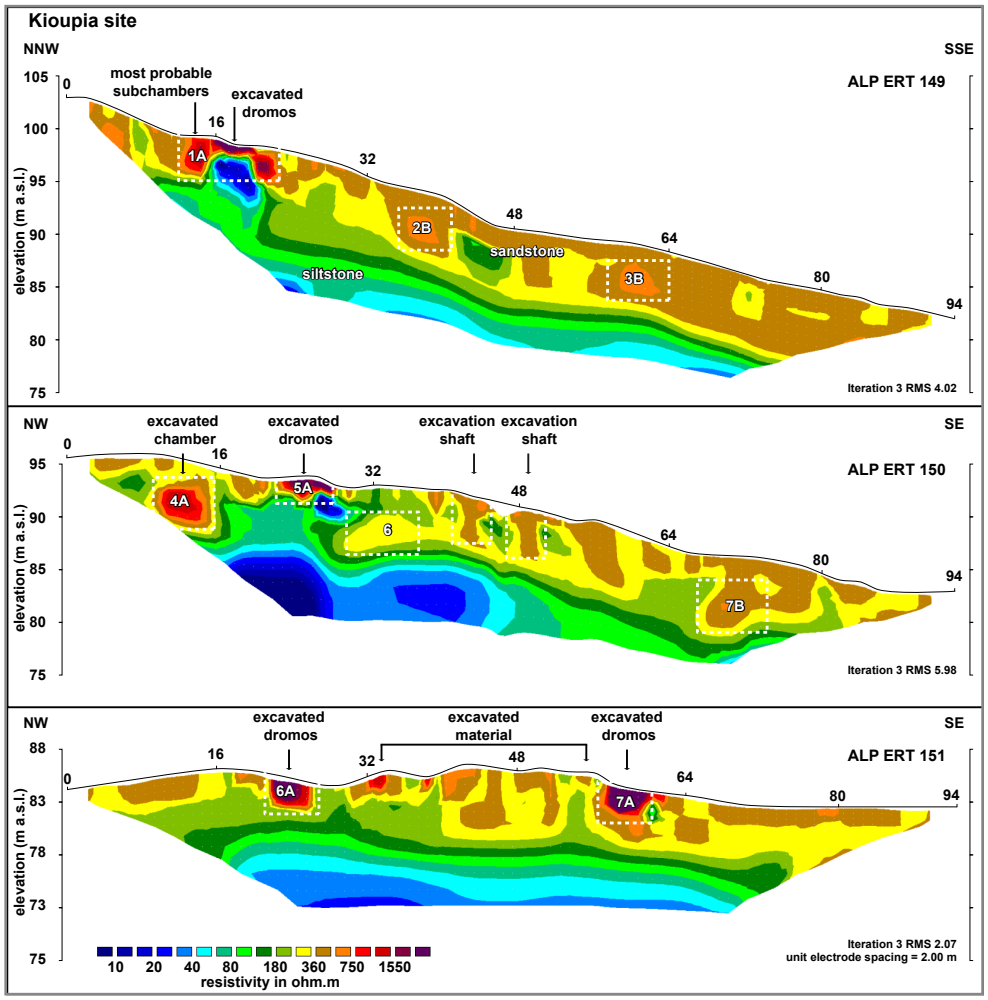

Fig. 2.3: 2D resistivity models with chamber tomb candidates (dotted ines) of transects ALP ERT 149, ALP ERT 150 and ALP ERT 151 at the Mageiras-Kioupia site. For location of transects see Fig. 2.1. See text for further explanations.

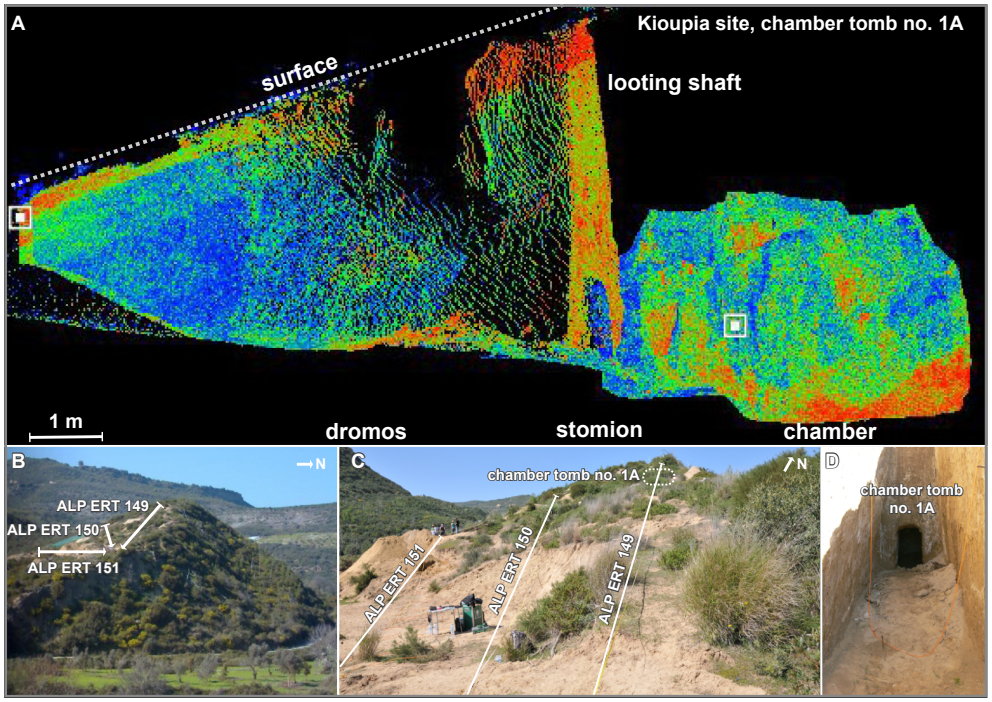

Fig. 2.4: Chamber tomb no. 1A at Mageiras-Kioupia. (A) TLS of the chamber tomb no. 1A showing the overall structure of the excavated tomb, (B-C) Mageiras-Kioupia hill, the local topography and location of ERT transects, (D) Stomion of chamber tomb no. 1. Photos by A. Vött.

2.3.2 Epitalio

In 2015, a handle and other fragments of a Mycenaean pottery vessel were found to the north of the village Epitalio. In the subsequent cleaning of the surface, further fragments, belonging to three different vessels were encountered. The topographical situation as well as the vessel types suggested the presence of a Mycenaean chamber tomb.

We carried out measurements along four ERT transects where the preceding archaeological survey brought to light these remains of a chamber tomb (Fig. 2.5). Similar to the Mageiras-Kioupia site, ERT transects (ALP ERT 197, ALP ERT 198, ALP ERT 199 and ALP ERT 200) were arranged more or less parallel to the length axis of the investigated hill, namely in a W-E direction (Fig. 2.1B).

Our ERT data show that the bedrock has the same characteristics as the bedrock observed at the Mageiras-Kioupia site. ERT depth sections clearly depict the border between low-resistivity siltstone at the base and overlying high-resistivity sandstone (Fig. 2.6). Minor differences between the electrical resistivity values of different ERT transects across the sandstone unit may be caused by varying water content and variations of pore volume. In a general view, the sandstone unit increased in thickness from the mid-section of the hill (ALP ERT 197) towards the hilltop (ALP ERT 198-200).

Fig. 2.5: Selected geomorphological features of the Epitalio site. (A) View from the Epitalio site to the coastal lowlands of the former Agoulenitsa Lagoon and the Gulf of Kyparissia, (B) Course of transect ALP ERT 197, location and remains of chamber tomb no. 2B, (C) Top of the Epitalio hill with transects ALP ERT 199 and ALP ERT 200 showing the location of chamber tomb candidate no. 7A; view to the NW towards the coastal plain, (D) Ridge of the Epitalio hill with transects ALP ERT 199 and ALP ERT 200 showing the location of chamber tomb candidate no. 7A; view to the E, (E) Mid hill position of the study site with transects ALP ERT 198 and ALP ERT 200; view to the NE towards Dartisa, (F) Eastern section of the Epitalio hill with transect ALP ERT 200. Photos by A. Vött.

ERT transect ALP ERT 197 crossed the site where part of a dromos was found within the framework of the preceding archaeological survey (Fig. 2.5A, B). In the corresponding depth section, a wide interference zone was found between 21 m and 32 m that possibly indicates the redistribution of material by man within the course of building the tomb (marked with 2B; Fig. 2.6). Electrical resistivity values range between 400-750 ohm.m (type 'B') and are therefore lower than those obtained for the excavated tombs at Mageiras-Kioupia. This may indicate that the tomb may be completely filled with loose material. Rescue excavations were carried out by the responsible Ephorate of Antiquities, in the course of which the entrance zone of a destroyed chamber tomb was found, and thus the existence of the grave was generally confirmed.

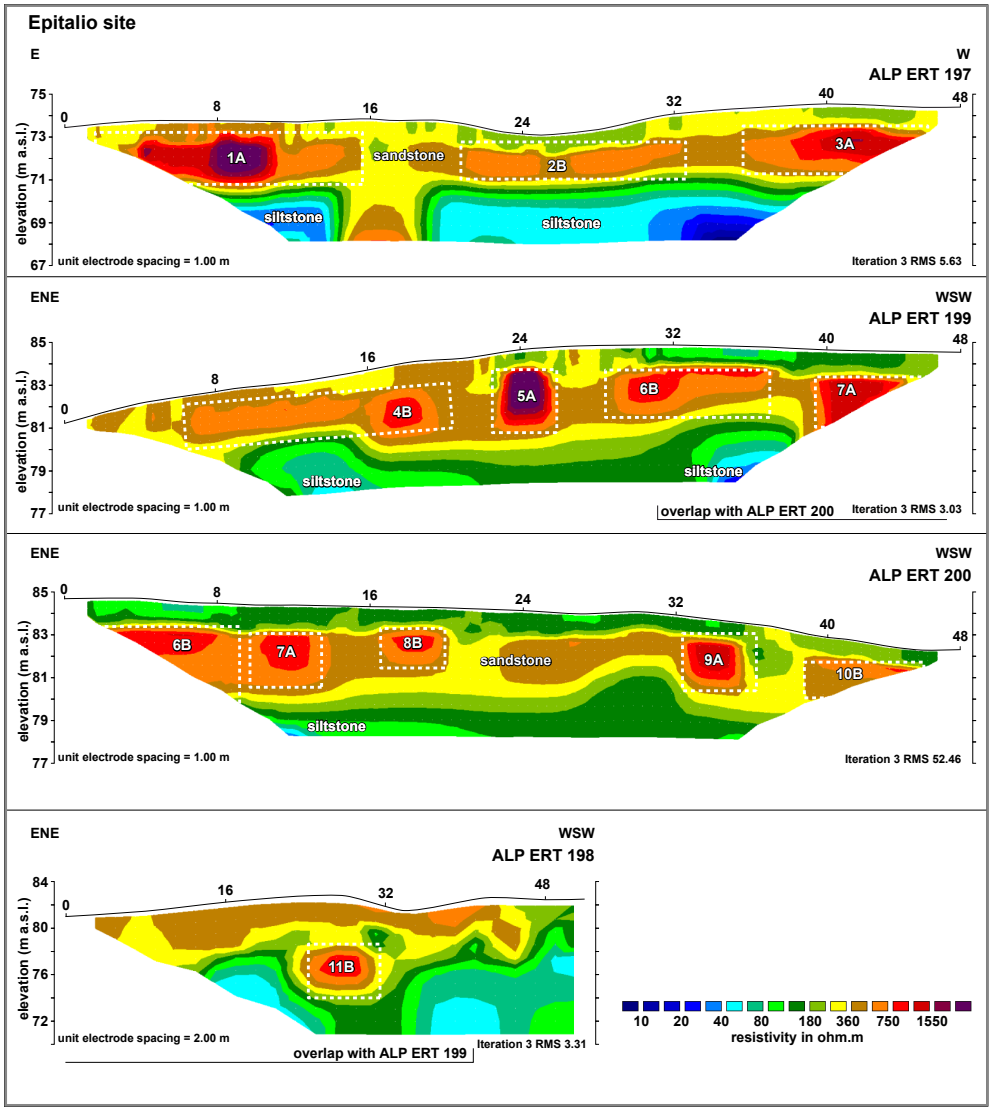

Fig. 2.6: 2D resistivity models with chamber tomb candidates (dotted lines) of transects ALP ERT 197, ALP ERT 198, ALP ERT 199 and ALP ERT 200 at the Epitalio site. For location of transects see Fig. 2.1. See text for further explanations.

However, we detected further zones of very high resistivity values (> 750 ohm.m, locally >1550 ohm.m) on the Epitalio hill that show a distinct rectangular shape in the ERT depth section. These anomalies of type 'A' are situated at 8 m to 11 m (no. 1A) and 39 m to 48 m (no. 3A) of ERT transect ALP ERT 197, at 22 m to 26 m (no. 5A) and 40 m to 44 m (no. 7A) of ERT transect ALP ERT 199 and at 32 to 36 m (no. 9A) of ERT transect ALP ERT 200. Anomaly no. 7A is also displayed in the overlapping depth section of transect ALP ERT 200 (Figs. 2.5C, 2.5D, 2.6). Additional zones of increased electrical resistivity with characteristics of type 'B' are located between 16 m and 19 m (no. 4B) and 30 m and 37 m (no. 6B) of transect ALP ERT 199 and between 17 m and 20 m (no. 8B) and between 39 and 45 m (no. 10B) of ERT profile ALP ERT 200. Another anomaly of Type 'B' was found in the depth section of ALP ERT 198 (no. 11B; Fig. 2.6) but slightly deeper than anomaly no. 6B lying directly opposite on transects

ALP ERT 199 and 200. All these anomalies are aligned horizontally and show a more or less regular arrangement within the sandy bedrock.

Fig. 2.7 shows the results of the GPR studies. The dataset shows a complex three dimensional structure visible as a high reflection amplitude feature, which is mainly ordered in a rectangular way. The feature occurs in the southeastern part of the survey area as coherent rectangular reflection (Fig. 2.7; E and D) between the transects ALP ERT 198 and ALP ERT 200 at the positions of anomalies no. 11B and 6B, respectively. The strong reflection was found at depths of about 2 m below surface (b.s.) and becomes surrounded by linear reflection events at lower depths (Fig. 2.7; C, ~1.2 m) and then continues as smaller structure up to the surface (Fig. 2.7; A and B). Three clear additional reflections were measured at 1 m b.s (B); their positions are consistent with the positions of ERT anomalies no. 4B, 5A and 6B. Furthermore, some reflections show a reversed polarity, which is due to a negative impedance contrast, and thus possibly indicates less consolidated material below those reflections.

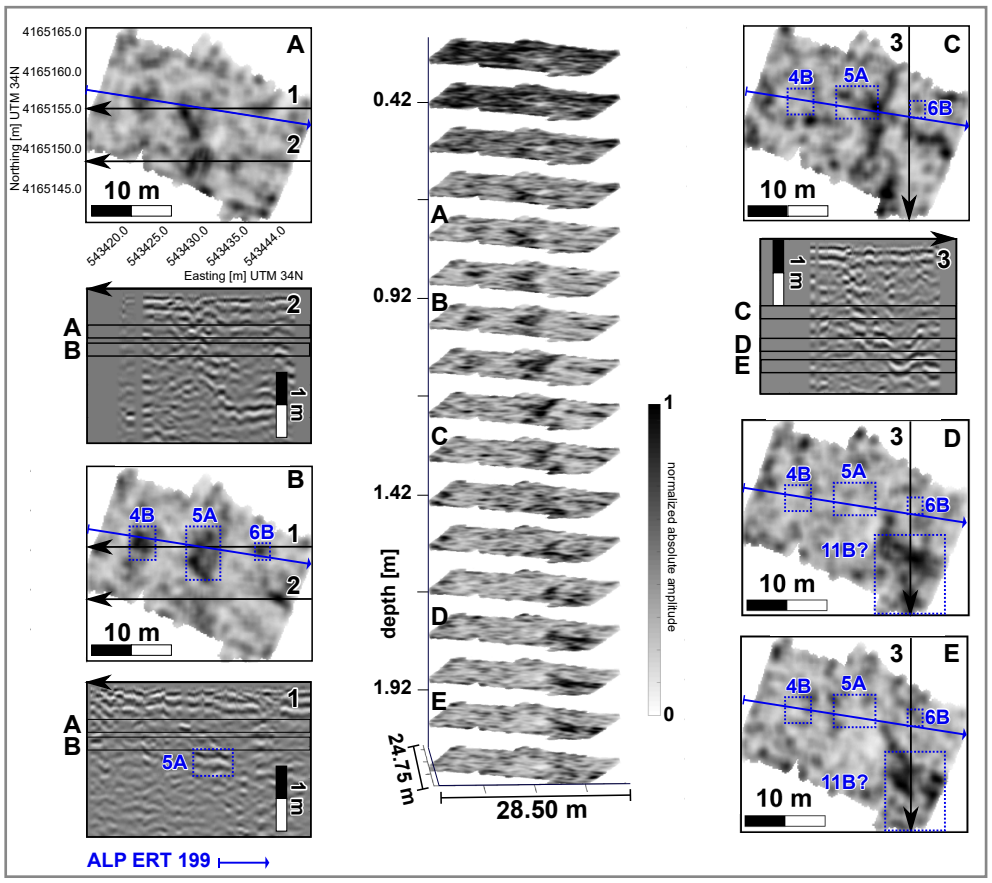

Fig. 2.7: Results of GPR studies conducted at the Epitalio study site. Center shows all GPR depth slices along a depth axis (m below surface). Capital letters A to E correspond to exemplary depth slices showing main features. Depth slices A to E are illustrated as top view, together with exemplary vertical radargrams (no. 1 to 3). Positions of vertical radargrams are indicated by black arrows in corresponding depth slices A to E. Boxes with dotted lines mark positions of corresponding ERT anomalies indicating chamber tomb candidates (see Fig. 2.6).

2.3.3 Dartisa

ERT measurements at Dartisa were aligned along N-S (ALP ERT 239), W-E (ALP ERT 241) and SW-NE (ALP ERT 242) directions with focus on a low mound which is part of the widespread Dartisa plateau. Due to its shape and position, this mound was searched for archaeological structures. The mound does not show a clear length axis or any other traces regarding the existence and orientation of potential chamber tombs. In contrast to the Mageiras-Kioupia and Epitalio study sites, we only detected values of type 'B' anomalies for the uppermost parts of ERT depth sections that means right for the top section of the hill (Fig. 2.8). These high electrical resistivity values are caused by sandstone that crops out at the surface where the soil cover is missing. In a general view, ERT depth sections do not allow to differentiate as clearly between different bedrock units as this was possible for the Mageiras-Kioupia and Epitalio sites. However, a zone of comparatively lower resistivity at the base of the depth section seems to represent the basal siltstone unit. As evidenced by a nearby spring located to the south of Dartisa, increased water content may also be the reason for decreased differences in the overall resistivity spectrum.

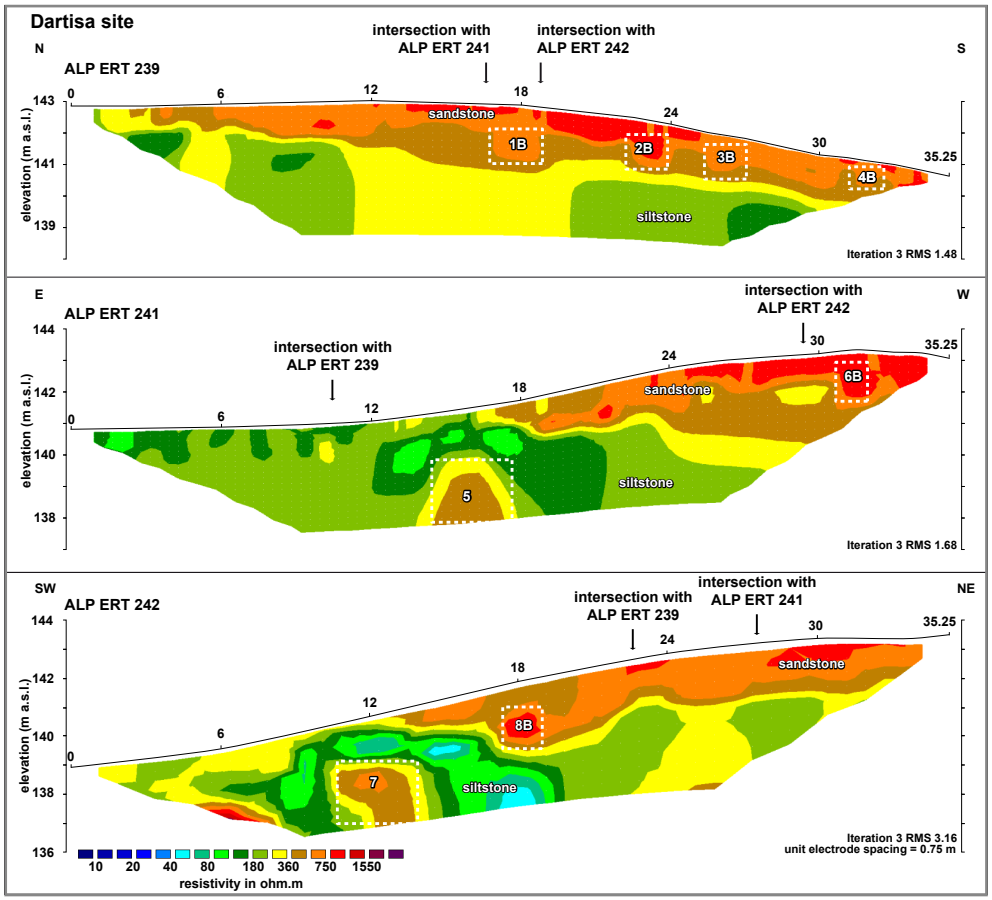

Fig. 2.8: 2D resistivity models with possible chamber tomb candidates (dotted ines) of transects ALP ERT 239, ALP ERT 241 and ALP ERT 242 at the Dartisa site. For location of transects see Fig. 2.1. See text for further explanations.

Four conspicuous features with higher resistivity values compared to the background were found for transect ALP ERT 239 and further two for transect ALP ERT 241, however, very close to the present ground surface. Areas of resistivity values of type 'B' (marked with 1B, 2B, 3B, 4B, 6B) show a rectangular shape and are horizontally aligned (Fig. 2.8). However, it must be noted that these zones are not wider than c. 1.5 m and were found at a maximum depth of 1 to 2 m below surface. This is also the case for anomaly no. 8B of transect ALP ERT 242. Larger areas with increased resistivity were detected for depth section of transect ALP ERT 241 between 14 m and 17 m with values up to 400 ohm.m (marked with 5). A clear anomaly, 3 m wide, was found for transect ALP ERT 242 between 10.50 m to 13.50 m (marked with 7), reaching in parts type 'B' characteristics (Fig. 2.8).

2.4 Discussion

At Mageiras-Kioupia, several Mycenaean chamber tombs were excavated during the past years and have revealed outstanding archaeological findings (Vikatou 2012a). Here, we were able to ascribe specific resistivity features in ERT depth sections to known and partly already unearthed chamber tombs. For example, the maximum resistivity zone depicted in the depth section of transect ALP ERT 149 corresponds to the air-filled chamber tomb no. 1A (Figs. 2.3, 2.4). Similar findings were made for depth section of transect ALP ERT 150 of which highest resistivity anomalies display chamber tomb no. 4A (Figs. 2.2B, 2.2E and 2.3). Further anomalies no. 6 and 7B (ALP ERT 150) are also interpreted as subchambers associated with chamber tombs. The latter seem to be related to dromoi of anomalies 6A and 7A (Fig. 2.3). First, they are located in the direct opposite of the two open dromoi. Second, both candidates are located in the same elevation level. Height measurement of the stomion base yielded 3 m below surface for anomaly no. 6A (Fig. 2.2D) and 4 m below surface for anomaly no. 7A (Fig. 2.2F). These depth are identical with the results depicted in the 2D model of ALP ERT 150 and are in good agreement with the base of anomalies 6 and 7B (ALP ERT 151; Fig. 2.3).

At the Epitalio site, archaeological evidence of a single chamber tomb comes from immediately adjacent to the asphalt road in a mid-slope position. In addition, anomalies similar to the ones found at Mageiras-Kioupia were measured on the entire upper slope. Anomalies no. 1A (ALP ERT 197) and no. 5A (ALP ERT 199) at Epitalio stand out with their extremely high resistivity values. These anomalies accord very well with values that were retrieved at the known chamber tomb no. 1A at Mageiras-Kioupia (Fig. 2.6) and are thus interpreted as possible chamber tombs. Moreover, both chamber tomb candidates (no. 1A and 5A) show a rectangular shape, and especially anomaly number 5A shows a marked contrast to the surrounding material. These features are typical of tombs as described by Papadopoulos et al. (2010) and Nero et al. (2016). Since air will not conduct electrical currents, we further expect anomalies marked with 'A' to represent intact tombs that means cavities that are still filled with air. Our interpretation is that the A-type anomalies at the Epitalio site do reflect such original chamber tombs because (i) the ERT data are similar to the Mageiras-Kioupia site, where excavated tombs yielded an identical ERT pattern, (ii) the rectangular shape, the overall dimensions and (iii) the extraordinarily high resistivity values cannot be explained by

natural processes and are typical of tombs as reported by other studies.

In contrast, ERT data collected along transect ALP ERT 197 at Epitalio, where parts of a tomb were found during an archaeological survey (no. 2B) revealed values only slightly different from those found for the local bedrock. Such results can be interpreted as collapsed chamber tombs that were filled by loose material that is more porous and less compact than the surrounding bedrock (Astin et al. 2007, Nero et al. 2016). Buried tombs are rarely intact (Karkanas et al. 2012), and this evaluation seems to be true for all anomalies marked with 'B'. Based on this finding, two further chamber tomb candidates at Mageiras-Kioupia (no. 2B and 3B) and four at Epitalio (no. 4B, 6B, 8B and10B) were identified. ERT results are highly consistent with GPR data. GPR cross-section profile 1 displays a clear reflection at c. 1 m b.s. that appears in the same elevation as the top edge of ERT anomaly no. 5A (Fig. 2.7). Two other, smaller structures found along GPR cross-section profile 1 show the same positions as anomalies no. 4B and 6B of ERT transect ALP ERT 199. However, towards deeper GPR depths, structures 4B, 6B (Fig. 2.7, C, ~1.2 m) and 5A (Fig. 2.7, D, ~1.7 m) become unclear. Therefore, we assume that even chamber tomb candidate no. 5A is filled with porous material at a lower depth. Moreover, at Epitalio, we found long zones of slightly lower resistivity adjacent to chamber tomb candidates no. 4B, 6B and 9A, up to 8 m long. These zones may depict, in a random cross-section along the length-axis of the tomb, the dromos associated with the chamber. Such dromoi constellations are usually filled with sediments and therefore show lower electrical resistivity values (Karkanas et al. 2012). The overall base of the anomalies detected was found down to 5 m and 6 m below the present surface at Mageiras-Kioupia and at Epitalio, respectively. At both sites, we found the chamber tomb candidates horizontally aligned, which is typical of such cemeteries (Nero et al. 2016).

Considering both type 'B' and type 'A' anomalies and assuming that they represent chamber tombs filled with reworked sediment and soil, or still being intact, respectively, the 2D dimensions of chamber tomb candidates range from 2 m x 2 m to 11 m x 3 m. Further GPR depth slices show a 3D structure at c. 2 m b.s. in the southeastern part of the investigated area (Fig. 2.7; D and E), at least 10 m long and ordered in a rectangular way, indicating anthropogenic origin. We interpret this as another chamber tomb candidate that may correspond to ERT anomaly no. 11B. The results shown may display the upper, air-filled part of the chamber or indicate a connection between chamber tomb candidates no. 6B, 7A and 11B. If so, chamber tomb canditates 6B, 7A and 11B would represent a large chamber tomb with associated dromos, altogether 17 m long. Such large differences in the tomb dimensions may be explained by differences in the social class of the dead as the case of Mageiras-Kioupia illustrates (Vikatou 2012a).

However, some constraints have to be discussed with regard to the ERT and GPR-based methodological approach. First, based on these datasets alone, it is not possible to discriminate conclusively between dromos and chamber. This is because one cannot exclude that a GPR area or an ERT transect covers only parts or lateral sections of a tomb complex, and the distance between neighbouring ERT transects is still too large. Moreover, the resolution of data decreases with depth and ERT electrode spacing so the interpreted size of anomalies need to be evaluated in comparison to these criteria. Second, the dimensions of an anomaly

observed by means of geophysical methods often appear larger than the dimensions of the corresponding cavity in the real subsurface (Butler 2008). This is also due to the fact that air-filled cavities are identified as second order effects based on indirect measurements (see chapter 2.2). Nevertheless, our studies provide evidence for altogether 11 chamber tombs dug into the local Tertiary sandstone of the hill at Epitalio. These dimensions indicate a quite substantial Mycenaean burial place in the western Peloponnese. It is already known that there was a Mycenaean settlement near Epitalio (i.e. on the Barkeika hill) used from early Mycenaean times to the end of the palatial period (15th to end of 13th century BC; Nikolentzos 2011). The newly identified cemetery substantially improves our knowledge on the distribution of human activity in the area during the Late Bronze Age.

Finally, we transferred our results from Mageiras-Kioupia - where many chamber tombs have already been excavated and where we calibrated our ERT-based approach - via Epitalio - where we were able to detect and localize a new, most probably Mycenaean burial site - to the Dartisa plateau. Here, no systematic information on archaeological remains currently exists. The shape of the low mound at Dartisa may suggest hidden ancient tombs (see e.g. Papadopoulos et al. 2010). However, based on the results of our ERT measurements and considering topographical conditions, no probable chamber tomb candidates can be identified at this site. The geometry of rectangular 'A' and B' anomalies depicted in depth sections of transects ALP ERT 239 and ALP ERT 241 are too small and their depths too shallow to represent chamber tombs. However, the shape of ERT anomalies appear unnatural and are suggestive of box-type graves unearthed from the local sandstone unit. Similar features observed by geophysical surveys are often interpreted as graves, for example by Neuhauser (2009) and Hansen et al. (2014). However, we may also think of artificial hollows used for storage. In comparison with the dimensions of the chamber tombs observed at both Mageiras-Kioupia and Epitalio, only two anomalies depicted in depth sections of transects ALP ERT 241 and ALP ERT 242 are notable (no. 5 and 7). Both candidates are situated in hill slope position and show resistivities slightly lower than type 'B' anomalies. Moreover, they seem to be located in the midst of a siltstone zone, which is atypical compared with Mageiras-Kioupia and Epitalio. Anomalies may be caused by differences in the water content or represent artifacts triggered by neighbouring low-resistivity water-bearing sub-zones at the hillside toe. So far, geophysical data available for Dartisa do not allow to explain such resistivity anomalies as chamber tombs. In any case, the ERT-based geophysical approach for detecting and locating chamber tombs such as at Epitalio requires archaeological excavation for final verification.

2.5 Conclusions

We calibrated an ERT-based geophysical approach to detect and locate chamber tombs at Kioupia where excavations during the past years have brought to light archaeological evidence of a large burial site of the Mycenaean period with precious grave goods (Vikatou 2012a). Intact chamber tombs turned out to yield highest resistivity values together with extreme resistivity gradients in both vertical and lateral directions. Resistivity anomalies associated with chamber tombs further appear rectangular in shape. At Mageiras-Kioupia, chamber

tombs were dug into a soft sandstone that overlies silt-dominated material, both belonging to the Vounargon stage of the Tertiary.

The study site at Epitalio is located at the fault scarp of a wide hilly region composed of the same Tertiary bedrock as at Mageiras-Kioupia. Based on the results of an archaeological survey during which remains of a chamber tomb were detected at the mid-slope position of a larger hill close to an asphalt road, the ERT-approach calibrated at Mageiras-Kioupia was applied in combination with detailed GPR studies. Altogether, 11 chamber tomb candidates were found, some of which show very high resistivity values indicating that chambers might be still intact and filled with air. Moreover, based on GPR data, it was possible to identify a 3D rectangular structure, indicating another air-filled cavity. By our study, we were thus able to detect and localize a new, most probably Mycenaean burial site near Epitalio by means of geophysical data for which no systematic archaeological information existed so far. Additionally, GPR and ERT data indicate the existence of large chamber tombs comparable with those found in Mageiras-Kioupia. However, to determine the exact size and shape of tombs an archaeological excavation would be necessary due to the fact that effective geophysical expression of a subsurface cavity often appears larger than the physical dimension of the cavity itself.

ERT-based prospection was also carried out further inland on the Dartisa plateau. Here, no chamber tomb candidates comparable to the ones excavated and measured at Mageiras-Kioupia and Epitalio, respectively, were identified. In contrast, we found geophysical evidence of shallow interferences in the sandstone unit, most probably associated with graves and/or hollows for storage reasons.

The combination of archaeological survey and geophysical, ERT- and GPR-based prospection turned out to be highly valuable in search of ancient burial sites as shown for this case study conducted in the environs of ancient Olympia.

3 Landscape reconstruction and major flood events of the River Main (Hesse, Germany) in the environs of the Roman fort at Großkrotzenburg[2]

Abstract. Detailed geoarchaeological studies were conducted at the Großkrotzenburg floodplain (Southern Hesse, Germany) in order to reconstruct the fluvial palaeogeography and search for Roman harbour installations. Another objective was to reconstruct the local flood history based on stratigraphic and geochronological data. Prospection based on electrical resistivity tomography, vibracoring and direct push electrical conductivity logging were carried out to detect and analyze subsurface stratigraphies. Altogether, 6 sediment cores, up to 7 m long, were drilled along transects along and perpendicular to the present course of the River Main. Based on sedimentological and geochemical data, we classified four sedimentary units. Vibracore data helped to detect the pre-Holocene bedrock topography and to differentiate between sedimentary facies. We present geophysical, sedimentary and geochronological evidence of a river channel right in front of the Roman fort that was probably active during Roman times. Moreover, we found another bridge pier candidate in the prolongation of a well-documented Roman bridge. Our findings further indicate that the northern riverbank has shifted towards south since Roman times. However, neither sedimentary nor archaeological evidence for harbour installations could be brought to light. Nevertheless, we assume that conditions favorable of a river harbour, namely permanent water flow and sufficient water depth, were guaranteed in front of the fort where an undercut slope was probably already existing during Roman times.

Several sequences of coarse-grained, sandy to gravelly river deposits were found associated with major flood events that affected the site at Großkrotzenburg during late Medieval and modern times. At that time, central Germany was repeatedly influenced by extreme meteorological conditions and associated extreme runoff events. Based on radiocarbon data we were able to define two periods of major flooding, namely between 1435 and 1484 cal AD and 1646-1792 cal AD. These periods are contemporaneous with periods of increased flood frequency in Central Europe, derived from historical sources, namely 1430-1460 AD and 1730-1790 AD. Based on sedimentary and geo-chronostratigraphic evidence, major flood events detected at the Großkrotzenburg alluvial plain are most probably related with the AD 1480, AD 1573 and AD 1780 events known from historical records. Our results document that few historical flood events controlled the overall development of the fluvial landscape at Großkrotzenburg at least since Roman times until the late 19th century, namely by eroding pre-existing fluvial deposits, accumulating thick sequences of event deposits and narrowing the riverbed. Since the late 19th century, river regulation measures severely changed the hydrological conditions of the River Main.

[2]This chapter is based on the paper by Obrocki, L., Becker, T., Mückenberger, K., Finkler, C., Fischer, P., Willershäuser, T., Vött, A. (2018a): Landscape reconstruction and major flood events of the River Main (Hesse, Germany) in the environs of the Roman fort at Großkrotzenburg. – Quaternary International, in press.

3.1 Introduction and historical background

Rivers and river landscapes provide access to important resources such as water, food, fertile soils etc. for human societies. In addition, rivers are important transport routes for travelling and trading (Guccione 2008, Viglione & Rogger 2015, van Lanen & Pierik 2019). Therefore, river environments allow for attractive living space so that people have settled close to rivers throughout all archaeological periods (Brown 1997, Hill 2014, van Dinter et al. 2017). This is also the case for the River Main near Großkrotzenburg and surrounding areas (Fig. 3.1). Here, the settlement history dates back to the Early Stone Age (Wolff 1903).

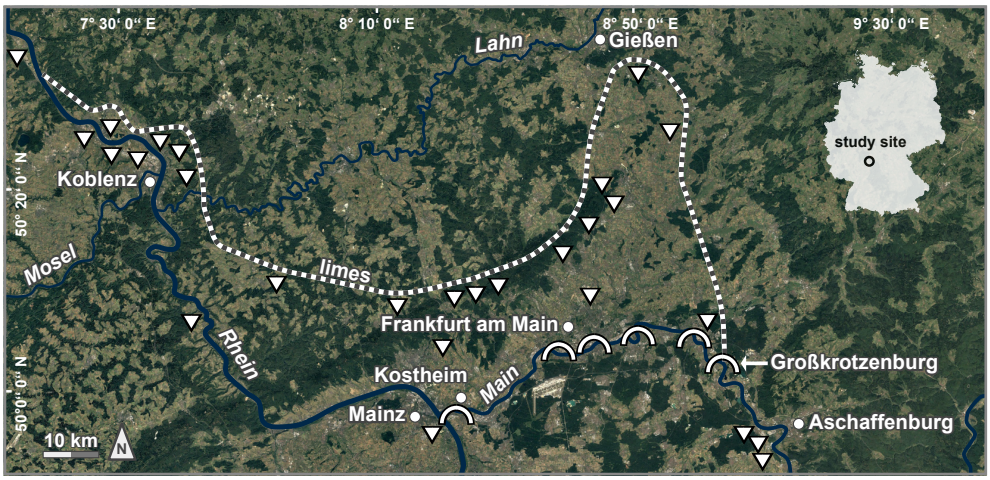

Fig. 3.1: Topographic overview of the wider study region showing sections of the Rivers Main and Rhine and the course of the Roman limes (white dotted line). The Roman fort at Großkrotzenburg is located where the limes meets the River Main the latter representing the border towards the east (so called Main Limes). White triangles show the distribution of tiles produced at the Roman fort at Großkrotzenburg. White half-circles mark the position of bridges of the River Main during Roman times (after Wolff 1903, Gündel 1922, Steidl 2008). Map modified after ESRI Vector Basemap 2013; Google Earth aerial images, 12/2016.

However, the area has become increasingly significant when it was occupied by the Romans around 100 AD, who built a fort at this place around 119-120 AD (Wolff 1903, Steidl 2008). Since the end of the 19th century AD, the Roman fort at Großkrotzenburg and the nearby limes have been excavated under the auspices of the Reichs-Limeskommission and later, by the hessenArchäologie (state monument protection service). The archaeological remains of the Roman fort are located in the immediate proximity of the edge of the lower terrace of the River Main (Becker 2014). Archaeological remains of five Roman bridge piers were found approximately 100 m downstream and let assume that the fort was directly facing the river during Roman times. Wooden posts, driven into the riverbed sediments, served as foundation for the bridge piers that were made out of sandstone (Stade 1933, Steidl 2008) (Figs. 3.2 and 3.3). Dendrochronological analyses of these wooden posts yielded an age of 134-138 AD (Steidl 2008). Trading goods transported from Mainz to the Spessart region, located to the northeast of Großkrotzenburg, document that the River Main was an important transportation route during Roman times (Steidl 2008). Additionally, archaeological excavations at Großkrotzenburg revealed the existence of a Severan brick

manufacture to the NE of the Roman fort that was operated by the cohort IIII Vindelicorum. Findings of bricks produced in Großkrotzenburg were made upstream the River Rhine up to Niedernberg and downstream the Main River up to Miltenberg and also along smaller rivers along the limes in the Wetterau (Steidl 2008, Wolff 1929) (Fig. 3.1). However, any evidence of harbour installations associated to the Roman fort at Großkrotzenburg is missing so far. It is assumed that there was a harbour at Großkrotzenburg or alternatively, a riverbank situation which allowed the landing of ships to load and unload bricks and other goods for transportation. Such landing sites are assumed for Bonn and Andernach along the River Rhine where the natural topography and the local flow regime allow the landing of ships without any harbour constructions (Roggenkamp 2016). Considering the weight of brick cargos as well as the risk of high-water pressure and flotsam during flood events, a quay wall seems to be the most plausible harbour installation for Großkrotzenburg, if any harbour installation ever existed at that Roman place. Quay walls are known features of Roman River ports at that time (Wawrzinek 2014). In Germany, Roman harbours with quay walls are known from Xanten and Kalkar along the River Rhine (Gerlach & Meurers-Balke 2014a) and also from Stockstadt, a Roman site at the River Main located some 15 km upstream of Großkrotzenburg (Drexel 1910). Although, at other locations along the River Rhine, e.g. at Köln (Cologne) and Königswinter, the river shore was stabilized only by stones to allow loading ships at any water level of the river channel (Roggenkamp 2016).

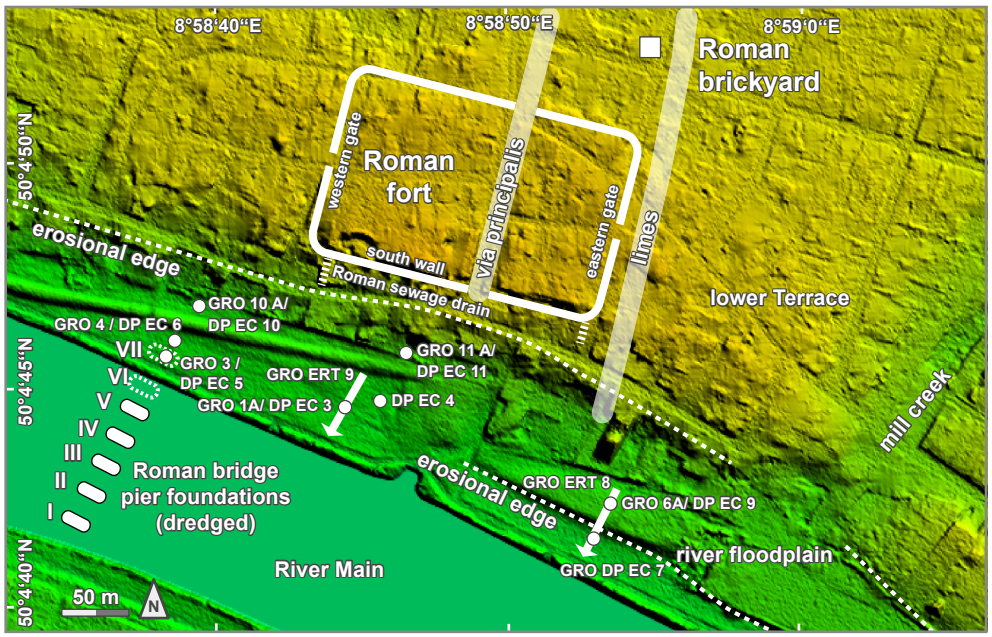

Fig. 3.2: Digital elevation model of the study area showing the position of the Roman fort as well as the location of vibracoring sites (GRO 1A, 6A 3, 4, 10A), DP EC logs (GRO DP EC 3, 4, 5, 6, 7, 9, 10, 11) and ERT transects (GRO ERT 8, 9). See text for further explanations. Map modified after Becker 2014.

Fig. 3.3: Photo of a wooden pile shoe of Roman bridge piers found in the riverbed of the Main River near the Roman fort of Großkrotzenburg. The wooden pile shoes, fortified by iron, were hit into the riverbed and covered by gravel and sand. The piers themselves were built on top of this foundation, consisting of sandstone. Photo by A. Vött.

Despite the advantages of living close to rivers, there is a considerable risk of flooding. Floods, considered to belong to the most widespread hazards in Europe, may have a destructive impact on human societies and infrastructure. They may also trigger changes of river dynamics and sedimentary and environmental conditions (Asselman & Middelkoop 1998, Baker et al. 2002, Brázdil et al. 2012, Glaser et al. 2010, Raška & Emmer 2014, Viglione & Rogger 2015, van Dinter et al. 2017). However, there are no high- water marks or historical data on ancient flood events available for the study site. But the fact that Roman forts in Germany were often built on the lower terrace generated during the last glaciation or at elevated areas and therefore protected from floods shows that the Romans were well aware of flood risks (Ollive et al. 2006, Roggenkamp & Herget, 2014, Roggenkamp 2016). On the contrary, the occurrence of flood events in Medieval and modern times is well documented for the major rivers in Germany (Glaser 2013, Herget et al. 2015). Local flood chronologies are mainly based on human observations such as written records, paintings, and flood marks on historical buildings (Kessler 1962, Gerlach 1995, Pfister 1999, Glaser et al. 2010, Herget et al. 2015) but also, to a lesser extent, on palaeoclimatological and geomorphological studies (Benito & Díez-Herrero 2015). Glaser (2012) observed an overall increase in the number of flood events in Central Europe since the 14th century AD. Moreover, Glaser et al. (2010) define four periods with intensive flood frequencies, namely 1540-1600 AD, 1640-1700 AD, 1730-1790 AD and 1790-1840 AD. With regard to the River Main, Glaser (2013) additionally mentions a higher frequency of floods for the periods between 1430-1460 AD and 1530-1600 AD. In this respect, it is worth noting that catastrophic flood events may have affected only a specific river section and not the entire catchment area. Effects of flood events are the result of a complex interaction of climatic conditions, the local topographical setting,

hydraulic dynamics and anthropogenic factors (Brázdil et al. 1999, Starkel 2002, Glaser 2012, Gębica et al. 2013, 2016, Rheinardt-Imjela et al. 2017). Historically, information on flood events is often restricted to large destructive floods that caused severe damage in settled areas. For this reason, smaller flood events or events in more remote areas have often remained unconsidered in historical flood chronologies (Brázdil et al. 1999, Herget 2012). Therefore, investigating historical water levels of a certain area is essential for the reconstruction of the local flood history (Baker 1987, Benito & Thorndycraft 2005, Herget 2012). Water level indicators comprehend sedimentary indicators such as flood sediments, erosional features and other traces of high-energy transport (Benito & Thorndycraft 2005, Herget 2012, Scheffer et al. 2014, Foulds et al. 2014, Toonen et al. 2015). Palaeoflood reconstructions are depending on the completeness and the time span recorded in fluvial sedimentary archives (see Brown 1997).

The main objectives of our study were (i) to reconstruct the local fluvial palaeogeography in the immediate environs of the Roman fort at Großkrotzenburg in search of an appropriate harbour situation using stratigraphic data, (ii) to decipher the local flood history based on sedimentary records and geophysical indicators of changing River Main dynamics in the study area (iii) and to evaluate the overall significance of fluvial sedimentary archives as a base to reconstruct the local landscape evolution since Roman times.

3.2 Regional setting of the floodplain at Großkrotzenburg

The study area in the environs of Großkrotzenburg is located at the northern riverbank of the River Main, approximately 6·5 km to the SE of the presentday city of Hanau near Frankfurt am Main (Southern Hesse, Germany) (Fig. 3.1). The River Main with its catchment of about 27 200 km^2 and a length of 530 km, is a main tributary of the River Rhine (Späth 1979). In its upstream section, the river is a typically mid-mountain river running through deeply incised valleys of the cuesta landscape of southwestern Germany. In contrast, the downstream section of the River Main near Hanau forms a transition towards a meandering system that evolved in a wide alluvial floodplain (Körber 1962, Brázdil et al. 1999) tectonically adjusted to the Upper Rhine graben. The natural flow regime of the River Main is controlled by precipitation, snow retention and snow melting, showing maximum discharge during November, December and March and minimum discharge during August and September (Keller 1979, Brázdil et al. 1999). The riverbank that is located to the immediate south of the modern village of Großkrotzenburg is a typical undercut bank associated with a meander of the River Main. The remains of the Roman fort are situated at the edge of the lower terrace about 6 m above the present river level and some 130 m distant to the recent riverbank. Remains of two Roman sewage systems were found some meters distant from the southern fortification wall in front of the fort documenting that the strip of land between the fort and the river channel was at least 15 m wide during Roman times (Becker 2014). However, the elevation of the sewage systems only yields information on the maximum water level of the river at that time and cannot be regarded as indicator of the mean water level. For this reason, estimating river channel incision since Roman times remains highly speculative. The recent

floodplain is bordered by a NW - SE trending erosional edge formed in material of the Lower Terrace (Hessische Geologische Landesanstalt 1922) (Fig. 3.2). Archaeological findings of six Roman bridges across the River Main between Großkrotzenburg and the confluence of the River Main into the River Rhine (Gündel 1922) (Fig. 3.1) document that there have been no major changes of the river course since Roman times. According to Schirmer (1983) and Gerlach (1995), the River Main was a broad and shallow river during Roman times that was characterized by the increasing deposition of loamy overbank deposits caused by deforestation. This human impact is made responsible for a considerable rise of the riverbed and, at the same time, a narrowing tendency of the river channel of the River Main during Medieval times (Kessler 1962). Today, both the channel architecture and the river discharge of the River Main are controlled by modern river regulation measures that were initiated in the late 19th century AD (Schüssler 2004).

3.3 Material and methods

Detailed geomorphological and sedimentological studies were carried out along the floodplain to the south of the Roman fort at Großkrotzenburg in order to reconstruct the local landscape dynamics. Electrical Resistivity Tomography (ERT) was conducted to obtain information on the alluvial stratigraphy and the local bedrock topography. Measurements were carried out using a Syscal R1 Plus Switch 48 multi-electrode system (IRIS Instruments) and a Wenner- Schlumberger electrode array with an electrode spacing of 1 m. ERT data were inverted using the RES2DINV software tool. We used ERT depth sections as a base to localize vibracoring sites enabling best-fit control of the underground architecture (Kirchner et al. 2018). Vibracores were drilled at 6 different sites using an automotive Nordmeyer RS 0/2.3 drill rig and 80 and 60 mm core diameters for a half-open steel auger (vibracores GRO 3, GRO 4) and 60 mm core diameter for a closed steel auger system with plastic inliners (vibracores GRO 1A, GRO 6A, GRO 10A, GRO 11A). Half-open sediment cores were cleaned, photo documented and described based on sedimentological and geomorphological criteria (Ad hoc-AG Boden 2005). Plastic inliner vibracores GRO 1A and GRO 6A were used for sampling and in situ measurements of geochemical and mineralogical parameters to distinguish between different stratigraphic units. Grain size analyses were conducted for 32 samples from core GRO 1A and 33 samples from GRO 6A using the Köhn sieving and pipette method (Köhn 1929, Barsch et al. 2000). Prior to grain size analysis of fine-grained material standard pre-treatment was carried out including dry-sieving in order to determine the amount of coarse material > 2 mm, followed by peptisation of the fraction < 2 mm in sodium pyrophosphate for 12 h. We determined percentages of eight grain size classes (clay: < 2 µm, fine silt: 2–6.3 µm, medium silt: 6.3–20 µm, coarse silt: 20–63 µm, finest sand: 63–125 µm, fine sand: 125–200 µm, medium sand: 200–630 µm, coarse sand: 630–2000 µm). For each sample, we calculated (mean) relative frequency distribution curves as well as cumulative frequency curves based on 99-step cosine interpolation function over the grain size classes. Colour spectroscopy (CIELAB colour space, see Scheinost & Schwertmann 1999, Viscarra Rossel et al. 2006) and magnetic susceptibility of sediment cores were measured with a resolution of 1 cm using a spectrophotometer (type Konica Minolta CM-600d) and a

Bartington MS2K surface sensor, respectively. Element concentrations were determined by X-ray fluorescence (XRF) in 2 cm steps using a handheld Thermo Scientific Niton Xl3t 900S GOLDD analyzer (calibration mode SOIL). We used a semi-quantitative approach based on element ratios to normalize XRF data and reduce the influence of masking effects related to differences in water content, sediment density, organic matter concentration and grain size (Weltje & Tjallingii 2008, Pantazis 2010, Sageman et al. 2013).

We also applied direct push electrical conductivity logging (DP EC) using a Geoprobe SC520 soil conductivity probe system adapted to our Nordmeyer drill rig RS 0/2.3 at eight different sites. Electrical conductivity of clastic sediment is mainly controlled by mineralogical characteristics, moisture and the chemical composition of the pore water (Schön 2015). In saturated sediments below the ground water table DP EC logs therefore show the change in sedimentary characteristics, if the differences in the chemical composition of pore water are negligible (Schulmeister et al. 2003, Harrington & Hendry 2006). Usually, low electrical resistivity values represent fine-grained sediments, such as clay and silt; in contrast, high electrical resistivity values are related to coarser sediments such as sand and gravel (Wunderlich et al. 2013, Fischer et al. 2016, Hausmann et al. 2018). The DP EC probe with four electrodes in a linear arrangement was operated using a Wenner array resulting in a vertical resolution of 2 cm (Harrington & Henry 2006). Using the DP EC system, electrical current and voltage are measured constantly with depth and electrical conductivity values are given in milli-Siemens per meter (mS/m, Direct Image 2008). The positions and absolute elevations of vibracoring and DP EC logging sites as well as ERT electrodes were measured by means of a differential GPS type Topcon HiPerPRO FC-250. Radiocarbon dating using the AMS technique was conducted for 15 samples, namely wood fragments, plant remains, and charcoal retrieved from cores GRO 1A, GRO 3, GRO 4 and GRO 6A. Radiocarbon dating was conducted at the Klaus-Tschira-Laboratory, Curt-Engelhorn- Zentrum für Archäometrie, Mannheim, Germany (MAMS). Calibrated ages were calculated using the Calib Rev 7.1 calibration software (Reimer et al. 2013).

3.4 Results

3.4.1 Vibracore transect across the River Main floodplain at Großkrotzenburg

Vibracores GRO 1A, GRO 6A, GRO 3, GRO 4 and GRO 10A were drilled along a NW-SE running transect across the floodplain of the River Main in the immediate environs of the Roman fort of Großkrotzenburg (Fig. 3.2). Stratigraphic changes in colour, grain size and texture are exemplarily depicted in Figs. 3.4 and 3.5 for selected vibracores. The stratigraphic record of the entire vibracore transect, schematically categorized in four sedimentary units (I-IV), is summarized in Fig. 3.10 based on grain size and colour. Vibracore GRO 6A (50° 04’ 42.069078” N, 08° 58’ 53.868627” E, ground surface at 103.79 m NN = m above sea level at Amsterdam, The Netherlands) was drilled in the eastern part of the study area to a depth of 7 m below surface (m b.s.).

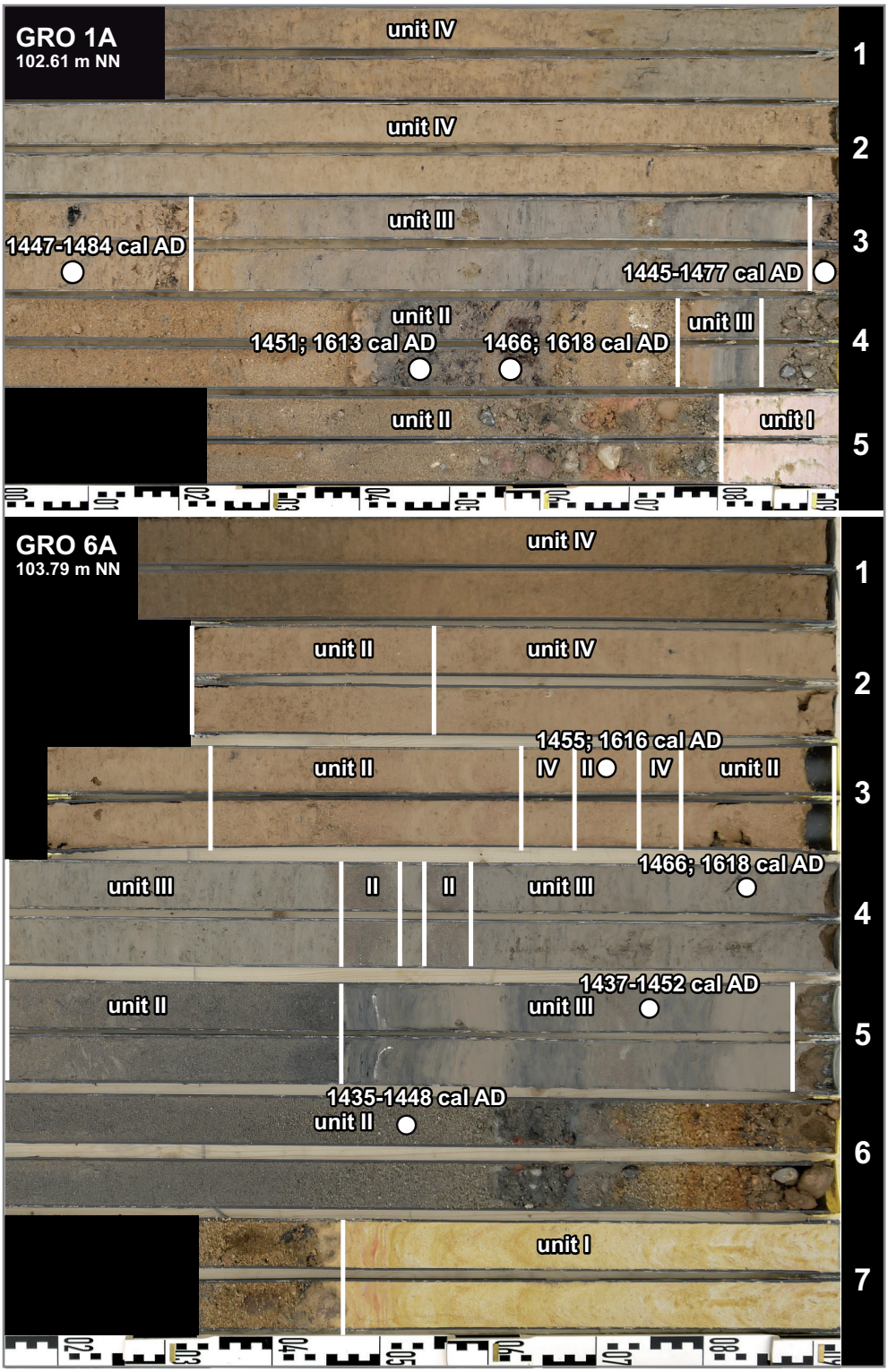

Fig. 3.4: Photo of vibracores GRO 1A and GRO 6A drilled in the floodplain of the River Main in front of the Roman fort at Großkrotzenburg. Note: Unit I – Tertiary bedrock, Unit II – channel sand and gravel, Unit III – quiet reach silt, Unit IV – floodplain silt. Photo by T. Willershäuser.

The vibracoring location is situated on the top of a fluvial terrace delineated to the east by an erosional edge, c. 1.5 m high (Fig. 3.2). At the base of the profile (96.79 to 97.32 m NN), we found intensely weathered Tertiary sandstone (unit I). Towards the top, the stratigraphic pattern can be divided into three different sedimentary units. On top of the bedrock, we found coarse sand and gravel (unit II) up to 98.91 m NN, beige to brownish red in the lower part and dark grey in the upper part with an intersected silt layer, 2 cm thick (98.10 to 98.12 m NN). Subsequently, we encountered a thick sediment layer out of clayey silt, light grey in colour (unit III). This unit locally contains high organic content as well as repeated intersections of coarser grained sediment layers, up to 35 cm thick. These coarser deposits are characterized by a high content of medium sand (unit II) with a high concentration of calcium carbonate and large amounts of mica. Moreover, we found characteristics of reworking processes such as silt clasts and basal erosional unconformities. At 100.79 m NN a clear change in colour from light brown to dark brown marks the boundary to unit IV out of sandy silt, clayey silt and silty fine sand with oxidation features such as Fe and Mn nodules. This section also shows several intersections by coarse-grained sediment at 101.01 m NN, 101.45 m NN and 102.47 m NN. Vibracore GRO 1A (50° 04’ 44.623443” N, 08° 58’ 44.871045” E, ground surface at 102.61 m NN) was drilled in the central study area in the direct prolongation of the via principalis of the Roman fort. In contrast to vibracoring site GRO 6A, the Tertiary bedrock shows a higher degree of weathering consisting of compact silty clay (unit I). The bedrock is covered by light brown sand and gravel up to 99.71 m NN (unit II). Within this section, we found an interesting layer out of grey to reddish brown clayey silt at 98.76 to 98.86 m NN covered again by coarse sand. Additionally, at 99.01 to 99.23 m NN, the core shows a layer of grey, fine to medium sand with a high content of plant remains and a mud cap on top. Analogous to vibracore GRO 6A, unit II is covered by thick layer of clayey silt (unit III, 99.71 to 100.40 m NN). The latter is partly intersected by coarser-grained deposits partly showing lamination, increased content of calcium carbonate and high amount of mica. The upper part of the vibracore is characterized by a thick layer of homogenously brown silty clay (unit IV, 100.40 to 102.61 m NN) and locally intersected by unit II layers similar to vibracore 6A. This quadripartite structure of the sedimentary sequence was also found at vibracoring site GRO 10A located some 80 m SW to the fort in the direct northern extension of the Roman bridge piers (50° 04’ 46.516800” N, 08° 58’ 40.350000” E, ground surface at 103.28 m NN). However, bedrock unit I comes closer to the surface reaching 99.40 m NN. Subsequently, it is covered by a thin layer of reddish-brown sandy gravel (unit II). Towards the top, grey predominant silty clay (unit III) was found with only few intersecting layers of coarse-grained sediments. Similar to core GRO 1A, the upper part of the core shows homogenously brown silty clay deposited by floodplain dynamics (unit IV).

Vibracores GRO 3 (50° 04’ 45.660224” N, 08° 58’ 39.589370 E, ground surface at 102.62 m NN) and GRO 4 (50° 04’ 45.930487” N, 08° 58’ 39.754413” E, ground surface at 102.76 m NN) were drilled between the northernmost known Roman bridge pier and vibracoring site GRO 10A (Fig. 3.2). At both locations, we did not reach the Tertiary bedrock. The lower part of core GRO 3 contains red sandstone fragments that are angular and therefore seem not to be transported by fluvial processes (Fig. 3.5; A).

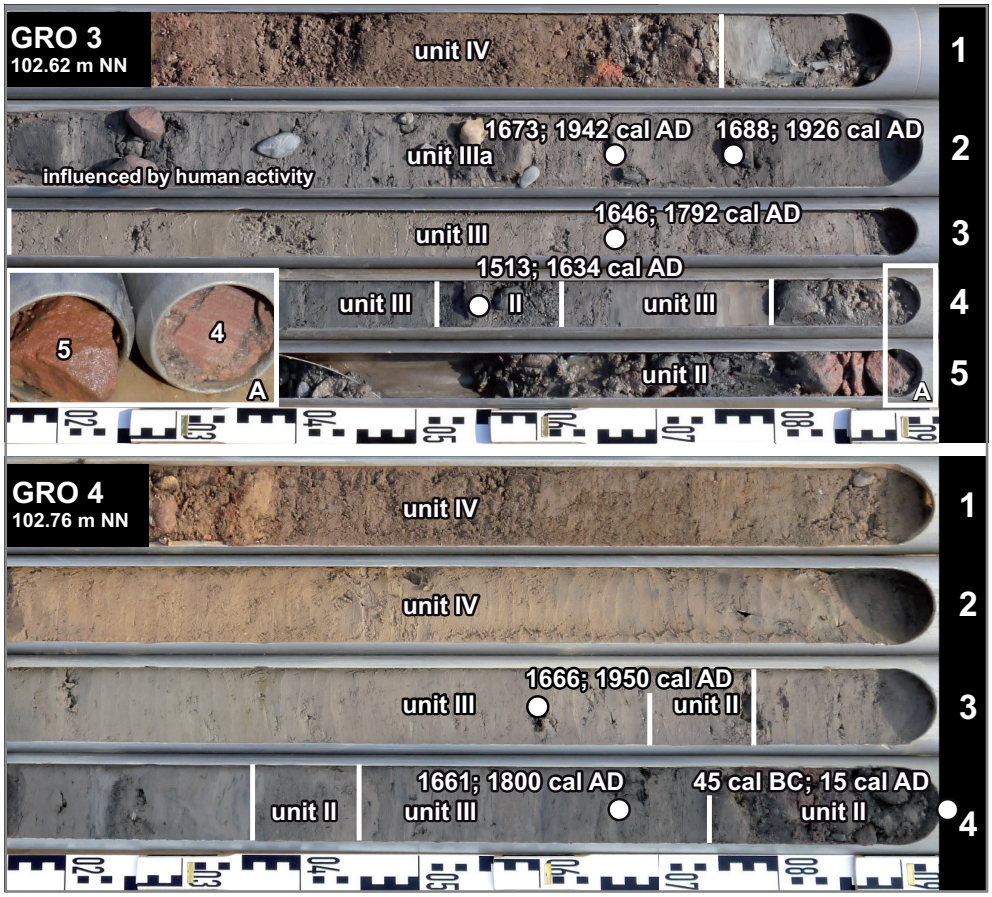

Fig. 3.5: Photos of vibracores GRO 3 and GRO 4 drilled in the floodplain of the River Main in front of the Roman fort at Großkrotzenburg. Note: Unit I – Tertiary bedrock, Unit II – channel sand and gravel, Unit III – quiet reach silt, Unit IIIa – anthropogenically disturbed layer, Unit IV – floodplain silt. Photos by A. Vött.

Up to 98.82 m NN, we found a subsequent layer out of gravel made out of sandstone (unit II). Following a basal erosional unconformity, we encountered a section of silty clay (unit III). The lower part of unit III shows higher contents of organic material and is intersected by a layer of gravelly medium sand (98.96 to 99.11 m NN).

Further upcore, a mixture of clayey silt and gravel documents human influence (Unit IIIa). Towards the top, we found brown floodplain silt corresponding to unit IV. At vibracoring site GRO 4, we encountered well rounded gravel embedded in coarse sand (unit II) and, on top of a sharp erosional contact, a thick layer of silty clay (unit III). The latter is intersected by a thin layer of sandy silt at 99.98 m NN. Finally, a change in colour from dark grey to dark brown and increasing numbers of oxidation features mark the transition between unit III and unit IV in the uppermost part of the core.

In a summary view, stratigraphic data of the River Main floodplain at Großkrotzenburg display a high variability documenting rapid changes in fluvial geomorphodynamics. We found fine-grained sediments out of clayey silt that reflect periods of low-energy depositional dynamics. However, we did not found palaeosol candidates that would represent stable surfaces over

a certain period. Phases of low-energy sediment deposition were repeatedly interrupted by phases of high-energy dynamics causing both erosional features and the accumulation of coarse-grained deposits in the stratigraphic record; the latter document the temporary influence of high-energy river channels of the River Main.

3.4.2 Multi-proxy approach: implications from sedimentological, mineralogical and geochemical analyses

Results of grain size studies as well as of in situ geochemical and geophysical analyses are illustrated in Fig. 3.6 showing subsurface conditions of the River Main alluvial plain right in front of the via principalis and east of it.

Unit II deposits out of medium and coarse sand dominate the lowermost parts of both profiles. Relative frequency distributions and the mean cumulative frequency obtained for unit II samples show that the sand fraction is predominant but overall the sorting of sediments is poor (Figs. 3.7B and 3.8B). Strong variations of the grain size distribution were found for sections 99.61 to 100.81 m NN and 98.91 to 101.45 m NN at sites GRO 1A and GRO 6A, respectively (Fig. 3.6). Coarse-grained layers intersecting silt-dominated deposits of unit III are characterized by up to 60% medium sand documenting temporary shifts from low-energy to high-energy depositional conditions. Sediment samples from unit III also appear poorly sorted but mostly show a clear maximum peak for coarse silt when compared to unit II deposits (Figs. 3.7C and 3.8C). Site-specific variations of local grain size distribution are also reflected by in situ electrical conductivity values logged by direct push sensing and converted into direct push resistivity values. The latter increase with increasing contents of medium and coarse sand and reach maximum values for unit II sediments on the top of the Tertiary bedrock where the amount of coarse sand is highest (Fig. 3.6). Homogeneous sections dominated by fine-grained deposits of unit IV with 70-90% or 40-65% silt and clay at sites GRO 1A and GRO 6A, respectively, show uniformly low resistivity values. In addition, relative frequency distribution curves reveal that samples from site GRO 1A are comparatively well sorted (Fig. 3.7D). These deposits reflect a low-energy depositional environment. Selected geochemical parameters also document rapid changes of environmental conditions in the investigated area. Unit IV sediments are characterized by a homogeneous curve shape of the K/Ti ratio. For site GRO 1A, the overall pattern of the K/Ti ratio remains constant until 99.55 m NN. In contrast, a strong increase of the K/Ti ratio and increasing fluctuations between positive and negative peaks characterizes unit II in the lower part of vibracore GRO 1A. For core GRO 6A, comparable results were found. Coarse-grained layers are related to maximum peaks whereas fine-grained deposits of unit III and IV reach minimum values. Concerning spectroscopic data, the amount of the red component is represented by the a* value in the L*a*b* CIELAB colour space. The sedimentary sequence of core GRO 6A shows a decrease of a* values downwards from 100.79 m NN where we found the transition between unit III and unit VI deposits. In contrast, sands and gravels of unit II as well as bedrock unit I show considerably increased a* values. However, the vertical distribution of a* values found for core GRO 1A is much more complex and does not follow a clear structure. Only unit III sediments show decreasing a* values as observed for vibracore GRO 6A.

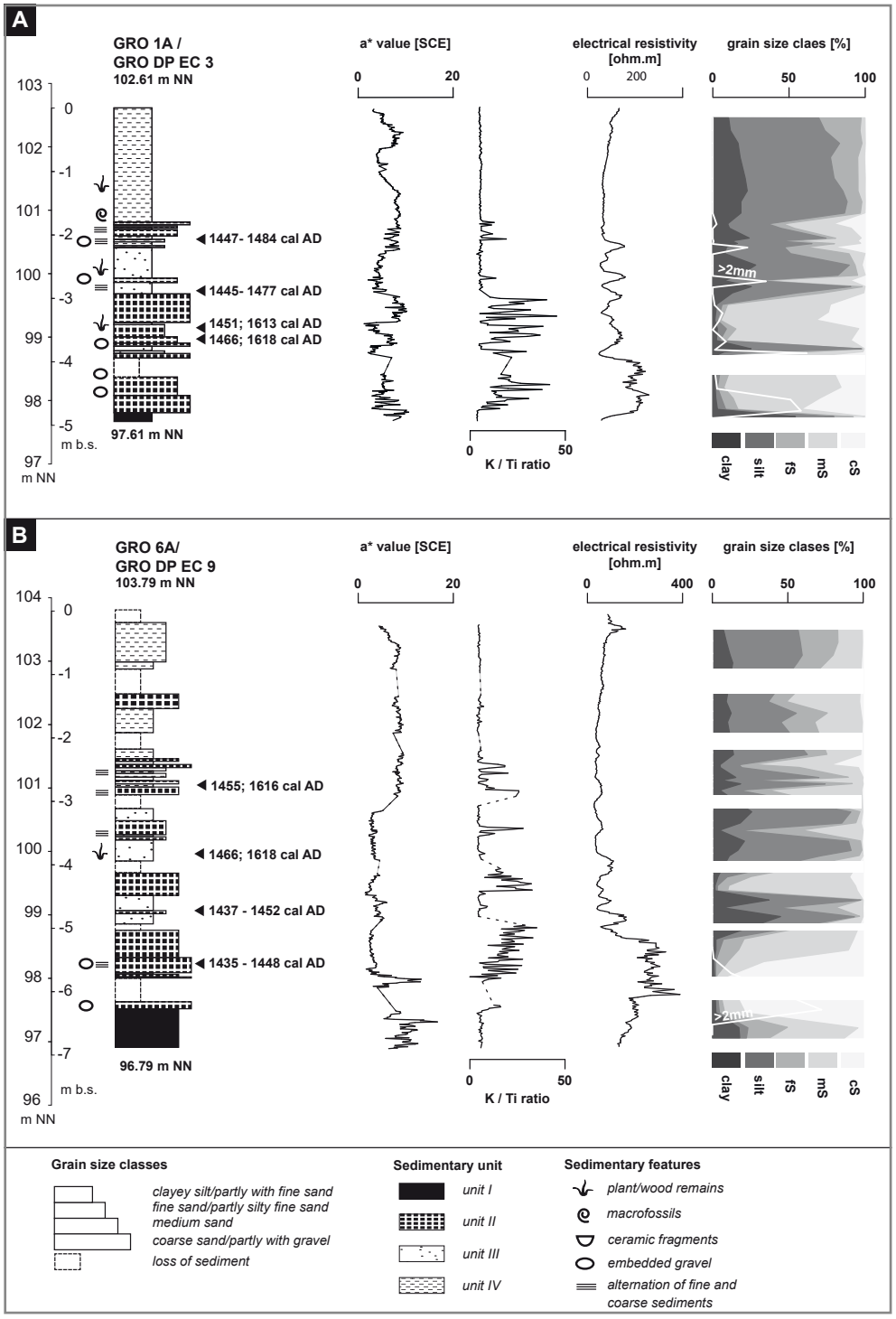

Fig. 3.6: Detailed stratigraphy of vibracores GRO 1A (A) and GRO 6A (B) showing colour spectroscopic data (CIELAB colour space, +a* = red, -a* = green), the K/Ti ratio, magnetic susceptibility values and grain size data. Core GRO 1A was drilled right in front of the via principalis of the Roman fort. See text for further explanations.

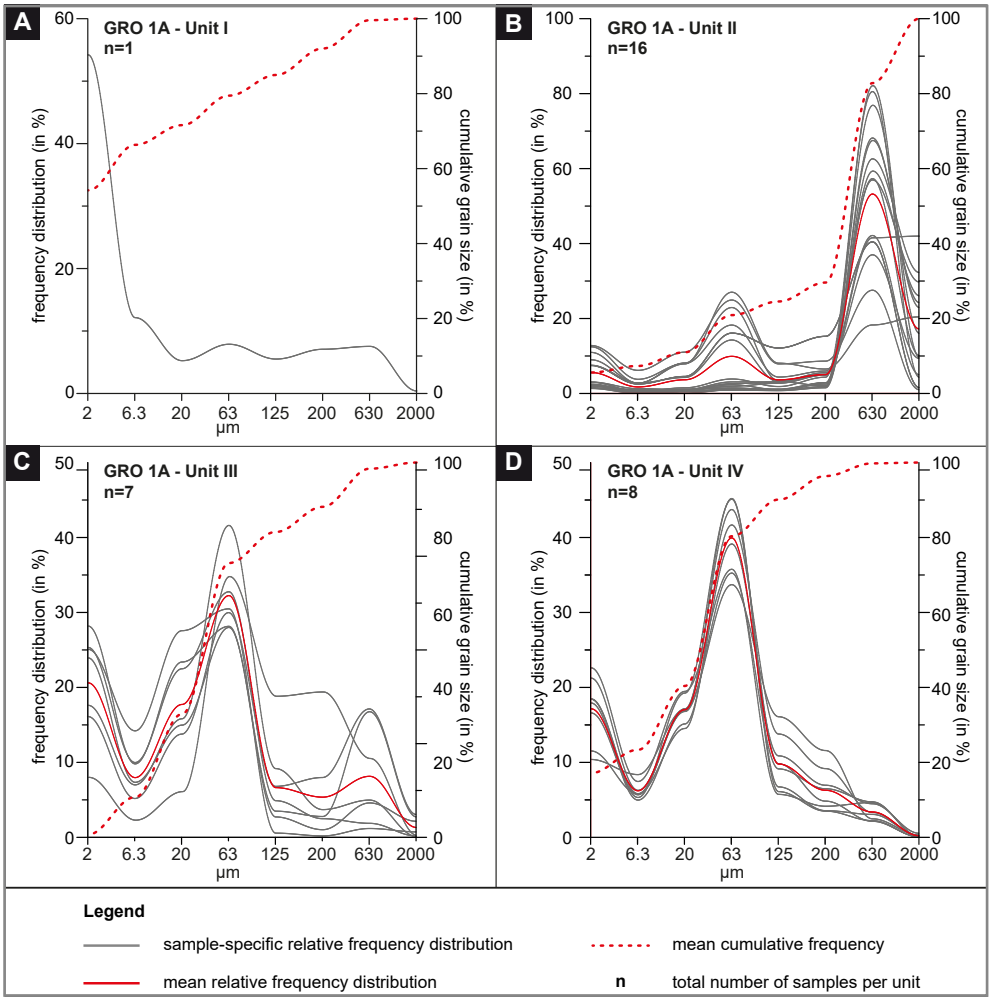

Fig. 3.7: Grain size data obtained for vibracore GRO 1A showing relative frequency curves for each sample classified according to units I, II, III and IV. Additionally, curves for the mean relative distribution frequency and the mean cumulative frequency are given for each sedimentary unit.

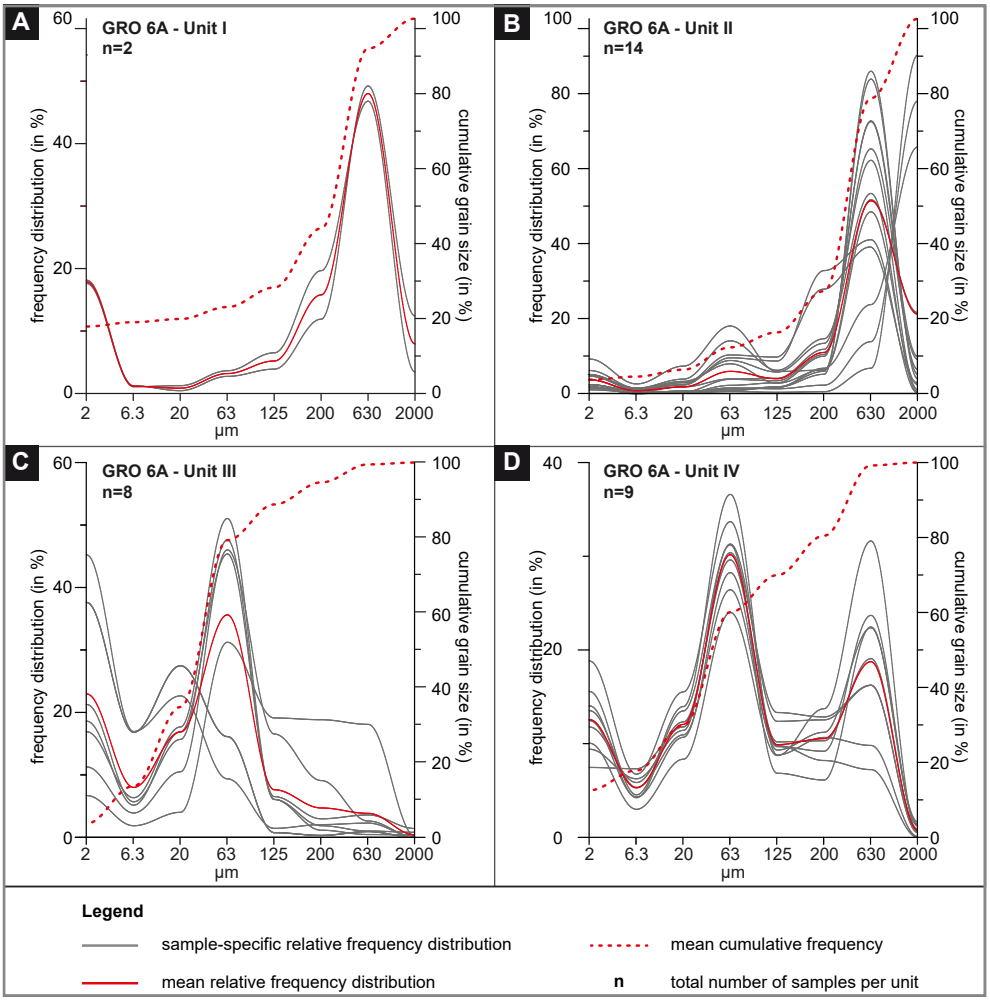

Fig. 3.8: Grain size data obtained for vibracore GRO 6A showing relative frequency curves for each sample classified according to units I, II, III and IV. Additionally, curves for the mean relative distribution frequency and the mean cumulative frequency are given for each sedimentary unit.

3.4.3 Site prospection based on ERT and DP EC measurements

In this paper, we present two selected ERT transects running parallel to each other from NE to SW across the River Main floodplain near Großkrotzenburg. ERT transect GRO ERT 8 crosses the erosional edge in the southeastern part of the study area and transect GRO ERT 9 is located directly south to the via principalis of the Roman fort (Fig. 3.2). ERT depth sections, compared with results of DP EC logging (converted to resistivity values) and schematic position of sedimentary units I to IV, are illustrated in Fig. 3.9. Transect GRO ERT 8 yielded a lower zone with very high resistivity values (≥120 Ω m), an intermediate zone with mid to high values (80-100 Ω m) and an upper zone of low electrical resistivity values (≤40 Ω m; Fig. 3.9, top). In general, results of ERT measurements are corroborated by DP EC sensing values, the latter showing a much better resolution and a higher reliability towards greater depths. DP resistivity values very well reflect the four sedimentary units described on the base of vibracore stratigraphies. DP resistivity curves, calibrated with sediment logs, document

well the depth of the local bedrock surface represented by decreasing values. Two channel structures can be identified that are separated from each other by the emerging bedrock and show considerable difference in the sedimentary filling. A channel between distance meters 30 and 40 along transect GRO ERT 8 and location of GRO DP EC 7 shows maximum resistivity values reflecting coarse-grained deposits. In contrast, another, wider channel at the northwestern end of the ERT transect corresponds to the stratigraphy of vibracore GRO 6A with coarse-grained unit II sediments (high DP resistivity values) and following thick fine-grained units III and IV (low DP resistivity values). ERT transect GRO ERT 8 reveals a relief inversion meaning that the terrace surface around vibracoring site GRO 6A lies on top of a palaeo-channel (Fig. 3.9, top).

ERT transect GRO ERT 9 generally shows a narrower range of absolute resistivity values which is also reflected by DP resistivity values. However, analogous to transect GRO ERT 8, highest resistivity values reflect coarse-grained unit II sediments. Resistivity values of GRO DP EC 4 mirror a coarse-grained channel fill with maximum grain sizes encountered at the base of unit II deposits. It is followed by unit III sediments with generally lower resistivity values. The DP resistivity log finally shows that, towards the surface, unit IV sediments are characterized by minimum resistivity values (Fig. 3.9, bottom).

GRO vibracores revealed local variations of the Tertiary bedrock ranging from marl to sandstone. Differences in the relative grain size distribution may also be due to different degrees of weathering at sites GRO 1A and GRO 6A (Figs. 3.7A and 3.8A). However, comparing DP logs with cores revealed that bedrock surfaces generally produce a strong decrease, locally even a minimum, of DP resistivity values.

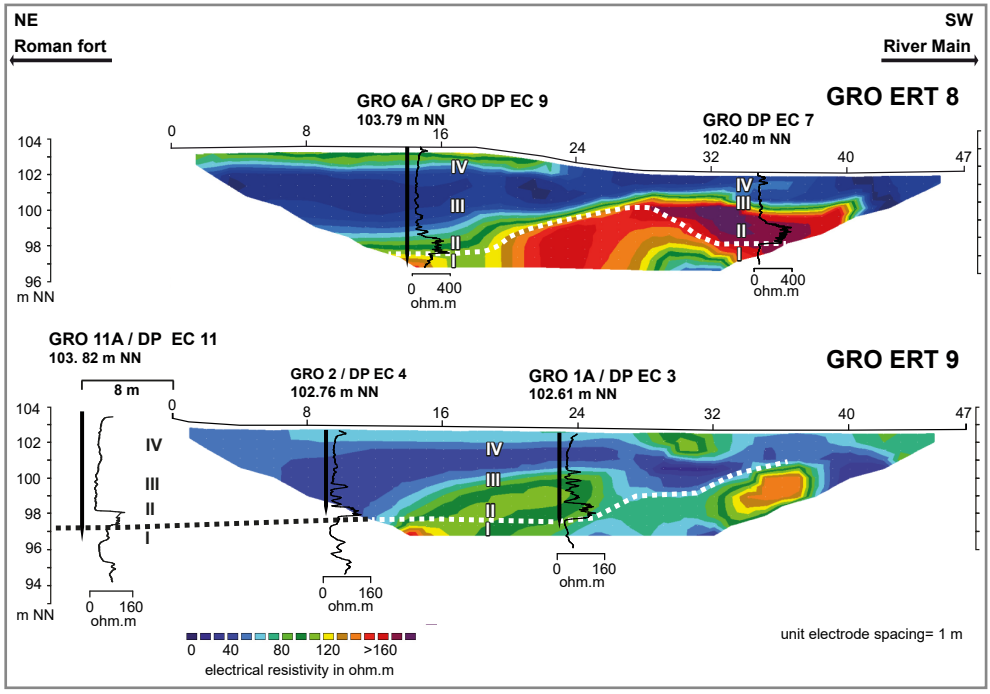

Fig. 3.9: Depth sections of electrical resistivity measurements conducted along transects GRO ERT 8 and GRO ERT 9. For location of transects see Fig. 2. See text for further explanations.

Therefore, DP resistivity logs GRO DP EC 11, 4 and 3 give evidence of a submerging bedrock topography towards the NE, similar to what was found along transect GRO ERT 9. Exemplarily, DP resistivity log GRO DP EC 11 revealed maximum values for unit 2 deposits right on top of the bedrock and homogeneous values for both unit III and unit IV (Fig. 3.9).

3.4.4 Radiocarbon dating

Tab. 3.1 shows the results of radiocarbon dating of 15 samples. These samples consisted of wood fragments, unidentified plant remains and charcoal fragments. If possible, we preferred retrieving radiocarbon samples from unit II and unit III. Doing so, we were able to achieve age estimates for two different sediment accumulation processes for the study site. Beside one Roman age, all radiocarbon ages are young lying between Medieval and modern times. Radiocarbon ages document both several hiatuses and high rates of sedimentation and are thus characteristic for incomplete fluvial sedimentary archives. Detailed discussion of the local geochronology is given in chapter 3.5.1.

Sample	Lab. No.(CEZ)	Depth (m b.s)	Depth (m NN)	Sample description	Unit	$\delta^{13}C$ (ppm)	^{14}C Age (BP)	1 σ max; min (cal BC/AD)	2 σ max; min (cal BC/AD)
GRO 1A/12 PR 2.08	28552	2,08	100,53	plant remain	IV	-22,9	399 ± 22	1447 - 1484 AD	1441; 1617 AD
GRO 1A/20 HR 2.92	28553	2,92	99,69	wood remain	III	-27,3	405 ± 22	1445 - 1477 AD	1477; 1616 AD
GRO 1A/24 HR 3.46	28554	3,46	99,15	wood remain	II	-30,1	384 ± 22	1451 ; 1613 AD	1445; 1622 AD
GRO 1A/24+ HR 3.57	28555	3,57	99,04	wood remain	II	-29,5	365 ± 22	1466; 1618 AD	1453; 1631 AD
GRO 3/HR 3 1.67	28557	1,67	100,95	wood remain	III	-25,6	159 ± 22	1673; 1942 AD	1667; 1950 AD
GRO 3/HR 4 1.77	28558	1,77	100,85	wood remain	III	-27,6	119 ± 22	1688; 1926 AD	1681; 1937 AD
GRO 3/HR 5 2.68	28539	2,68	99,94	wood remain	III	-27,8	242 ± 21	1646; 1792 AD	1641; 1950 AD
GRO 3/HR 8 3.56	28540	3,56	99,06	wood remain	II	-29,6	329 ± 22	1513; 1634 AD	1486; 1641 AD
GRO 4/HR 1 2.60	28541	2,60	100,16	wood remain	III	-28,8	184 ± 22	1666; 1950 AD	1662; 1950 AD
GRO 4/PR 3 3.65-3.68	28542	3.65 - 3.68	99.11 - 99.08	plant remain	III	-32,9	202 ± 22	1661; 1800 AD	1652; 1950 AD
GRO 4/HR 6 3.99	28543	3,99	98,77	wood remain	II	-29,3	2018 ± 24	45 cal BC -15 AD	89 BC; 53 AD
GRO 6/HK 1 2.72	28545	2,72	101,07	charcoal	IV	-26,8	375 ± 22	1455; 1616 AD	1448; 1629 AD
GRO 6/PR 3 3.84	28546	3,84	99,95	plant remain	III	-26,2	365 ± 21	1466; 1618 AD	1453; 1631 AD
GRO 6/HR 1 4.75	28547	4,75	99,04	plant remain	III	-26,8	439 ± 21	1437 - 1452 AD	1428 - 1469 AD
GRO 6/PR 5 5.53	28548	5,53	98,26	wood remain	II	-29,2	450 ± 21	1435 - 1448 AD	1423 - 1459 AD

Tab. 3.1: Radiocarbon dating results of samples from vibracores drilled at Großkrotzenburg. Note: Lab. No. (CEZ) – laboratory number, Curt-Engelhorn-Zentrum für Archäometrie, Mannheim, Germany; b.s. – below ground surface; m NN – m above sea level at Amsterdam, The Netherlands; unit – stratigraphical unit; 1σ max; min (cal BC/AD) – calibrated ages, 1σ-range; (; – several possible age intervals) 2σ max; min (cal BC/AD) – calibrated ages, 2σ-range; (; – several possible age intervals). Calibration based on Calib Rev 7.01 with IntCal 13 dataset (Reimer et al. 2013).

3.5 Discussion

3.5.1 Geochronostratigraphy and reconstruction of major river flood events

The overall stratigraphic record of the Großkrotzenburg floodplain is characterized by a high complexity of sedimentary sequences along the vibracore transect (Fig. 3.10). Unit I deposits, representing the local Tertiary bedrock, show a diverse texture and composition due to local lithological differences and differences in the degree of weathering. Unit II sediments consist of medium to coarse sand and gravel characterized by poor sorting. We consider unit II sediments as corresponding to a high-energy fluvial facies (Brown 1997) of the River Main. It was found at all investigated sites directly on top of the bedrock and intersecting unit III sediments. Moreover, our data show that the frequency and thickness of coarse-grained intersections decrease with increasing distance to the present river course (GRO 10A, GRO DP EC 11). The delivery of fresh detrital and differentially weathered material is also underlined by increasing values of K/Ti ratio (Mischke et al. 2010) measured for the coarse-grained sections of vibracores GRO 1A and GRO 6A. In contrast, low values of the K/Ti ratio are an indicator for enhanced weathering as found for units III and IV. We define unit III as a quiet reach silt that accumulated under reducing conditions below the water level. In contrast, unit IV deposits are interpreted as floodplain silts that developed in an oxidizing environment. The transition zone from unit III to unit IV was found in a constant position across the floodplain at c. 101 m NN reflecting uniform geomorphological conditions for the last accumulation phase of Holocene sequence. The delimitation of unit IV is based on the extremely homogenous curve shape of the K/Ti ratio, sediment colour and hydromorphic characteristics due to oscillating ground water. Both unit III and IV reflect the silting up of the river floodplain and the transition from a permanently inundated to a mostly dry floodplain system (Mischke et al. 2010, Turner et al. 2015). Only at site GRO 6A, unit IV deposits contain a higher amount of fine and medium sand and an intersecting layer of medium sand at 102.40 m NN. This elevation correlates with the base of a local erosional edge which we assume to be related to historic flood events that took place during (sub-) recent times, namely after 1455-1616 cal AD, which is the age of the uppermost GRO 6A radiocarbon dated sample (Figs. 3.4 and 3.10). At vibracoring site GRO 3, we found a disturbed unit IIIa layer at 100.62 m NN that was dated to 1673-1942 cal AD. Further, at vibracoring site GRO 4 we found a sharp contact between unit II and unit III that revealed radiocarbon ages of 45 cal BC - 15 cal AD and 1661-1800 AD, respectively. We interpret this hiatus of around 1800 years, together with the disturbed layer encountered in vibracore GRO 3, as the result of major river work measures in the late 19th century AD at the Großkrotzenburg floodplain (Stade 1933). By these melioration measures, dredging contacts were formed and older material was locally taken up and subsequently incorporated in younger sediments, for example the radiocarbon sample dating to 1661-1800 AD.

Regarding unit II sediments, it is crucial to consider the total sedimentary sequence. Doing so, it is possible to separate bed load deposits documenting an active river channel from slack water sediments that were deposited during flood events when flows go overbank or river channels become inactive (Baker 1987, Benito et al. 2003, Wolf & Faust 2016). Slack water deposits are composed of fine-grained material that accumulate out of suspended material

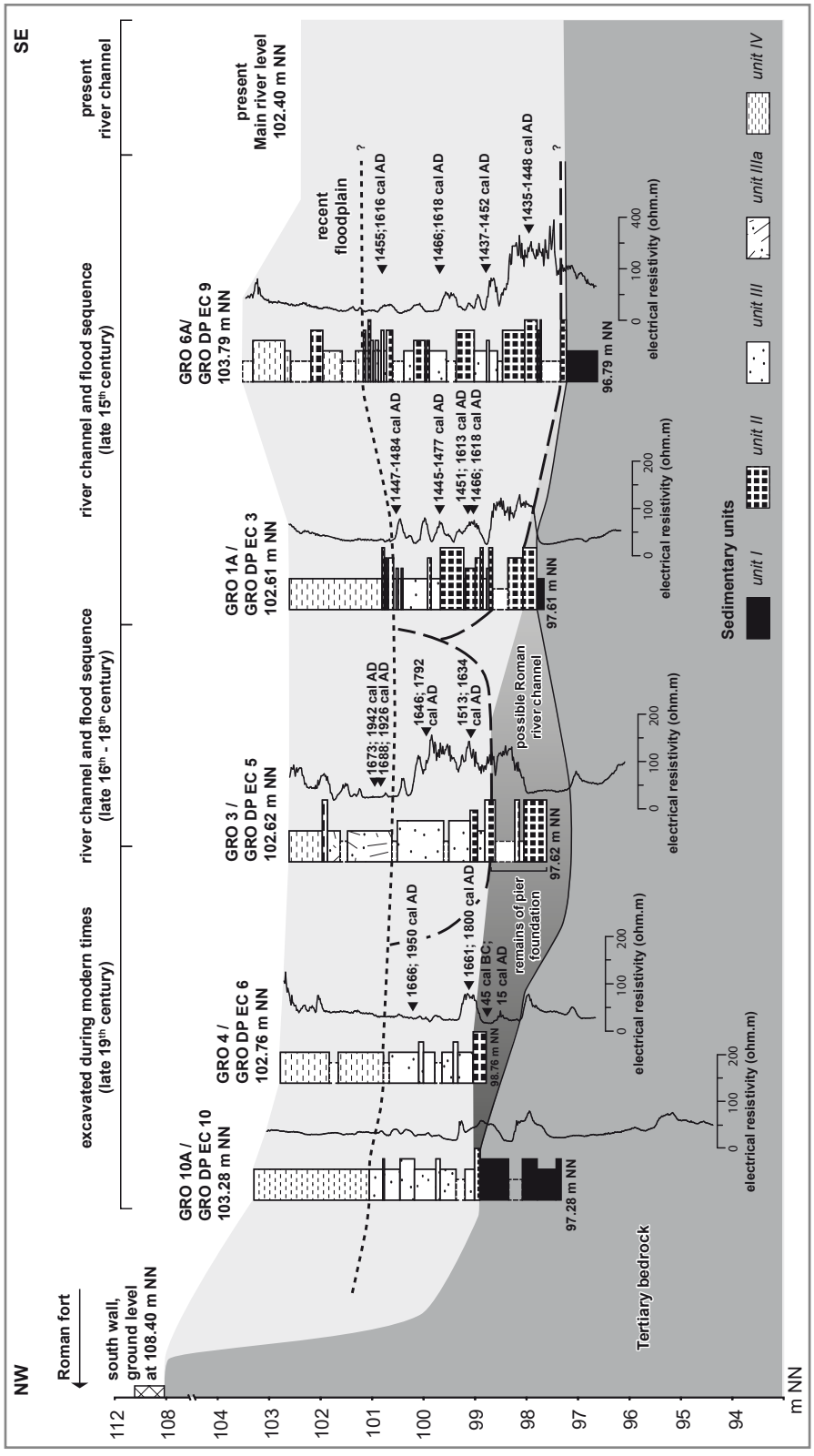

Fig. 3.10: Stratigraphical cross-section across the River Main floodplain based on vibracores and DP EC logs. Radiocarbon ages are summarized in Table 3.1. See text for further explanation.

during or after flood events. Sediment accumulation is generally expected to increase with the number of flood events and depending on the distance from the main river channel where water stagnation might occur (Asselman & Middelkoop 1998, Benito & Thorndycraft 2005, Schneeweiss & Schatz 2014). We found thick sediment sections accumulated within a very short time span, namely at sites GRO 1A and GRO 6A. Both sections show strongly oscillating grain sizes and geochemical parameters, erosional unconformities at the base of coarse-grained sub-sections, incorporated clasts of reworked underlying material, and partly enriched organic material derived from flotsam, and mud caps on top of high-energy layers. These features are typical of high-energy inundation as related with river floods (Berner et al. 2012, Benito & Díez-Herrero 2015). Unit III sediments document phases of reduced flow energy; however, evidence of soil formation is missing that would indicate geomorphological stability under oxic conditions and the beginning of soil formation processes, for example between two flood events. Therefore, we assume that units II and III represent successive inundation events. Organic samples retrieved from high-energy unit II as well as low-energy unit III yielded identical ages within the range of errors framing a time period of approximately 1435-1618 cal AD (Fig. 3.11, shaded in light grey; Tab. 3.1). The statistical probability was found highest for the time period 1435-1484 cal AD (Fig. 3.11, shaded in dark grey; Tab. 3.1). Based on these results, we suggest that the accumulation of unit II and III sediments at sites GRO 1A and GRO 6A were triggered by one flood event. It is known from historical sources that in 1480 AD, a large flood occurred causing strong inundation along the rivers Main and Rhine. The 1480 AD event, therefore, fits well with the chronological spectrum of the flood sequence encountered at Großkrotzenburg. Beside this event, numerous further flood events are reported for the 15th century (Kessler 1962, Schüssler 2004, Herget 2012). The flood sequence encountered at Großkrotzenburg is chronologically also consistent with a period of high flood frequency reported for the River Main by Glaser (2013) for the time period 1430 to 1460 AD (Fig. 3.11). Conclusively, our data show that the study site experienced major river flood impact during the time period 1435-1484 cal AD. Considering the aligned median values of radiocarbon ages depicted in Fig. 3.11, flooding was most probably associated with the AD 1480 event. However, we cannot exclude that it was (also) associated to the period of increased flooding activity between 1430 and 1460 AD reported by Glaser (2013).

Basal unit II sediments consist of coarse sand and gravel embedded at site GRO 6A and medium sand and gravel at site GRO 1A. They document bed load transportation of coarse clasts by high-energy water fluxes. However, a clear differentiation between regular channel deposits and flood deposits is not possible. We assume that the basal sand and gravel section, found at all investigated sites, represents a palaeo-channel of the River Main. We further suggest that channel deposits reflect different stages because consistent indicators of one and the same palaeostage were not found.

Moreover, the detection of the local bedrock topography (unit I) helped to reconstruct the local palaeogeography and revealed the existence of a channel-like structure to the north of the recent river course. This channel-type structure is also depicted in ERT transects. It runs parallel to the Roman fort, found deepest near sites GRO 6A (97.32 m NN) and DP EC GRO 11 (97.60 m NN) to the south of the via principalis (Figs. 3.9 and 3.10) with a maximum distance

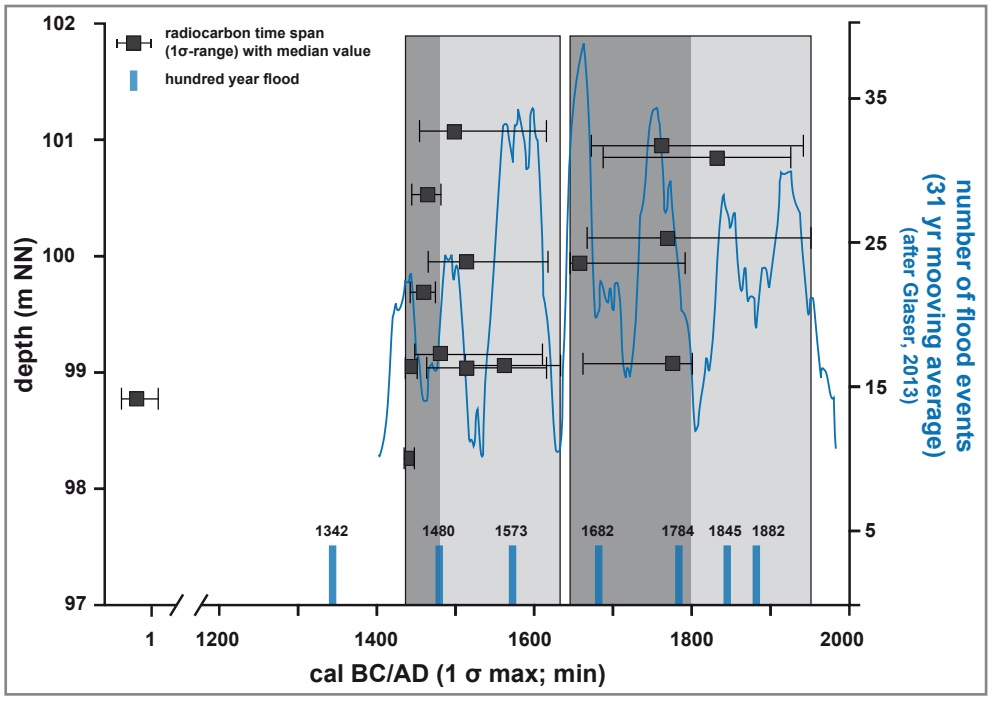

Fig. 3.11: Age-depth relation of radiocarbon dated samples retrieved from vibracores at Großkrotzenburg compared with the number of flood events along the River Main as known from historical sources (Kessler 1962, Glaser et al. 2010, Herget 2012, Glaser 2013). See text for further explanations.

of c. 75 m to the present riverbank of the River Main. At vibracoring sites GRO 3 and GRO 4, we were also able to detect coarse sand and gravel (unit II) at the lowermost part of the cores. This result indicates a possible continuation of the channel that was found at vibracoring sites GRO 1A and GRO 6A. We suggest that the deepest part of the channel is located at site GRO 3 where bedrock has not been recovered. However, based on our data, we do not know whether the channel represented the main channel of the River Main, a secondary stream channel in an anastomosing river system where different channels are separated due to the local bedrock topography or if the channel was only flooded during flood events. In front of the Roman fort at Großkrotzenburg, the possible Roman channel is bound to emerging bedrock units with bedrock surfaces at 98·90 m NN (GRO 10A) in the north and at 97·82 m NN (GRO 1A) in the south. Further south, the emerging bedrock separates the channel from the recent riverbed forming the base of the southern riverbank at vibracoring site GRO 1A (Fig. 3.9). Riverbanks are characterized by decreased flow velocity and decreasing transport capacity in contrast to riverbeds (Reineck & Singh 1980). Moreover, sediments at site GRO 1A indicate temporary subaerial exposure caused by a fluctuating water level. The difference in the palaeotopography may explain the stratigraphic differences with dominating medium sand for basal unit II and higher a* values for units II and III in vibracore GRO 1A. The central and eastern floodplain area where flood deposits were preserved, silted up during the flood event between 1435 and 1484 cal AD by the vertical accretion of slack water deposits. For the western- most part of the study site, we found a different geochronostratigraphic pattern documenting that the channel was active at least during high- energy flow dynamics until early

modern times. However, the flood sequence of the late 15th century is completely missing in the sedimentary record of the western floodplain. Evidence for another flood event are recorded in the sedimentary sequence at vibracoring site GRO 3. Here, unit II deposits are embedded in fine-grained sediments with a basal unconformity; the time period 1513-1634 AD represents a *terminus ad* or *post quem* for the flood event (Figs. 3.5 and 3.10). The median value of 1564 cal AD suggests a relation with the historical hundredyear flood of the River Main in 1573 AD (Gerlach 1995, Glaser 2013). Finally, a thick layer of fluvial sediments (unit III) encountered at vibracoring sites GRO 3 and GRO 4 was dated to 1646-1792 cal AD and 1661-1950 cal AD, respectively. Assuming natural sedimentation processes, these results reflect rapid accumulation of sediments and silting up of the channel in late Medieval and modern times at the latest (Fig. 3.10). Regarding the median values of radiocarbon ages depicted in Fig. 3.11, flood signals found for the time between 1646 and 1792 cal AD (Fig. 3.11, shaded in dark grey) are well consistent with periods of in- creased flood activity reported by Glaser (2013) for the period of 1640-1700 AD and 1730-1790 AD. Median values of 1769 cal AD and 1777 cal AD obtained for samples retrieved from sediment core GRO 4 indicate that flooding was associated with the 1784 AD event. Glaser & Hagedorn (1990) describe this flood event of the River Main as one of the greatest natural disasters in history showing an exceptionally increased water level. Historical sources also report that widespread sand sheets had been deposited by this event, an observation consistent with our findings in the Großkrotzenburg alluvial plain. However, we consider the upper parts of the natural stratigraphies at vibracoring sites GRO 3 and GRO 4 severely changed by dredging activities in the late 19th century (Stade 1933, chapter 3.5.3). Therefore, the periods of 1646-1792 (GRO 3) and 1661-1950 (GRO 4) most probably do reflect dredging-related reworking of older organic material. This, however, leaves the general age of the younger flood event deposits encountered at the study site untouched.

To sum up, we present sedimentary and geomorphological evidence of repeated flood impact by the River Main on the Großkrotzenburg floodplain. The natural floodplain development has been mainly controlled by major flood events. However, it is striking that the stratigraphies recovered do not give any evidence of the Magdalena flood in 1342 AD that is described as the largest flood of the River Main ever recorded during history (Herget et al. 2015, Herget & Zbinden 2017). Therefore, we suggest that flood events that occurred during late Medieval and modern times caused intensive erosion of the fluvial sediments and erased flood sequences of the early and high Medieval period.

3.5.2 Age evaluation of coarse channel sediments found in front of the Roman castle

At vibracoring site GRO 4, a wood remain embedded in the basal coarse sand and gravel (unit II) was dated to 45 cal BC - 15 cal AD. Overlaying unit III sediments revealed a radiocarbon age of 1661-1800 cal AD resulting in a hiatus of around 1800 years. These findings allows two possible explanations for the real age of the channel sediments: (i) The age of the dated wood in the basal coarse sediments is consistent with the time when the channel was active (*terminus ad quem*) and thus suggests the existence of a channel right in front of the fort when this was used by the Romans. This would result in a hiatus of around 1800 years in the sedimentary archive. However, it is impossible that the young unit III siltation facies directly

follows Roman channel deposits without showing an own basal bedload transport facies. (ii) Unit II sediments might represent the bedload of a flood sequence that was deposited by the same flood event as unit III sediments, namely around 1661-1800 cal AD (chapter 3.5.1). This would correspond to a classical structure of fluvial channel fills with a fining upward trend of grain size towards the top due to decreasing flow velocities (Reineck & Singh 1980, Gerlach & Meurers-Balke 2014a). The wood remain of Roman age would then have to be considered to reflect reworking effects and would simply represent a *terminus post quem* (maximum age) for the deposition of unit II channel material.

However, both the archaeological situation and the human impact on the natural sedimentation must be taken into account regarding sites GRO 3 and GRO 4. Both vibracoring sites are located in the direct prolongation of the Roman bridge of Großkrotzenburg (Steidl 2008). The first Roman bridge pier was discovered 16 m north of the southern riverbank in 1885 during dredging activities within the framework of river regulation measures (Stade 1933). Four additional bridge piers were found towards the northeast resulting in a distance of 20 m between each pier (Stade 1933). At vibracoring site GRO 3, located 40 m to the northeast of bridge pier V, we found angular, red sandstone fragments at the base of the core without any indication that the material was transported and abraded by the river (chapter 3.4.1; Fig. 3.5). These fragments are covered by coarse sand and gravel that show identical sedimentary characteristics compared to the channel sediments encountered at vibracoring site GRO 4. Additionally, channel river deposits (GRO 4) and sandstone fragments (GRO 3) are located at the same depth. According to the DP EC log GRO DP EC 5 (Fig. 3.10), the sand and gravel layer following the red sandstone fragments is almost 1 m thick. Red sandstone fragments of the same type were found as parts of bridge pier III and built-in components of the fortification wall of the Roman fort at Großkrotzenburg (Steidl 2008). Based on this, we prefer considering these artefacts as more or less in situ instead of ascribing them to the phenomenon of being relocated and embedded in younger fluvial material (Brown 1997). In contrast, we suggest that another bridge pier existed at vibracoring site GRO 3 in a distance of c. 40 m to pier V. Consequently, to ensure the equidistance of 20 m between bridge piers, another bridge pier VI must be assumed right underneath the present northern riverbank (Fig. 3.2). Accordingly, we consider it likely that the River Main flowed right in front of the Roman fort during Roman times. Since bridge pier I was found 16 m to the north of the southern riverbank, indicating that this waterside seems to have remained constant over time, the riverbed must have been wider during Roman times compared to the modern riverbed. The possible Roman channel structure was detected at a maximum distance of 75 m to the present riverbank at site GRO DP EC 11. As the sedimentary sequence at vibracoring site GRO 4 with the possible Roman channel fill shows a large hiatus, we suggest that Roman river sediments were originally thicker; they seem to have been partly (GRO 3, GRO 4) and completely (GRO 1A, 6A) eroded during younger periods.

Following this argumentation, narrowing of the river channel since Roman times was mainly triggered by high sediment accumulation during flood events in late Medieval and early modern times. Repeated intersections in the form of unit II layers, erosional unconformities and hiatuses characterize the complex stratigraphic record of the silting up sequence at

the Großkrotzenburg floodplain. Therefore, it is difficult to find clear evidence for vertical dynamics of the river channel. However, at all investigated sites, basal unit II sediments cover the Pliocene bedrock at around the same level (Fig. 3.10). We assume short-term high flow velocities for the northern channel at least until the 18th century. During flood events, the river repeatedly went overbank, traversed the northern channel structure, and caused erosion as long as high-water levels existed. Subsequently, with decreasing flow velocities, sediment accumulation started and silting up of the channel reached up to c. 101 m NN. This caused an overall rise of the riverbed during Medieval (GRO 1A, GRO 6A) and modern times (GRO 3, GRO 4). Beside historical flood events that affect the entire floodplain, intensive anthropogenic impact on the stratigraphy must be assumed for vibracoring sites GRO 3 and GRO 4 in relation with river regulation measures since the late 19th century (Stade 1933, chapter 3.5.1). Also, a modern sewage drain (Figs. 3.2 and 3.10) traverses the western floodplain in the immediate vicinity of vibracoring site GRO 4. The construction of this sewage drain severely disturbed the natural sedimentary sequence. Therefore, considering all these arguments, sediments of unit III encountered directly on top of high-energy channel deposits (unit II) at vibracoring site GRO 4 as well as the upper part of core GRO 3 must be considered as influenced by subrecent dredging activities and may contain reworked material. In terms of age determination of the river channel bed encountered at site GRO 4, these arguments speak for the scenario of an active river channel that existed in front of the fort when it was used by the Romans.

3.5.3 Potential Roman harbour settings

One major objective of our study was to search for fluvial settings that might have hosted harbour facilities during Roman times. Our studies did provide neither archaeological nor sedimentary evidence for harbour installations as such, for example fine-grained sediments of a sheltered harbour basin associated with artefacts typical of harbour use. However, our data indicate that the Roman fort was situated on the edge of a prominent undercut slope that probably already existed during Roman times and that a large River Main channel was probably passing by in the immediate front of the fort and the via principalis.

Hydrological conditions at the undercut slope of a river offer some advantages with regard to the use as a landing site or the installation of a quay. First, the undercut slope offers the deepest part of the riverbed and therefore provides a water level that ensures the navigability of the river also during periods of low water discharge. Second, in contrast to the slip-off slope, the undercut slope is characterized by maximum flow velocities that help to prevent the harbour from being silted up within a short period of time. Moreover, high kinetic energy turned out to be helpful for driving and maneuvering heavily loaded ships (Gerlach & Meurers-Balke 2014b, Roggenkamp & Herget 2014, Wawrzinek 2014). At the same time, constructing a harbour at the outer bank of an undercut slope provokes the risk of erosion and damage. For stabilization reasons, moorings are therefore regarded as essential features of such a harbour situation (Wawrzinek 2014). Roman harbour installation in outer riverbank positions along undercut slopes have been reported from the Lower Rhine region, for example from Xanten, Krefeld- Gelep and Moers-Asberg (Gerlach & Meurers-Balke 2014a). However, Roggenkamp (2016) point out that most of the Roman harbours along the River Rhine did not have any harbour installations. The author mentions that Roman cargo

vessels were characterized by a flat bottom that allowed landing at the riverbank without any need of a quay wall (Roggenkamp 2016). The same may have been the case for the River Main and the harbour situation at Großkrotzenburg.

In addition to the advantages of such harbour situations mentioned above, the installation of a harbour site at an undercut slope of the River Main at Großkrotzenburg was favorable because of logistic reasons; this harbour position ensured the shortest transport route of heavy bricks from the brickyard to the riverbank near the fort at Großkrotzenburg.

Gerlach & Meurers-Balke (2014b) further hypothesize that, during Roman times, riverbeds were wider than today and rivers may have partly worked more as anastomosing river systems than as mere meandering streams. These authors suggest that permanent navigability was ensured only close to the undercut slope of the main stream. Hydrological conditions for the River Rhine during Roman times were studied by Roggenkamp & Herget (2014) who found that navigability of the river channel requires a minimum water depth of 0.51 m. Comparable studies do not exist for the Roman River Main. The River Main obtained its present fairway depth of 2.90 m between Kostheim and Lengfurt and 2.50 m between the entry in the River Rhine and Kostheim by river regulation measures since the late 19th century (WSV 2015). Until then, water depths lay between 0.60 m (Würzburg) and 0.90 m (entry in River Rhine) (Noll 1866, Schüssler 2004).

The two Roman sewage drains found at Großkrotzenburg are both orientated orthogonal to the River Main (Becker 2014). The mean water level of the River Main during Roman times must have been below the mouth of these sewage drains, otherwise the fort would have become flooded by backwater (cf. Roggenkamp 2016). The bottom of the western sewage drain was reconstructed by Becker (2014) to 107.89 m NN. Roggenkamp (2016) shows that the distance between Roman sewage drains and the mean water level may differ from site to site and thus sewage drains only allow the reconstruction of the maximum mean water level. At Großkrotzenburg, there are no further archaeological findings that may be used to reconstruct the mean water level of the River Main. For this reason, estimating river channel incision since Roman times is not possible.

Remains of Roman bridge piers can be also a useful indicator to estimate the past hydrological conditions of a river (Roggenkamp 2016). Unfortunately, none of the five bridge piers near Großkrotzenburg are preserved until the present day, all the structures being removed during river regulation measures, and data concerning the altitude of the bridge pier foundation is not available (Stade 1933). The minimum water level can thus simply be estimated to be at 99.02 m NN (unit II sediments at site GRO 4) and the maximum water table as below 107.89 m NN (Roman sewage drain). However, a final estimation of the water depth of the Roman River channel and a following assessment of the navigability are not feasible based on our data. Nevertheless, our results indicate that the River Main flowed right in front of the fort during Roman times (chapter 3.5.1 and 3.5.2). The potential harbour site could be easily reached by the via principalis that passes the southern gate of the Roman fort. If any harbour installation existed, they, however, were most probably eroded by the River Main since Roman times.

3.6 Conclusions

The floodplain at Großkrotzenburg was investigated using geomorphological, geoarchaeological, sedimentological, geophysical and geochemical methods in order to reconstruct the palaeogeographical evolution of the fluvial landscape in the immediate environs of the Roman fort. Geophysical and sedimentological results indicate that, during Roman times, the active river channel was probably located directly in front of the Roman fort. This channel revealed features typical of an undercut slope offering hydrological conditions favorable for a river harbour. Geomorphological investigations further suggest that the riverbed was wider during Roman times. Findings of bridge piers document the overall water course of the River Main during Roman times. However, our data indicate that the northern riverbank has shifted towards the south since then. In contrast, the southern waterside seems to have remained constant over time. Additionally, we found evidence for another bridge pier candidate located 40 m northwards of bridge pier V. However, neither archaeological nor sedimentary evidence associated with typical harbour installations were detected. Nevertheless, we assume that a harbour situation was existing right in front of the fort and would have been easily reachable by the via principalis. Fluvial sediment archives near Großkrotzenburg turned out to be fragmentary as documented by hiatuses spanning up to 1800 years. This is due to major erosional processes related to few high-energy flood events as well as due to intense anthopogenic impacts during river regulation measures at least since the late 19th century and the construction of a modern sewage drain.

We were able to detect two periods of major flooding, namely between 1435 and 1484 cal AD and between 1646 and 1792 cal AD. These periods are consistent with periods of increased flood activity in Central Europe derived from historical sources, namely between 1430-1460 AD and between 1730–1790 AD. Focusing median values of presented geochronological data, we suggest that these two periods most probably correspond to the hundred year floods in 1480 AD and 1784 AD, respectively. A third major flood event recorded in the Großkrotzenburg fluvial archive revealed a maximum age of 1513-1634 cal AD and is probably related to the hundred year flood event that occurred in 1573 AD. Our results indicate that a few historical flood events controlled the overall development of the fluvial landscape at Großkrotzenburg at least since Roman times and until the late 19th century AD, namely by eroding pre-existing fluvial deposits, accumulating thick sequences of event deposits and narrowing the riverbed. Since the 19th century AD, the architecture and the overall hydraulic conditions of the River Main are controlled by modern river regulation measures.

4 Tracing tsunami signatures of the AD 551 and AD 1303 tsunamis at the Gulf of Kyparissia (Peloponnese, Greece) using direct push *in situ* sensing techniques combined with geophysical studies[3]

Abstract. The western Peloponnese was repeatedly hit by major tsunami impacts during historical times as reported by historical accounts and recorded in earthquake and tsunami catalogues. Geological signatures of past tsunami impacts have also been found in many coastal geological archives. During the past years, abundant geomorphological and sedimentary evidence of repeated Holocene tsunami landfall was found between Cape Katakolo and the city of Kyparissia. Moreover, neotectonic studies revealed strong crust uplift along regional faults with amounts of uplift between 13 m and 30 m since the mid-Holocene. This study focuses on the potential of direct push *in situ* sensing techniques to detect tsunami sediments along the Gulf of Kyparissia. Direct push measurements were conducted on the landward shores of the Kaiafa Lagoon and the former Mouria Lagoon from which sedimentary and microfaunal evidence for tsunami landfall are already known. Direct push methods helped to decipher *in situ* high-resolution stratigraphic records of allochthonous sand sheets that are used to document different kinds of sedimentological and geomorphological characteristics of high-energy inundation, such as abrupt increases in grain size, integration of muddy rip-up clasts and fining upward sequences which are representative of different tsunami inundation pulses. These investigations were completed by sediment coring as a base for local calibration of geophysical direct push parameters. Surface-based electrical resistivity tomography and seismic data with highly resolved vertical direct push datasets and sediment core data were all coupled in order to improve the quality of the geophysical models. Details of this methodological approach, new in palaeotsunami research, are presented and discussed, especially with respect to the question how the obtained results may help to facilitate tracing tsunami signatures in the sedimentary record and deciphering geomorphological characteristics of past tsunami inundation. Using direct push techniques and based on sedimentary data, sedimentary signatures of two young tsunami impacts that hit the Kaiafa Lagoon were detected. Radiocarbon age control allowed the identification of these tsunami layers as candidates for the AD 551 and AD 1303 earthquake and tsunami events. For these events, there is reliable historical data on major damage on infrastructure in western Greece and on the Peloponnese. At the former Mouria Lagoon, corroborating tsunami traces were found; however, in this case it is difficult to decide whether these signatures were caused by the AD 551 or the AD 1303 event.

4.1 Introduction

Extreme event impacts on Earth surface systems may result in subsequent changes in pre-existing environmental conditions and associated geomorphological processes, leaving distinctive traces in the corresponding sedimentary archives. Such palaeoenvironmental changes can be determined by a variety of different geoscientific approaches. In palaeotsunami

[3]This chapter is based on the paper by Obrocki L., Vött, A., Wilken, D., Fischer, P., Willershäuser T., Koster, B., Lang, F., Papanikolaou, I., Rabbel, W., Reicherter, K. (2018b): Tracing tsunami signatures of the AD 551 and AD 1303 tsunamis at the Gulf of Kyparissia (Peloponnese, Greece) using direct push in situ sensing techniques combined with geophysical studies. – Sedimentology, in press: 1-35.

research, tsunami events are commonly identified based on sediment coring or trenching and subsequent detailed sedimentological, geochemical, geophysical and microfaunal analyses (Dominey-Howes et al. 2000, De Martini et al. 2010, Vött et al. 2011a, Cuven et al. 2013, Ulvrova et al. 2016, Chagué-Goff et al. 2017, Finkler et al., 2018a, 2018b, 2018c, Hoffmann et al. 2018, Werner et al. 2018a, 2018b). In some case studies, non-invasive subsurface geophysical methods such as electrical resistivity tomography (ERT), ground penetrating radar (GPR) and/or seismic reflection studies were used to encompass the lateral variability of tsunami deposits and other tsunami-related phenomena such as basal unconformities and erosional channels (Cita & Rimoldi 1997, Vött et al. 2009a, Koster & Reicherter 2014, Goodmann & Austin 2015, Gouramanis et al. 2015, Costa et al. 2016, Kempf et al. 2017, Wunderlich et al. 2018a). Sounding using direct push (DP) *in situ* techniques can significantly facilitate site characterization and improve the quality and resolution of sediment coring (McCall et al. 2014, Maliva 2016). Beside the fact that DP techniques are much less time-consuming than common sediment drilling, *in situ* measurements also do not entail the risks of sediment compaction or contamination (Hausmann 2013). Direct push measurements record data directly while the DP tools penetrate the subsurface and provide profound stratigraphic information on a centimetrescale (Schulmeister et al. 2003, Dietrich & Leven 2006, Vienken et al. 2012). Because these techniques allow the differentiation of sediment properties such as composition, grain size and material consolidation, they are increasingly being applied in hydrogeological and geotechnical investigations. However, the DP techniques have been used very little in geomorphological studies (Schmelzbach et al. 2011, Fischer et al. 2016a, Wunderlich et al. 2018b). So far, DP measurements have not been used within the framework of palaeotsunami research. For the first time, this study focuses on the systematic use of DP techniques in combination with sediment coring and surface-based geophysical prospection in order to detect tsunami deposits.

The western Peloponnese was repeatedly impacted by tsunamis as reported in historical accounts, including earthquake and tsunami catalogues (Soloviev 1990, Soloviev et al. 2000, Ambraseys & Synolakis 2010, Hadler et al. 2012, Papadopoulos et al. 2014a, 2014b, Hadler et al. 2015, Papadopoulos 2015, Willershäuser et al. 2015b). Two major tsunami events that impacted the eastern Mediterranean are reported to have also affected the western Peloponnese, namely the AD 365 and the AD 1303 events (Guidoboni et al. 1994, Ambraseys 2009). These events struck many coasts in the eastern Mediterranean causing extensive destruction of man-made infrastructure on a supra-regional scale. As for the Peloponnese, sedimentary field evidence of these tsunami impacts exists, underlined by results of numerical modelling (Scheffers et al. 2008, Shaw et al. 2008, Papadopoulos et al. 2014b, Ntageretzis et al. 2015a, 2015b, 2015c, Vött & Kelletat 2015, Vött et al. 2018b). Large tsunami events but with minor damage were also reported for 1630 AD and 1866 AD and affected the coasts of the western Peloponnese (Slejko et al. 2014). However, according to Hadler et al. (2012) it must be assumed that the historical record of tsunami catalogues is incomplete, and it cannot be excluded that a considerably higher number of tsunami events hit this area between 500 BC and 1400 AD.

During recent years, geomorphological and sedimentary evidence of repeated Holocene

tsunami landfall was found along the coasts of the Gulf of Kyparissia (Ionian Sea) between Cape Katakolo in the north and Filiatra in the south (Vött et al. 2011a, 2015, Willershäuser et al. 2012, 2015a, Röbke et al. 2013, Koster et al. 2015) (Fig. 4.1). Historical tsunami landfalls for the area surrounding the Kaiafa Lagoon were documented by Koster et al. (2015) for the period between 540 cal AD and 1274 cal AD. Geo-scientific traces of tsunami landfall along the Gulf of Kyparissia are in good accordance with the results of numerical simulations that were calculated based on different palaeotopographies and using different boundary conditions (Röbke et al. 2012, 2013, 2015, 2016). The high tsunami risk for the western Peloponnese seems to be related to high seismic activity along the Hellenic trench, where the African lithospheric plate is being subducted under the Aegean microplate (Papazachos & Dimitriu 1991, Papanikolaou et al. 2007, Fountoulis & Mariolakos 2008). As a result, strong earthquakes occur frequently and are the most common trigger for tsunamis in the eastern Mediterranean (Soloviev et al. 2000, Röbke et al. 2013, Papoulia et al. 2014). Besides tsunamis caused by local offshore faults or submarine slides, potential impact of teletsunamis have to be considered for the western Peloponnese, such as the AD 365 event triggered by an earthquake that took place offshore western Crete (Papadopoulos et al. 2014a). Moreover, the coastline of the Gulf of Kyparissia is directly exposed to the Hellenic Trench which is located only 70 to 80 km offshore (Papanikolaou et al. 2007), and to the Filiatra and Zakynthos

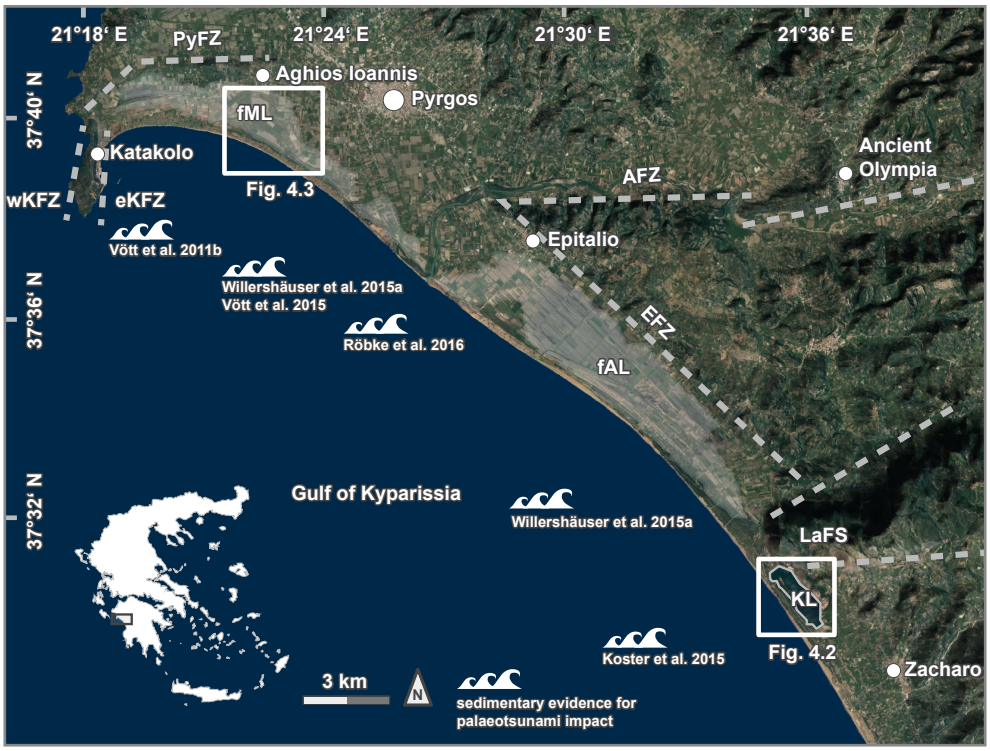

Fig. 4.1: Topographical overview of the northern Gulf of Kyparissia and the western Peloponnese. The western and eastern Katakolo Fault Zone (wKFZ, eKFZ), the Pyrgos Fault Zone (PyFZ), the Epitalio Fault Zone (EFZ), the Alpheios Fault Zone (AFZ) and the Lapithas Fault System (LaFS) border the coastal plain of the Gulf of Kyparissia. Studies were conducted in the former Mouria Lagoon (fML) which has been drained since the 1960s (Pillay 1966) and the Kaiafa Lagoon (KL). Map based on Google Earth aerial image (12/2016).

faults (Tselentis et al. 2010). Moreover, due to its position southward of the protecting Ionian Islands, the gulf is open towards the central Ionian Sea. Additionally, the narrow shelf zones along the western Peloponnese and significant water depths up to 5000 m in the central Ionian Sea increase the tsunami hazard in the Gulf of Kyparissia (McClusky et al. 2000).

Once a tsunami impacts a certain area, it causes abrupt changes in sedimentary and ecological conditions due to sudden high-energy inundation and inland sediment transportation (Peters & Jaffe 2010, Anthony 2014, Röbke & Vött 2017). The impact is of temporary duration but imprints overall landscape evolution in coastal zones and leaves distinct signatures in geological archives. Characteristic features of tsunami traces within an onshore sediment archive may comprise: (i) basal erosional unconformities; (ii) mixed littoral and sublittoral overwash material; (iii) multi-modal grain size distribution; (iv) shell debris layers; (v) fining upward sequences and mud caps; (vi) rip-up clasts; and (vii) thinning and fining of the tsunami layer when moving inland (Dawson & Stewart 2007, Morton et al. 2007, Bahlburg & Spiske 2012, Papadopoulos et al. 2014a, Chagué-Goff et al. 2015, Röbke & Vött 2017). Identifying and investigating tsunami traces is the basis for deciphering the tsunami-related impact on the local landscape evolution and for the evaluation of the overall tsunami hazard. The main objectives of this study were, firstly to identify tsunami deposits by applying a new methodological approach based on selected DP tools combined with sediment coring and surface-based geophysical measurements; and secondly to use DP-derived parameters for stratigraphic interpretations of sedimentary features related to high-energy tsunami inundation. Thirdly, in a more general methodological context, this study evaluates the use of combined ERT and DP prospection techniques in search of appropriate vibracoring sites as a base for collecting relevant sedimentary data.

4.2 Study Areas

The study areas are located along the coast of the Gulf of Kyparissia in the western Peloponnese (Fig. 4.1). They comprise the eastern shore of the Kaiafa Lagoon (Fig. 4.2) to the north-west of the Zacharo village and the former Mouria Lagoon to the south of the village of Aghios Ioannis (Fig. 4.3). The crescent-shaped coastline of the Gulf of Kyparissia is characterized by sandy beaches and a mostly vegetated dune belt consisting of different generations of beach ridges and dunes (Kraft et al. 2005). The dunes separate extensive backbeach swamp and lagoonal environments from the open waters of the Gulf of Kyparissia. The lagoonal system comprises the former Mouria Lagoon to north, and the former Agoulenitsa Lagoon and the Kaiafa Lagoon to the south of the Alpheios River mouth (Fig. 4.1). Nowadays, only the Kaiafa Lagoon still exists as a waterbody, whereas the other two lagoons have been drained since the 1960s (Pillay 1966). The Alpheios River is the largest river of the Peloponnese and forms the main sediment source for sedimentary processes along the shores of the Gulf of Kyparissia (Kraft et al. 2005). The Agoulenitsa coastal plain is bound by a steep north-west/south-east trending fault at its landward side, namely the Epitalio Fault Zone (EPZ) that in the form of a fault scarp – separates the coastal plain from a hilly range out of sandy to silty deposits of the Vounargon Stage of Upper Pliocene (IGME 1982, Papanikolaou et al. 2007). The Kaiafa Lagoon

is also bound by a steep fault zone, namely the southern Lapithas Fault Zone (LaFZ) (Fig. 4.1; Institute for Geology and Mineral Exploration (IGME 1982, Mason et al. 2015). The region has experienced substantial vertical crust movement, especially along these deep fault systems, since Tertiary times (Papanikolaou et al. 2007, Athanassas & Fountoulis 2013). Based on the comparison of relative sea-level indicators, Vött et al. (2015) identified crust uplift of minimum 13 to 20 m along local fault zones (western Katakolo Fault Zone (wKFZ), eastern Katakolo Fault Zone (eKFZ), Pyrgos Fault Zone (PyFZ), Alpheios Fault Zone (AFZ), Epitalio Fault Zone (EFZ)) of the northern Gulf of Kyparissia since the mid- Holocene. These data are in good agreement with results of Papanikolaou et al. (2007), who estimated an overall displacement of 60 m in the north (Katakolo) and 30 m in the south (Filiatra) during the Holocene, based on offshore seismic data. Low-energy environments such as the Kaiafa and former Mouria lagoons show a high preservation potential for tsunami deposits and thus represent excellent archives for tsunami research (Minoura & Nakaya 1991, Switzer & Jones 2008, Vött et al. 2009a, 2009b, Avramidis et al. 2013, Fischer et al. 2016b, Finkler et al. 2018a, 2018b). Due to repeated tsunami landfall, washover fans were formed at both sites (Figs 4.2 and 4.3; Koster et al. 2015, Willershäuser et al. 2015a). However, there are differences between the local settings of the sites, which vary with regard to the palaeoenvironmental and coastal evolution (Kelletat 1974). Major storms are neither recorded in local geological archives nor reported by historical data (see Vött et al. 2018b, 2018c, for further details and discussion).

4.2.1 The Kaiafa Lagoon

The Kaiafa Lagoon has been, unlike the Mouria and Agoulentisa lagoons, only partly drained and shaped by anthropogenic influences since 1970, resulting in a decreased present-day surface extent of 1.5 km^2 (Koster et al. 2015). The lagoon runs parallel to the present coastline and is still connected with the Gulf of Kyparissia by a small channel (Fig. 4.2A). Kraft et al. (2005) suggests that the lagoon was formed by littoral sand transport from the Alpheios River at least since Classical times. Strabo (63 BC to 23 AD) and Pausanias (115 to 180 AD) describe a river called Anigros that fed the Kaiafa Lagoon. This river was supposedly fed by several large springs located at the foot of the Lapithas fault scarp, one which was called the Spring

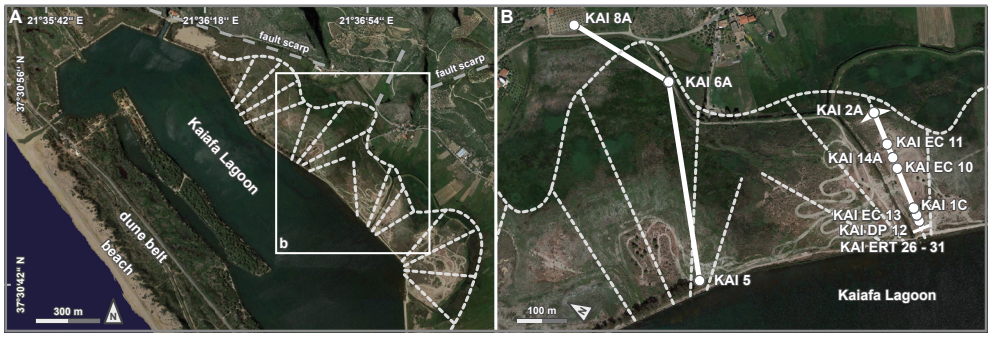

Fig. 4.2: Topographical setting of the study area near the Kaiafa Lagoon. (A) Overview of the geomorphological setting along the eastern shore of the lagoon. White dashed line depicts washover fans. (B) Detailed view with location of vibracoring sites, DP sensing sites and ERT transects presented in this paper. Locations of sensing sites KAI HPT/CPT 1 and KAI HPT/CPT 14 are identical with locations of coring sites KAI 1C and KAI 14A; for further details, see text. Maps based on Google Earth aerial images (5/5/2015).

of Anigrid Nymphs. These thermal springs are still present and are located to the north-east of the lagoon discharging water with high sulphur and mineral concentrations into the Kaiafa Lagoon as well as into the swampy back beach area between the Lapithas Mountains and the dune belt (Katsambas & Antoniou 1996, Kraft et al. 2005). The eastern shore of the Kaiafa Lagoon is characterized by multiple fan-like sand structures (Fig. 4.2). According to Koster et al. (2015), these configurations clearly correspond to wash-over fans that were formed by tsunami impact between 540 cal AD and 1274 cal AD.

4.2.2 The former Mouria Lagoon

The area of the former Mouria Lagoon has been completely drained since the 1960s and transformed into agricultural land (Pillay 1966). The present surface represents the former lake bottom, most parts of its lying below the present sea level. According to Kraft et al. (2005) the lagoon is separated from the sea by a large barrier system. Willershäuser et al. (2015a) presented a vibracoring transect across the former Mouria Lagoon (Fig. 4.3) documenting an intensive change in palaeoenvironment due to Holocene sea level changes and repeated tsunami landfall since the 5th millennium BC. Tsunami deposits attest to high-energy tsunami inundation up to ca 1.9 km inland forming washover fans along the coastal barrier (Willershäuser et al. 2015a).

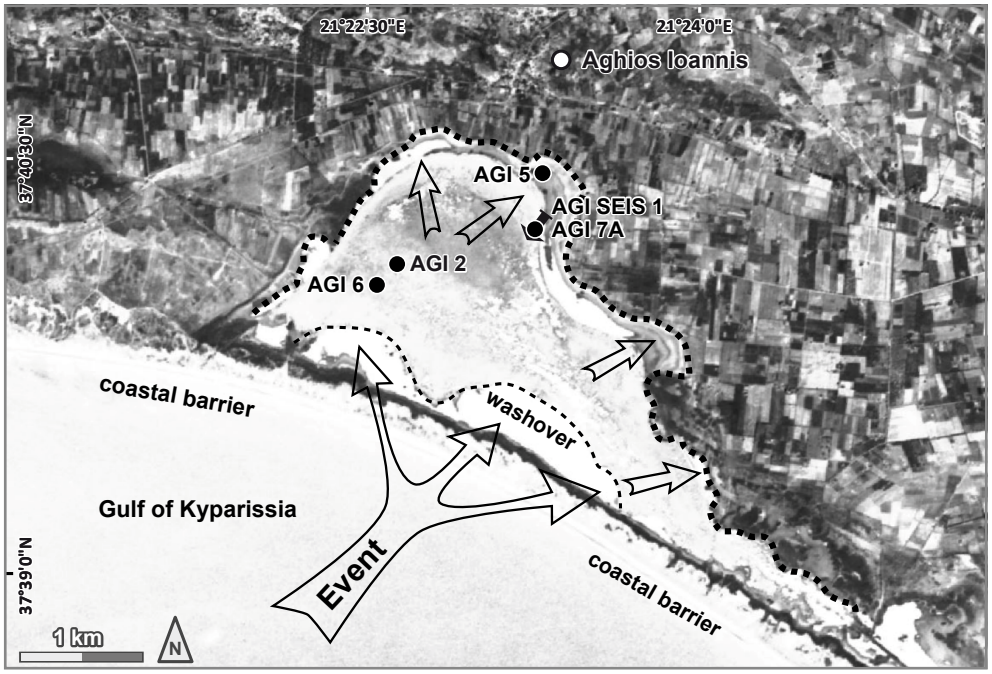

Fig. 4.3: Topographical setting at the former Mouria Lagoon near Aghios Ioannis with location of vibracoring site AGI 7A, DP sounding sites AGI SCPT 7/HPT 7 and seismic transect AGI SEIS 1 presented in this paper. Arrows show direction of tsunami impact. Adapted from Willershäuser et al. (2015a). Map based on Corona satellite image (1970).

4.3 Material and methods

Geomorphological and sedimentological studies were carried out at the Kaiafa Lagoon and the former Mouria Lagoon in order to investigate the local stratigraphic records of tsunami landfalls using both DP techniques and surface-based geophysical methods. Sites were selected because previous investigations revealed sedimentary evidence of tsunami impact based on geophysical and sediment core data (Kaiafa Lagoon: Koster et al. 2015; former Mouria Lagoon: Willershäuser et al. 2015a). DP HPT and DP CPT logging were carried out to test the usability of both methods for the detection of sedimentary features associated with tsunami landfall. The methodological approach were complemented by surface-based and DP *in situ* seismic (DP SCPT) measurements with the aim to improve the geophysical model of non-invasive seismic profiling. The positions and absolute elevations of DP sites, new vibracoring sites, ERT transects and seismic profiles were measured by means of a differential GPS HiPerPRO FC-250 (Topcon, Tokyo, Japan) with a precision ≤2 cm.

4.3.1 Electrical resistivity tomography (ERT) investigations

In the current study, electrical resistivity measurements (ERT) depth sections were used as a base to localize DP and vibracoring sites in order to ensure best possible representativeness with regard to underground architecture. ERT measurements were further conducted along transects on the eastern shore of the Kaiafa Lagoon in order to obtain information on the stratigraphy of a local washover fan structure (ERT transects KAI ERT 26 to 31; Fig. 4.2B). Measurements were carried out using a Syscal R1 Plus Switch 48 multi electrode system (IRIS Instruments, Orléans, France) and a Wenner-Schlumberger electrode array with an electrode spacing of 1 m. ERT data were inverted using the RES2DINV software tool. To ensure the overall comparability of ERT depth sections, data from different transects were displayed using the same legend categories for electrical resistivity, given in ohm.m.

4.3.2 Sedimentologial analysis

Vibracores were drilled at five different sites at the Kaiafa Lagoon (cores KAI 1C, KAI 2A, KAI 6A, KAI 8A and KAI 14A) and at one site at the former Mouria Lagoon (core AGI 7A) using an automotive Nordmeyer RS 0/2 3 drill rig (Nordmeyer, SMAG, Braunschweig, Germany) and 60 mm core diameter for a closed steel auger system with plastic inliners inside to obtain undisturbed sediment cores. Plastic inliners were opened in the laboratory, cleaned, docucmented by photograph and described based on sedimentological and geomorphological criteria (Ad-hoc-AG Boden 2005). Grain size analyses were conducted for 41 samples retrieved from core KAI 1C, for 26 samples from core KAI 2A, for 19 sample from KAI 6A, for 26 samples from KAI 8A, for 31 samples from KAI 14A and for 29 samples from AGI 7A using the Köhn sieving and pipette method (Köhn 1929, Barsch et al. 2000). Prior to grain size analysis of fine-grained material, standard pre-treatment was carried out including dry-sieving in order to determine the amount of coarse material >2 mm, followed by peptization of the <2 mm fraction in sodium pyrophosphate for 12 h. The percentages of eight grain size classes for cores KAI 1C, KAI 14A and AGI 7A were determined (clay: <2 µm; fine silt: 2 to 6.3 µm; medium silt: 6.3 to 20 µm; coarse silt: 20 to 63 µm; finest fine sand: 63 to 125 µm; fine sand: 125 to 200 µm; mediumsand: 200 to 630 µm; coarse sand: 630 to 2000 µm). For each sample,

the (mean) relative frequency distribution curves as well as cumulative frequency curves based on 99-step cosine interpolation functions over the grain size classes were calculated.

Radiocarbon dating using the accelerator mass spectrometry (AMS) technique was conducted for six samples out of plant remains and charcoal retrieved from cores KAI 6A and KAI 8A. Radiocarbon dating was carried out at the Klaus-Tschira-Laboratory, Curt-Engelhorn-Zentrum für Archäaometrie, Mannheim, Germany. Radiocarbon ages of this study and published dates from previous studies were calibrated using the Calib Rev 7.1 calibration software (Reimer et al. 2013).

4.3.3 Direct push *in situ* techniques: Hydraulic profiling tool (DP HPT) and cone penetration testing (DP CPT)

Direct push logging was carried out using a Geoprobe 540 MO system (Geoprobe, Salina, KS, USA) adapted to a Nordmeyer drill rig RS 0/2 3 (Nordmeyer, SMAG, Braunschweig, Germany). Direct push measurements were carried out at 12 sites using different DP probes. Hydraulic profiling (HPT) was performed at sites KAI 1C and KAI 14A at the Kaiafa Lagoon and at site AGI 7A at the Mouria Lagoon using a Geoprobe HPT K8050 (2.25 inch system) probe. During the penetration process, water was injected with a constant flow rate (Q) of 250 ml min^{-1} to the pushhole through a small screen port at the side of the DP HPT probe. The system allows the measurement of the water pressure (P_{inj}) and inline pressure (P_{inline}) in response to the sedimentary conditions in a vertical resolution of 2 cm (McCall 2011). The raw HPT pressure (P_{total}) is the sum of the atmospheric pressure (P_{atm}), hydrostatic pressure (P_{hydro}) and the pressure required to inject the water into the subsurface (P_{inj}) observed at every measurement point. Since P_{hydro} increases below ground water level, P_{inj} must be corrected by performing pressure dissipation tests at different depths below ground water level. These tests allow the evaluation of the local static ground water level, the atmospheric pressure and the hydrostatic pressure for various depths of the dissipation test. Based on these three parameters, the actual P_{inj} is calculated as: $P_{inj} = P_{total} - (P_{hydro} + P_{atm})$ (Körber et al. 2009, McCall et al. 2014, Geoprobe 2015). The estimated hydraulic conductivity ($K_{est.}$) was calculated as:

$$K_{est.} = 21.1 * \ln (Q/P_{inj}) - 41.74$$

after McCall & Christy (2010) using the Direct Image Viewer Software(www.geoprobe.de). Usually, low $K_{est.}$ and high P_{inj} are related to small grain sizes, such as clay and silt, and a lower ability to transmit water. In contrast, high $K_{est.}$ and low P_{inj} indicate larger grain sizes, such as sand or gravel (Geoprobe 2015). The DP HPT probe is also equipped with four electrodes in a linear arrangement using a Wenner array to measure the electrical conductivity (EC; Harrington & Hendry 2006). The DP EC log generally correlates well with DP HPT pressure, if the differences in the chemical composition of pore water are negligible (Geoprobe 2015, Schön 2015). Usually, low EC values are related to coarser sediments, such as sand and gravel. In contrast, high EC values represent fine-grained sediments, such as clay and silt (Wunderlich et al. 2013, Fischer et al. 2016a). Contrary to the DP HPT, DP EC is also dependent on chemical and mineralogical factors and, therefore, DP HPT logs show changes in sedimentary characteristics below the ground water surface more reliablly (Geoprobe 2015). At the Kaiafa lagoon, EC values and HPT parameters showed a very high visual correlation. DP

EC sensing using a SC520 soil probe for DP EC measurements was carried out at 9 additional sites (KAI EC 2, KAI EC 6-13).

Cone penetration tests (CPT) were conducted at the Kaiafa Lagoon (sites KAI 1C, KAI 14A) using a CPT Geotech probe NOVA (Geotech, Askim, Sweden). All DP CPT measurements were controlled and analyzed using the software CPT-Pro 6.00 (www.geosoft.com). While pushing the probe with a constant rate of 2 cm sec^{-1} into the subsurface, the DP CPT records simultaneously the cone resistance at the tip (q_c), the sleeve friction (f_s) and the pore pressure (u_2) just behind the cone with a resolution of 2 cm (Lunne et al. 2002, Robertson 2016). The cone resistance is defined as the total force acting on the tip of the probe divided by the projected area of the cone and is a measure of the shear strength. The sleeve friction describes the total force acting on the sleeve of the rod divided by the total area of sleeve (Lunne et al. 2002). The projected tip area and the sleeve area are 10 cm^2 and 150 cm^2, respectively. Both parameters, q_c and f_s, are affected by ambient pore pressure (u_2) due to the geometry of the cone penetrometer and must be corrected using u_2 (Lunne et al. 2002, Robertson 2009, Hausmann et al. 2016). Corrected cone resistance (q_t) and corrected sleeve (f_t) were used for the calculation of the normalized friction ratio (F_r) (Robertson 2016). Robertson (1990) suggested a classification chart based on normalized q_t (Q_t) and F_r that link the DP CPT measurements to specific soil behaviour types (SBT) based on the *in situ* mechanical behaviour of the sediment. This classification chart was applied for this study as a base to interpret DP CPT data. DP CPT and DP HPT data are dependent on the grain size and usually are in a good agreement with grain size measurements (Hausmann 2013). However, SBT only describe the material behaviour that is strongly influenced by stress, stiffness, microfabric, mineralogy and void ratios and therefore may differ from real grain size distribution (Robertson 2009).

All of the DP HPT and DP CPT data were linearly interpolated on a 1 cm depth scale using the 'linterp' function of the 'astrochron' R package (Anthony 2014, Meyers 2014). Further, the DP and grain size data were used to derive both a linear regression and a multivariate linear regression for the estimation of a calculated total sand content for each DP site.

4.3.4 Combined surface-based seismic reflection and seismic CPT (DP SCPT) measurements

At the north-eastern shore of the former Mouria Lagoon, a seismic reflection profile of 71 m length was performed (transect AGI SEIS 1; Fig. 4.3). This seismic profile was done using 48 horizontal geophones (Sensors 4.5 Hz; ION, Houston, TX, USA) with an equidistance of 1.5 m, orientated perpendicular to the profile and connected to two Geode seismographs (Geometrix, San Jose, CA, USA). Horizontally polarized (shear waves perpendicular to the profile direction) shear waves were excited on the profile at shotpoints every 1.5 m in between the geophones by hitting a sledgehammer horizontally on the side of a steel bar, which was coupled to the ground with spikes. Due to the good data quality of the seismic profile, no common midpoint processing and stacking was required (Sheriff & Geldart 1999), but a simplified reflection seismic processing was done. This included a sorting of seismic traces by selecting two seismic traces of those geophones adjacent to each shotpoint to create a common offset section of 0.75 m trace distance, and 0.75 m offset. Each trace was then

bandpass filtered with a trapezoidal bandpass with corner frequencies 8 Hz, 16 Hz, 150 Hz and 200 Hz, then normalized with their first quantile amplitude, and spreading corrected using a linear time gain function. At the former Mouria Lagoon, additional to DP HPT and DP CPT, seismic CPT (DP SCPT) logging were carried out at site AGI 7A. For DP SCPT measurements, a DP CPT system expanded by a SCPT adapter connected immediately behind the DP CPT probe (www.geotech.eu) was used. The use of DP SCPT provides *in situ* data of compression wave velocities (V_p) and shear wave velocities (V_s) that were used to improve both the identification of sediment characteristics (Lunne et al. 2002, Baginska et al. 2013, Robertson 2016) and the evaluation of surface-based seismic measurements. DP SCPT sounding was performed 46 m distant from the beginning of seismic profile AGI SEIS 1. Shear (SH) waves were excited at the surface with the same seismic source and polarization used for profile AGI SEIS 1 at 0.5 m distance to the borehole. The waves were recorded with a three-component geophone located within the DP SCPT probe. Seismic borehole data was acquired at irregular depths, any time when the q_c-log indicated a rapid change of the sedimentary behaviour, because the seismic measurements need to switch of the drill rig to avoid seismic noise. It is assumed that the seismic velocities do not significantly change in between these measurement depths, which was controlled using the DP CPT-log results. The seismic velocity generally shows sensitivity to temperature and pressure (at which temperature can be neglected in the shallow domain), and the porosity of the subsoil. In unconsolidated sediments, the different grain contact conditions between non-cohesive sands and gravels and cohesive clay and silt need to be considered as well (Schön 2015). The porosity, in turn, depends on grain size, clay and silt content. Generally, an increasing porosity leads to a reduced seismic velocity. With increasing pressure, the seismic velocity increases. This study used the y-component perpendicular to the seismic profile for velocity analysis only, because of the chosen source signal polarization. The seismic trace for each depth (z_i) was normalized by its maximum amplitude, bandpass filtered with a Butterworth filter with corner frequencies 32 Hz, 40 Hz, 240 Hz and 288 Hz, and again normalized. Then the crosscorrelation function of two adjacent traces at depths z_i and z_{i+1} was calculated and the time of its maximum was derived. This time represents the difference in travel time (d_{ti}) between two arrival times for different depths. The velocity between these two traces is calculated with $v_i = (z_{i+1} - z_i)/ d_{ti}$ determined based on the arrival time of the first seismic trace because no accurate phase measurement can be done directly at the surface due to near field effects. In a further step, the shear wave velocity depth function derived from the DP SCPT analysis was used to migrate the seismic data of profile AGI SEIS 1 using Stolt migration with time axis stretching of the common offset gather (e.g. Claerbout 1985).

4.4 Results

4.4.1 Traces of high-energy impact at the Kaiafa Lagoon

4.4.1.1 Lithostratigraphic record and grain size distribution of washover deposits

Vibracoring was conducted along two transects from the eastern shore of the Kaiafa Lagoon across the washover fans towards the foot of the Lapithas Mountains (Fig. 4.2B). The

stratigraphic record of the vibracore transect was categorized in four sedimentary units (I to IV) based on grain size analysis. It is in a good accordance with the results described by Koster et al. (2015) showing basal grey sands, covered by typically lagoonal deposits and peat followed by a sand sheet with features of high-energy transport. The lithostratigraphic structure of vibracores KAI 1C and KAI 14A is depicted in Fig. 4.4. Vibracore KAI 1C (ground surface at 2.05 m above sea level (m a.s.l.); located at 37°30'30.36'' N, 21°36'53.79''E) was drilled 1.20 km inland and in a distance of 50 m from the eastern shore of the Kaiafa Lagoon down to 5 m below surface (b.s.).

Fig. 4.4: Photos of vibracores KAI 1C and KAI 14A drilled on the eastern shore of the Kaiafa Lagoon. Note: unit I – high-energy sand; unit II – moderate to high-energy sandy silt to silty sand; unit III – quiet reach silt and clay, unit IV – mud or peat. Ground surface is to the upper left, and the final coring depth to the lower right in each vibracore photo.

The base of vibracore KAI 1C consists of greyish beige fine sand including a high amount of plant remains that is covered by a thin layer of decalcified clayey silt, black to brownish grey in colour (4.85 to 2.91 m below surface). Subsequently, a thick peat unit occurs (4.85 to 3.44 m below surface) with increasing numbers of undecomposed roots, reed, seaweed and other plant remains when moving upcore. The peat layer indicates semi-terrestrial conditions of a swamp over a specific time period. Following an erosional unconformity, a dark grey, laminated clayey silt characterized by a distinct increase of calcium carbonate (3.44 to 3.23 m below surface) is present, covered by a sequence of brown to light grey clayey silt with intersecting layers of fine-grained to medium-grained sand and abundant plant remains (3.23 to 2.77 m below surface). Another sharp contact marks the transition to a massive sand unit, grey to dark grey in the lower part and brownish grey to brown in the upper part (2.77 to 0.00 m below surface). This sand sheet is dominated by medium grained sand but is continuously laminated and shows several sections of fine-grained sand as well as enrichment of shell debris. At 1.60 m below surface, a compact, beige silty clay deposit is encountered. This sequence is again overlain by sand containing several clay intraclasts mixed with numerous fragments of marine microfauna and macrofauna. Vibracore KAI 14A (ground surface at 1.22 m a.s.l.; 37°30'33.42'' N. 21°36'57.37'' E) was drilled 130 m from vibracore KAI 1C with a maximum depth of 4 m below surface. Lithostratigraphic characteristics of vibracore KAI 14A are similar to those of vibracore KAI 1C. However, the change from the peat layer to the upper clastic unit is a more gradual transition from an organic rich mud to dark grey silty clay with some organic foliations. Furthermore, the upcore sand sheet is almost 1 m thinner compared to vibracore KAI 1C and contains several shell layers. Based on core description and results of grain size analyses, four lithostratigraphic units can be discerned, namely three clastic sedimentary units (unit I to III) and one unit dominated by organic material (unit IV; peat, organic mud; Fig. 4.4). Relative and mean cumulative frequency curves of grain size distribution of vibracores KAI 1C and KAI 14A are illustrated in Fig. 4.5. Unit I shows a clear dominance of well-sorted medium-grained sand covering up to 87% of the <2 mm fraction (Fig. 4.5A and B). Relevant amounts of clay and silt can be only observed for intersecting mud caps and clayey intraclasts that also contain some medium-grained sand (Fig. 4.5A). Further, unit I sediments are characterized by a basal erosional contact and the presence of marine fauna, locally in the form of shell debris. The cumulated grain size data clearly reflect the sharp contact between unit I and II indicating a sudden impact on environmental conditions triggered by high-energy sediment transport (Figs. 4.6 and 4.7). Relative frequency distribution of unit II sediments reveal a multimodal distribution and accentuate the poor sorting especially for vibracore KAI 14A (Fig. 4.5C and D). At vibracoring site KAI 1C, unit II deposits are dominated by coarse silt whereas the relative frequency distribution for KAI 14A clearly indicates a trimodal structure. Two sediment samples document a frequency maximum for coarse silt, whereas the others show a frequency maximum for medium sand. Poor sorting of unit II sediments is further underlined by the stepped increase of the mean cumulative frequency curve, representing the presence of grains larger and smaller than the average (Fig. 4.5C and D). Furthermore, unit II partly shows a clear layering and intersecting layers of organic material and shell debris. In particular, the latter cause an increase of coarser grained material in the grain size dataset.

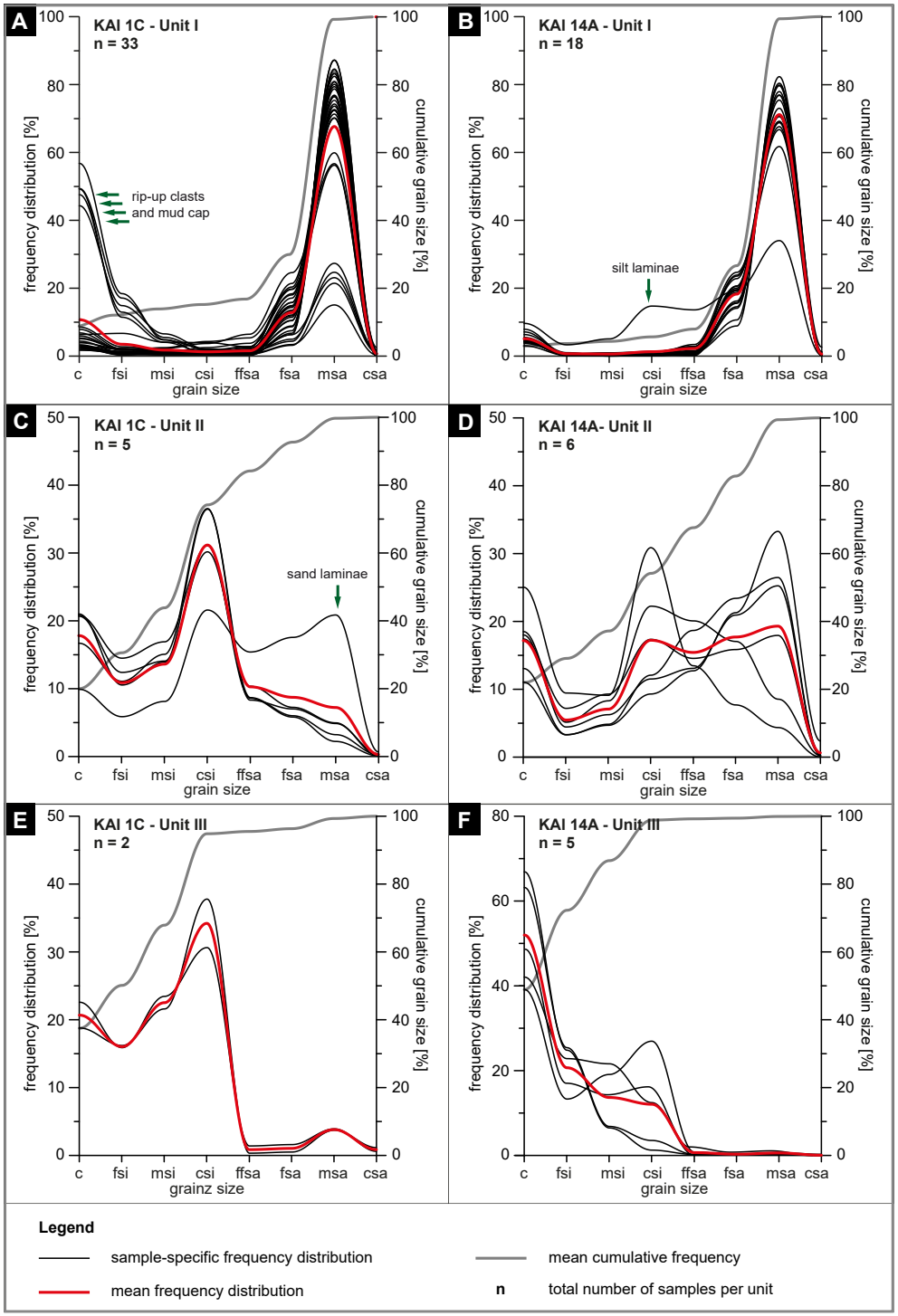

Fig. 4.5: Grain size data obtained for sediment samples from vibracores KAI 1C and KAI 14A showing frequency curves for each sample, classified according to units I, II and III. Curves for the mean distribution frequency and the mean cumulative frequency are given for each sedimentary unit. Note: unit I – high-energy sand; unit II – moderate to high-energy sandy silt to silty sand; unit III – quiet reach silt.

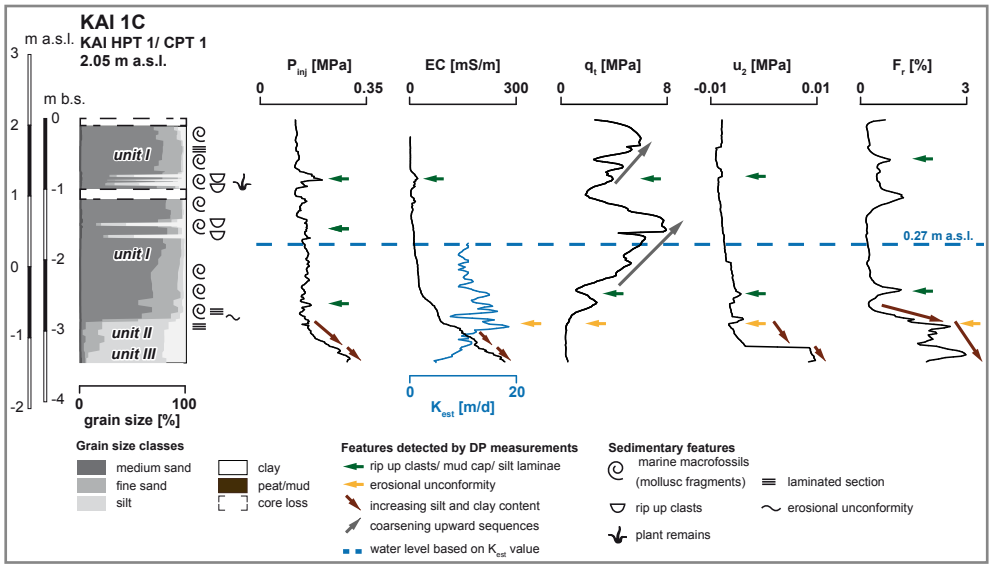

Fig. 4.6: Detailed stratigraphy of the upper section of vibracore KAI 1C compared to cumulative grain size data and results of DP HPT (P_{inj}, EC, $K_{est.}$) and DP CPT measurements (q_t, u_2, F_r). See text for further explanations.

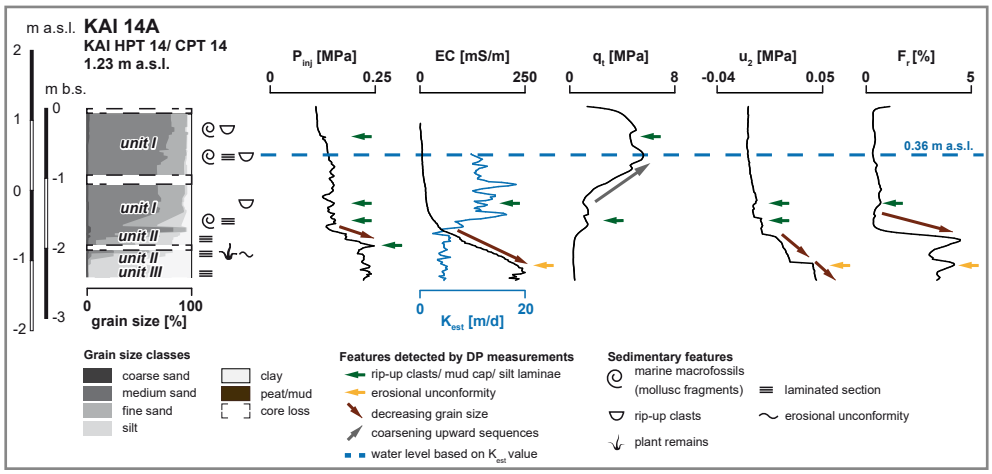

Fig. 4.7: Detailed stratigraphy of the upper section of vibracore KAI 14A compared to cumulative grain size data and results of DP HPT (P_{inj}, EC, $K_{est.}$) and DP CPT measurements (q_t, u_2, F_r). See text for further explanations.

Unit II characteristics attest to energetic conditions significantly higher compared to unit III. Grain size characteristics of unit III show moderate sorting and decreasing grain size from coarse silt dominating at vibracoring site KAI 1C, to clay dominating at vibracoring site KAI 14A (Fig. 4.5E and F). A maximum of 68% of clay was found for a sample retrieved from vibracore KAI 14A. A coarse-grained component, that is absent in the relative frequency distribution at site KAI 14A, appears at site KAI 1C. This seems to reflect decreasing transport energy from site KAI 1C towards site KAI 14A which lies further inland. Cumulated grain size data for the Kaiafa study site are also illustrated in Fig. 4.8 showing a thinning of the uppermost unit I deposits with increasing distance to the coastline.

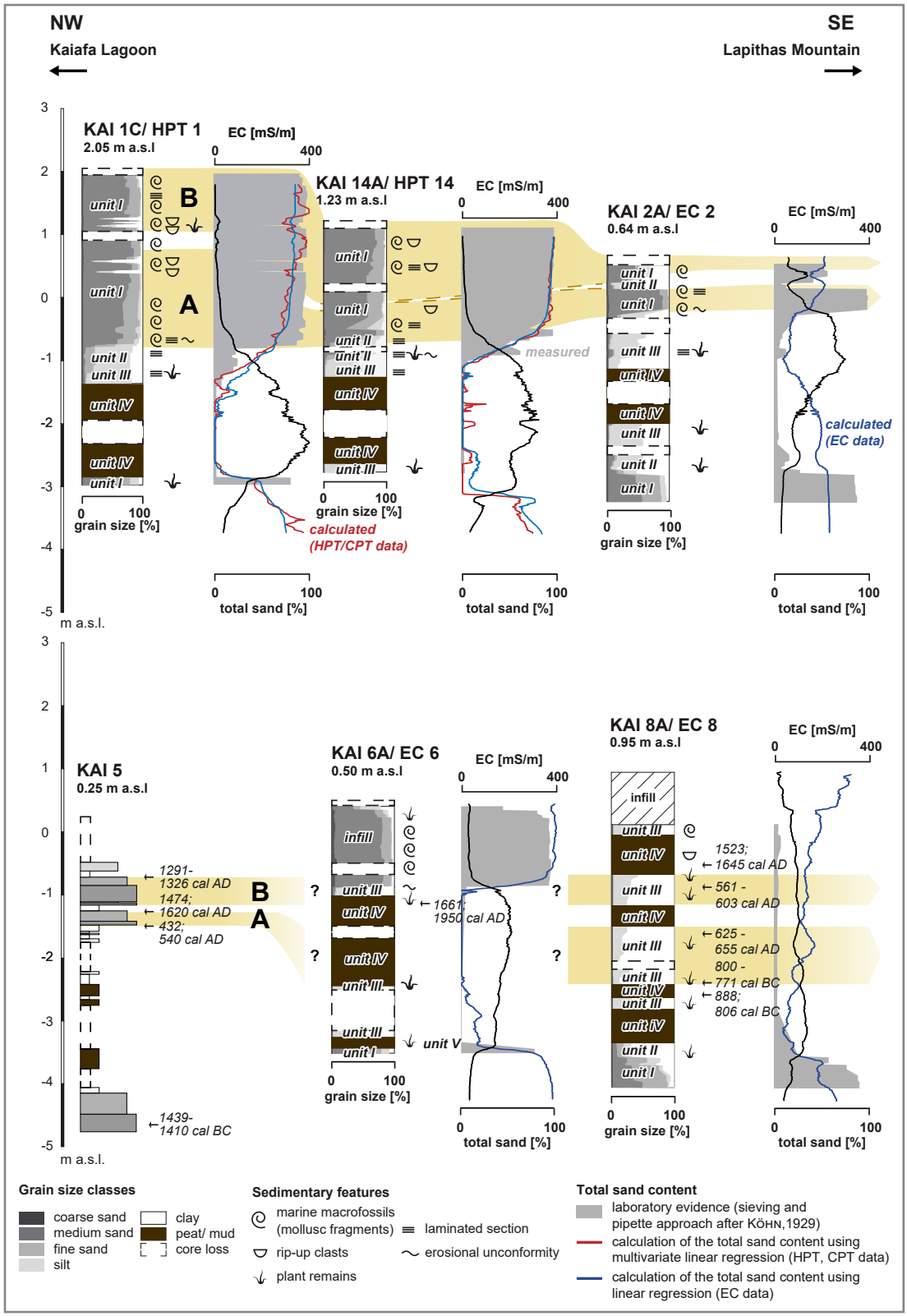

Fig. 4.8: Stratigraphic cross-section across two washover fans at the eastern shore of the Kaiafa Lagoon based on vibracore and grain size data as well as on DP sensing data and modelled grain size data based on DP results. Radiocarbon data are summarized in Table 4.1. See text for further explanation.

Unit I sediments at vibracoring site KAI 1C appear almost 3 m thick and thinning towards inland, namely 0.85 m at vibracoring site KAI 2A, where unit I is interrupted by a 10 cm thick layer of unit II. At the foot of the Lapithas Mountains, unit I sediments are absent in the upper core section (KAI 8A). The lowermost parts of vibracores KAI 1C, KAI 2A, KAI 6A and KAI 8A are characterized by unit I sediments. Repeated environmental changes are documented by the stratigraphic records of vibracores KAI 2A, KAI 6A and KAI 8A showing alternating layers of quiescent water sediments, peat and organic-rich mud.

4.4.1.2 Electrical resistivity tomographies and direct push electrical conductivity data

In this study, six overlapping ERT depth sections are presented running from south-west to north-east across the washover fan at the eastern shore of the Kaiafa Lagoon covering a total length of 256 m. Results of ERT measurements, together with locations of vibracoring sites and results of DP EC sensing are displayed in Fig. 4.9; DP EC values were converted into resistivity values to ensure a better comparability with ERT data. All of the ERT transects revealed a basal zone with low resistivity values (c. 10 to 40 ohm.m) and an upper zone of high electrical resistivity (up to >1200 ohm.m). The transition of these zones is depicted by a distinctly sharp gradient in DP data which is associated with unit I sediments. Additionally, DP data allow the identification of sub-units within unit I obviously due to changes in grain size, mineralogical composition and/or varying water content. Overlapping ERT depth sections clearly depict the landward thinning of the sand sheet. However, ascribing depth boundaries to units I, II and III is not possible based on ERT data alone. Apart from neatly depicting upcore sand deposits, DP logs, with a much higher vertical resolution, show a slight increase for the lowermost parts of depth sections indicating the change to coarser grained material. Further, at vibracoring site KAI 2A, upper unit I is only weakly discernible in ERT because the sand layer is very thin and lies close to ground surface; the uppermost three decimeters of

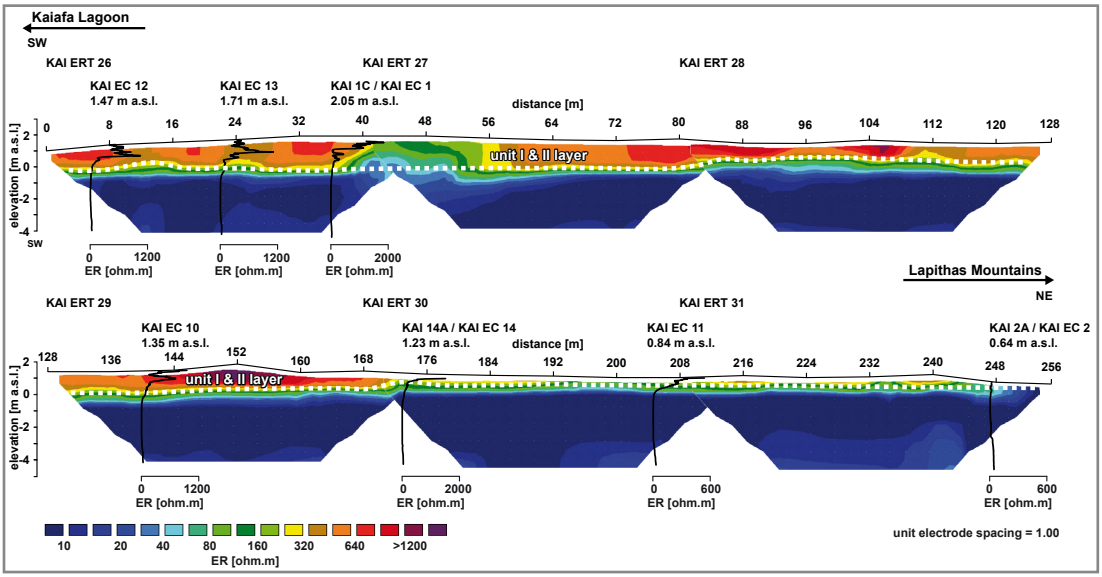

Fig. 4.9: Depth sections of ERT measurements conducted along transects KAI ERT 26-31 together with locations of DP measurements and vibracoring sites. Results clearly document thinning inland of unit I. For transect locations see Fig. 2; for further explanations, see text.

the subground are, however, not depicted in the ERT depth sections due to methodological reasons. Moreover, effects of water content may overlay the sensitivity towards changing grain sizes with increasing target depth and decreasing grain size fraction (unit II to IV).

4.4.1.3 Results of direct push hydraulic profiling and direct push cone penetration test measurements

Hydraulic profiling (DP HPT) and cone penetration test (DP CPT) measurements were carried out at vibracoring sites KAI 1C and KAI 14A. Selected parameters of DP sensing are illustrated in Figs. 4.6 and 4.7, together with cumulated grain size classes for the upper 3.50 m and 2.50 m of cores KAI 1C and KAI 14A, respectively. Grain size data were obtained using sieving and pipette method after KÖHN (1929; chapter 4.3.3). Based on visual comparison, DP HPT and DP CPT data reflect very well the different geophysical characteristics of sediment units found at the Kaiafa study site. This is especially true of the transition from unit I to unit II which is marked by a distinct decrease of $K_{est.}$ and a clear increase of P_{inj}, EC, u_2 and F_r. Also, q_t reaches minimum values for fine-grained sediments caused by decreasing shear strength. Due to the higher water permeability of sand, unit I shows low values for both P_{inj} and u_2. Of course, u_2 is slightly increased in the undrained zone. Furthermore, unit I is characterized by low electrical conductivity values even below the ground water level. Parameter q_t is an indicator of shear strength and maximum values are present for unit I. However, differences in q_t can be observed at both investigated sites. Clayey intraclasts and silty laminae incorporated into unit I appear as distinct peaks in P_{inj}, EC and F_r and as sudden decrease of q_t values especially for site KAI 1C. The sharp erosional contact between unit I and unit II becomes visible by a sudden increase of u_2 increasing fine-grained component of unit II is also shown by a noticeable increase of EC and P_{inj}. However, the P_{inj} curve at site KAI 1C shows a uniform increase and the DP HPT graph for site KAI 14A shows more varying values within unit II. The latter may indicate the poor sorting at this site. Further, grain size data obtained for vibracore KAI 14A show a distinct medium sand peak from 1.68 to 1.76 m below surface that is also recognizable by decreasing $K_{est.}$ values; however, it is rather bound to a shell debris layer than to a sand layer. Maximum pore pressure is associated with unit III due to predominant clay which is also visible in the form of a stepwise increase of u_2. The very low water permeability of unit III is reflected by minimum $K_{est.}$ values. The overall interpretation of DP CPT data based on soil behaviour types (SBT) after ROBERTSON (1990) fits well to the stratigraphic sequences of vibracores KAI 1C and KAI 14A (Figs. 4.10 and 4.11). However, some distinct discrepancies compared to actual core data and results of grain size analyses can be observed. The classification of SBT after ROBERTSON (1990) results in a much more detailed layering of the sequence comprising six SBTs. Unit I deposits are represented by SBT (7) 'gravelly sand to sand', SBT (6) 'clean sand to silty sand' and SBT (5) 'silty sand to sandy silt'. However, grain size data show only small variations of grain size distributions with predominating medium sand (Fig. 4.5). Soil behavior type variations correlate well with the q_t log at both study sites. Maximum q_t values are displayed as SBT (7) whereas minimum q_t peaks within unit I are interpreted as SBT (5). Therefore, SBT classification for unit I reflects varying stiffness and compressibility rather than differences in grain size. The transition from unit I to unit II is marked by SBT (4) 'clayey silt to silty clay' for KAI CPT 1 and KAI CPT 14, 8 cm and 4 cm thick, respectively. Further downcore,

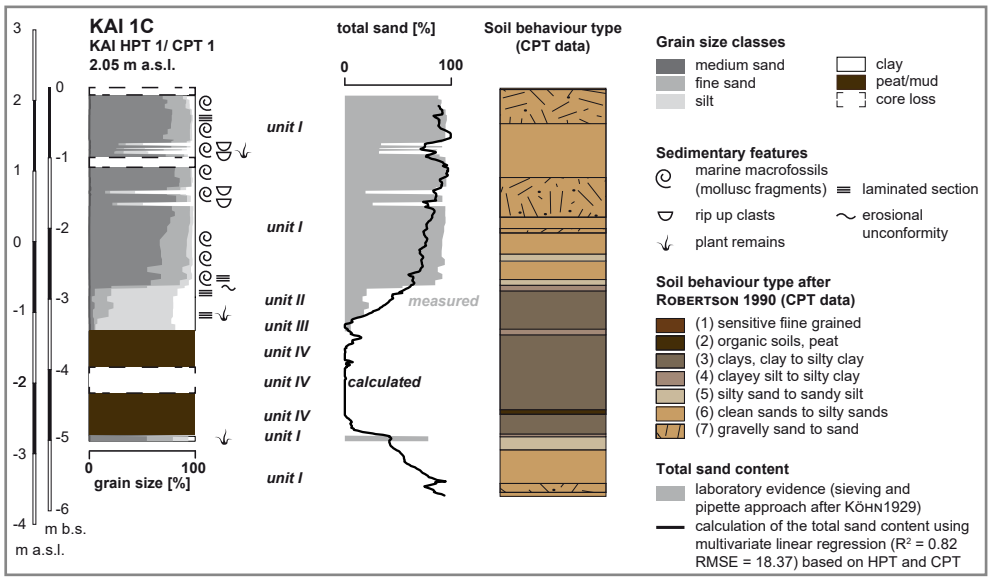

Fig. 4.10: Grain size data (measured after Köhn 1929) obtained for vibracore KAI 1C compared to modelled grain size data based on DP HPT and DP CPT results and classification into soil behaviour types (SBT) based on DP CPT data using the approach after Robertson (1990). See text for further explanations.

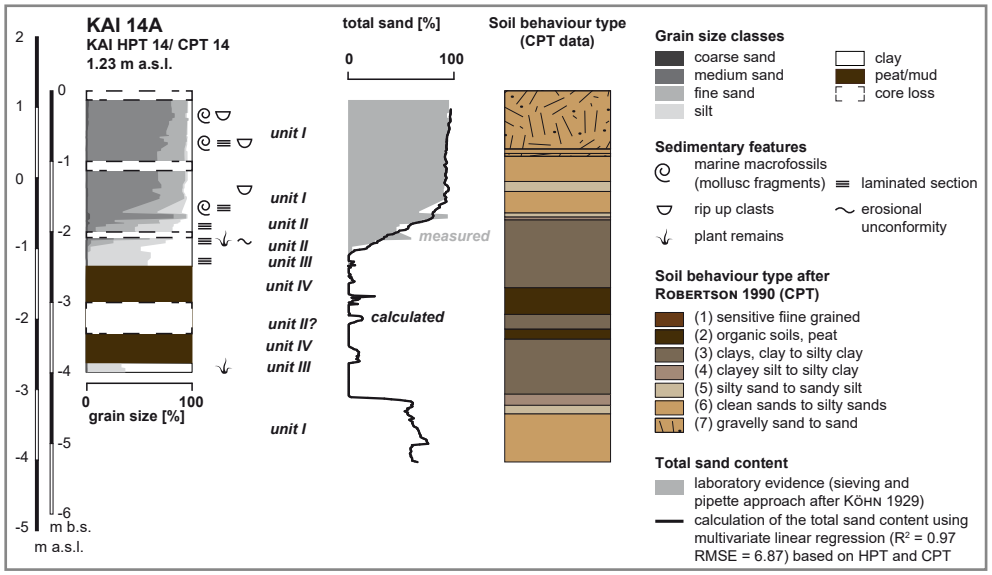

Fig. 4.11: Grain size data (measured after Köhn 1929) obtained for vibracore KAI 14A compared to modelled grain size data based on DP HPT and DP CPT results and classification into soil behaviour types (SBT) based on DP CPT data using the approach after Robertson (1990). See text for further explanations.

unit II and III sediments are classified as SBT (3) 'clays, clay to silty clay' which perfectly describes the actual sediment composition of unit III at vibracoring site KAI 14A based on grain size data. However, SBT classification does not allow the discrimination between units II and III and does not reflect the intersecting sand-rich layers recognized in unit II at both sites by grain size analyses (Fig. 4.5). Unit IV deposits were mainly classified as SBT (3) and only partly as SBT (2) 'organic soil and peat'. This may be due to differences regarding the decomposition of the peat and to intersecting thin layers of clastic sediments. Nevertheless, SBT classification after Robertson (1990) documents well the differences between coarse-grained and fine-grained sediments. To meet the objective of this study to detect high-energy (i.e. predominantly sandy) sediments by means of DP techniques, DP CPT and DP HPT data and Köhn grain size data were used as a base for a multivariate linear regression equation to calculate the total sand content at a specific DP site. Using the principle of parsimony after Sober (1981), Eq. (1) for site KAI 1C 6 and Eq. (2) for site KAI 14A were obtained:

Eq. (1) total sand content (KAI 1C) $= 81.05 + 1.09*q_t + 832.77*f_t - 3.46*F_r - 0.08*EC - 0.03*P_{inj} + 0.26*P_{inline}$

Eq. (2) total sand content (KAI 14A) $= 106.45 - 560.44*u_2 - 1.44*q_t - 0.73*F_r - 0.30*EC - 0.02*P_{inj}$

Eqs. (1) and (2) are based on partly different DP CPT and DP HPT parameters. This is because differences in the site-specific discrimination power of individual parameters were considered. The statistic quality criterion $R^2 = 0.82$ and $R^2 = 0.97$ for Eqs. (1) and (2), meaning that 82% and 97% of the variance are explained by the regression for the total sand content for vibracores KAI 1C and KAI 14A, respectively. The resulting calculated total sand content shows a very good approximation of the true sand content measured by sieving and pipette analyses after Köhn (1929) especially for vibracore KAI 14A with a root mean square error (RMSE) of only 6.88. The RSME represents the sample standard deviation of the differences between measured values and predicted values. The higher RMSE of 18.37 found for sediment core KAI 1C results in a slight underestimation of the sandy component but displays well tendencies of measured grain size variations within unit I. Further, Eqs. (1) and (2) indicate intercalating sand layers within peat unit IV at both vibracoring sites KAI 1C and KAI 14A that are partly strongly correlated with increasing grain size as depicted in the SBT chart (Figs. 4.10 and 4.11). Results show that, once a calibration of DP data with measured grain size data has been achieved, DP CPT and DP HPT techniques can be used within palaeotsunami research to search and identify allochthonous sand layers in their vertical and lateral variabilities in a low cost and highly time-efficient level resulting in high-resolution data of good reliability. Sand contents for all vibracoring and DP sites along the Kaiafa Lagoon transect were further calculated based on a more simple linear regression approach based on DP EC data (Fig. 4.8). Linear regression equations were derived for each DP site using EC as the independent variable (Fig. 4.8; blue curves). Additionally, the results of Eqs. (1) and (2), based on DP CPT and DP HPT data, are depicted for sites KAI 1C and KAI 14A (Fig. 4.8; red curves). It can be discerned from Fig. 4.8 that differences of the sand content within unit I, such as decreasing sand content due to the presence of rip-up clasts (KAI 1C), are not shown by the DP EC-based calculation. Also, intersecting thin sand layers encountered within unit IV at site KAI 14A are not recognized using the EC-based approach. Furthermore, the relation between DP EC data and local sand

content seems to be very site-specific so that no general linear regression equation can be applied for the entire transect. The curves for the calculated sand content at vibracoring sites KAI 2A and KAI 8A show a low R^2 of 0.16 (KAI 2A) and 0.35 (KAI 8A). In contrast, results of the calculated total sand content based on DP EC values for vibracoring sites KAI 1C, KAI 14A and KAI 6A show much better quality criteria with R^2 = 0.79, R^2 = 0.95 and R^2 = 0.83 as well as RMSE = 19.16, RMSE = 8.93 and RMSE = 16.61, respectively. The calculated sand content based on DP EC data can be used as a powerful screening tool in search of tsunami-related sand sheets considering that DP EC measurements can be performed even more quickly and more effectively than DP CPT and/ or DP HPT measurements. In case tsunami sand sheets are detected using the DP EC technique, vibracore evidence is needed to verify a palaeotsunamite candidate and as a base for calibrating high-resolution DP CPT and DP HPT applications.

4.4.1.4 Radiocarbon dating

Results of radiocarbon dating are depicted in Tab. 4.1 together with radiocarbon ages of previous studies.

Sample	Lab. No.	Depth (m b.s)	Depth (m b.s.l)	Sample description	Unit	$\delta^{13}C$ (ppm)	^{14}C Age (BP)	1 σ max; min (cal BC/AD)	2 σ max; min (cal BC/AD)
KAI6A/ 14 PR[1]	33163	1.36-1.37	0.86-0.87	plant remain	III	-25,5	201	modern	younger than 1950
KAI6A/ 14 HR[1]	33154	1.42	0.92	wood remain	III	-27,2	301	modern	younger than 1951
KAI 6A/16+ PR[1]	33165	1,55	1.05	plant remain	IV	-27,1	201 ± 21	1661; 1950 AD	1653; 1950 AD
KAI 8A/ 7 PR[1]	33166	1,48	0,53	plant remain	IV	-27,6	301 ± 23	1523; 1645 AD	1496; 1650 AD
KAI 8A/ 10 HK[1]	33167	1,83	0,88	charcoal	III	-23,9	1486 ± 22	561 - 603 AD	543 - 625 AD
KAI 8A/ 15+ PR[1]	33168	2,57	1,62	plant remain	III	-27,2	1407 ± 23	625 - 655 AD	605 - 660 AD
KAI 8A/ 20+ PR[1]	33169	3.36-3.39	2.41-2.44	plant remain	IV	-27	2574 ± 30	800 - 771 BC	810; 568 AD
KAI 8A/ 21+ PR[1]	33170	3,57	2,62	plant remain	III	-34,9	2684 ± 26	888; 806 BC	895 - 804 AD
-[2]	-	0.95-0.97	0.70-0.68	-	II	-	1068 ± 18	1291 -1326 AD	1274; 1385 AD
-[2]	-	1.51-1.52	1.26-1.27	-	I	-	356 ± 18	1474; 1620 AD	1462; 1631 AD
-[2]	-	1.74-1.77	1.49-1.52	-	II	-	1559 ± 16	432; 540 AD	428; 544 AD
-[2]	-	4.33-4.35	4.08-4.10	-	IV	-	3147 ± 19	1439 -1410 BC	1493; 1325 BC
AGI 2/3+ M[3]	KIA 45967	1.39	3.68	mollusc	I	-3.15	2365 ± 30	87 BC- 14 AD	143 BC - 55 AD
AGI 2/5 M[3]	KIA 45968	1.64	3.93	mollusc	I	-10.19	2560 ± 35	345 - 235 BC	372 - 185 BC
AGI 2/15+ PR[3]	KIA 45969	4.45-4.48	6.74-6.78	plant remain	IV	-23.15	3840 ± 30	2346; 2207 BC	2456; 2202 BC
AGI 5/20+ HK[3]	KIA 45972	4.65.4.70	4.37-4.42	charcoal	III	-11.70	3260 ± 35	1209-1078 BC	1280; 1031 BC
AGI 6/11+ M[3]	KIA 45973	2.82	2.57	mollusc	I	-8.83	2100 ± 25	235 - 329 AD	172 -363 AD
AGI 6/12 PR[3]	KIA 45974	3.35	3.10	plant remain	I	-15.53	2705 ± 25	481- 391 BC	576-388 BC
AGI 6/17 + PR[3]	KIA 45975	5.25-5.26	5.00-5.01	plant remain	IV	-24.14	3785 ± 33	2292; 2144 BC	2336;2058 BC

Tab. 4.1: Radiocarbon dates of samples retrieved from vibracores KAI 6A and KAI 8A (this study[1]) and radiocarbon dates from previous studies by Koster et al. (2015)[2] and Willershäuser et al. (2015a)[3]. Note: m a.s.l. – metres above present mean sea level; 1σ (2σ) max; min cal BP/BC (AD) – calibrated ages, 1σ (2σ)-range; ";" – total interval between minimum and maximum calibrated ages, age model shows multiple intersections with the calibration curve; calibration based on Calib Rev 7.1.0 software (Reimer et al. 2013); Lab. No. – laboratory number (Klaus-Tschira-Labor, Curt-Engelhorn-Zentrum Archäometrie gGmbH, Mannheim, Germany).

Sample KAI 6A/16 + PR was retrieved from the peat section at 1.55 m below surface and yielded a 1σ-calibrated age of 1661 to 1950 cal AD including modern times. Samples KAI 6A/14 PR and KAI 6A/14 HR from the overlying sand unit yielded negative radiocarbon ages, i.e. the material is younger than 1950 AD most probably due to contamination effects with (sub-) recent root material. The uppermost sand layer encountered at site KAI 6A is thus interpreted as an anthropogenic fill leaving the undisturbed quasi-natural subsurface at 1.30 m below surface represented by unit III sediments. Radiocarbon dates are discussed in detail in the local stratigraphic and geographical contexts in the section on event chronostratigraphy (chapter 4.5.2).

4.4.2 Traces of high-energy impact at the former Mouria Lagoon

4.4.2.1 Lithostratigraphic record and grain size distribution of vibracore AGI 7A

Vibracore AGI 7A was drilled at the north-eastern shore of the former Mouria Lagoon (Fig. 4.3), ca**.** 400 m from vibracoring site AGI 5A. The latter was part of a vibracore transect and revealed a thick layer of allochthonous sand which was deposited by tsunami wave impact during the recent past (Willershäuser et al. 2015a). The stratigraphic sequences of the entire vibracore transect were classified using four sedimentary units (Fig. 4.12) as already described for the Kaiafa Lagoon. Vibracore AGI 7A (ground surface at 2.78 m below sea level (m b.s.l.); located at 37°40’17.86’’ N, 21°23’24.53’’ E) was only drilled to a depth of 3 m below surface and focused on the youngest high-energy event layers. The Holocene stratigraphy at site AGI 7A is similar to the one reported for site AGI 5A as both cores were drilled close to the former shore of the Mouria Lagoon. The basal part of vibracore AGI 7A (3.00 to 1.54 m below surface) shows unit III sediments consisting of partly laminated silty clay to clayey silt. The relative frequency distribution curve shows a poor sorting with multi-modal grain size distribution dominated by clay (Fig. 4.13A). Unit III is characterized by a greyish brown to beige colour and shows oxidation features such as Fe and Mn spots. It is intersected by a unit II layer out of beige to grey silty fine sand, 4 cm thick, followed by a clearly laminated sub-section. On top of unit III, greyish beige sandy silt (unit II) was found, including cemented coarse-grained nodules embedded in the sediment matrix (1.54 to 1.45 m below surface). The relative frequency distribution indicates overall moderate to poor sorting of unit II sediment with a dominating silt fraction (Fig. 4.13B). Subsequently, thick unit I medium-grained silty sands mixed with marine shell debris and clayey intraclasts cover the underlying low-energy sediments (1.54 to 0.72 m below surface). The mean relative frequency curve and the mean cumulative frequency curve for unit I document the poor sorting of the sediment (Fig. 4.13C). Cumulated grain size data (Fig. 4.14) document two fining upward sequences within unit I starting with dominating medium-grained sand including a coarse-grained sand component and ending up with sandy silt. From 0.72 to 0.10 m below surface, light beige to brown unit II sediments with several oxidation features were encountered upcore. The uppermost 10 cm of the core are silty fine-grained sand mixed with shell debris.

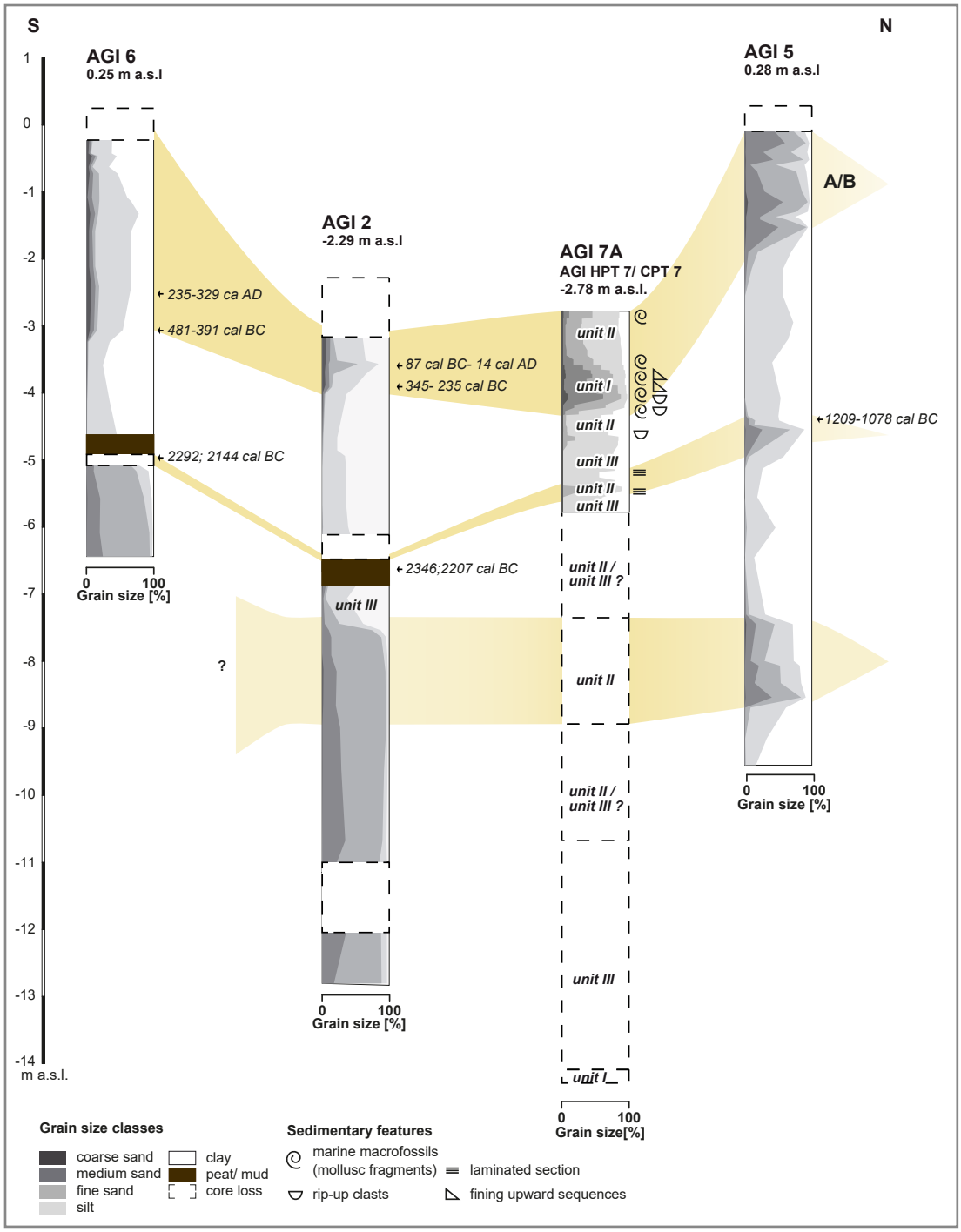

Fig. 4.12: Stratigraphic cross-section across the former Mouria Lagoon based on results by Willershäuser et al. 2015a (AGI 2, AGI, 5, AGI 6) including vibracoring and DP data presented in this study (AGI 7A, AGI SCPT 7, AGI HPT 7). Radiocarbon data are summarized in Table 4.1. See text for further explanation.

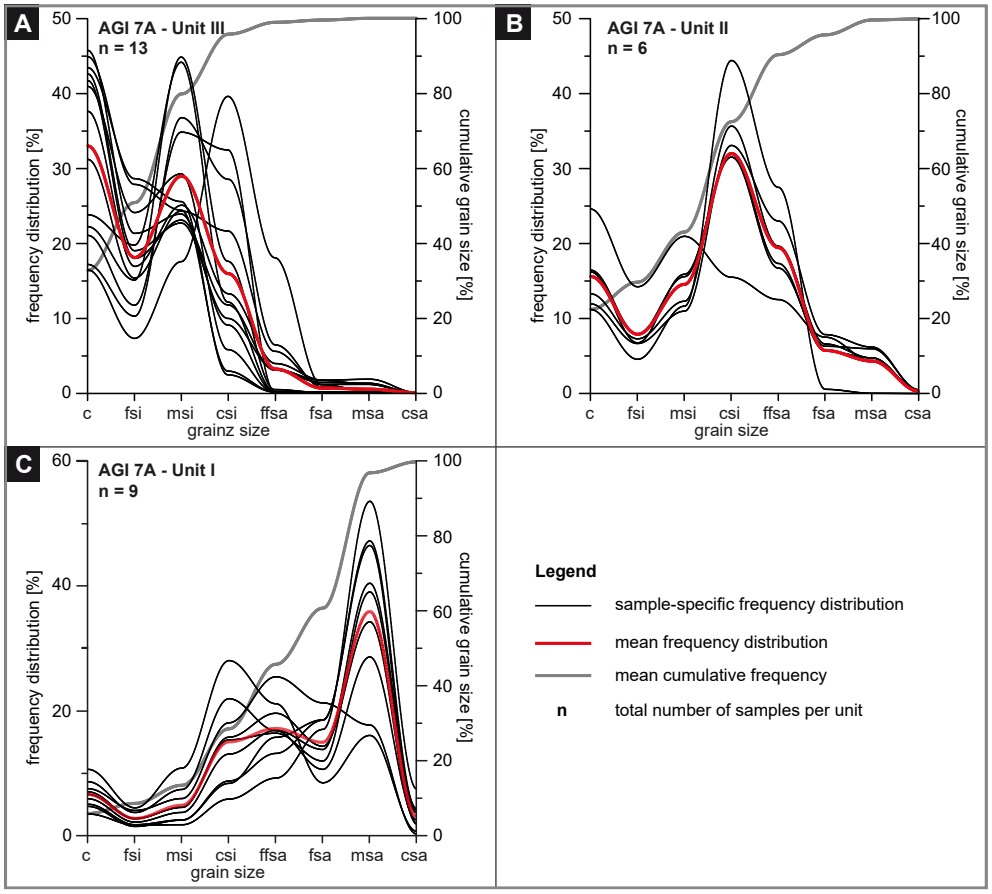

Fig. 4.13: Grain size data obtained for sediment samples from vibracore AGI 7A showing frequency curves for each sample, classified according to units I, II and III. Curves for the mean distribution frequency and the mean cumulative frequency are given for each sedimentary unit.

4.4.2.2 Results of direct push and seismic measurements at vibracoring site AGI 7A

Hydraulic profiling (DP HPT) and seismic cone penetration tests (DP SCPT) *in situ* measurements were carried out at vibracoring site AGI 7A down to 11.50 m below surface to allow a combination with surface-based seismic profiling. Direct push logs AGI HPT 7 and AGI SCPT 7 are depicted in Fig. 4.14 together with cumulated grain size classes for vibracore AGI 7A for the upper 3.00 m based on sieving and pipette data obtained using the KÖHN (1929) method (see chapter 4.3.3). Seismic velocities are depicted as uniform sections between two seismic pulses and associated measurements. Direct push data visually correlates well with grain size data (Fig. 4.14) similar to what is described for the Kaiafa Lagoon. Coarse-grained unit I from 1.54 to 0.72 m below surface is clearly delimited by smallest P_{inj}, EC, F_r and u_2 values and overall increased $K_{est.}$ and q_t values. Further, the q_t log displays the fining upward sequences well, by repeatedly decreasing q_t values with decreasing grain size towards the top (Fig. 4.14). The transition from unit I to unit II at 1.54 m below surface appears with maximum values of q_t and V_s reflecting the cemented section found for vibracore AGI 7A at the same depth. Unit II sediments are characterized by an increase of F_r and a decrease of q_t compared to unit I. However, P_{inj}, EC, $K_{est.}$ and u_2 do not allow a differentiation between unit I and unit II.

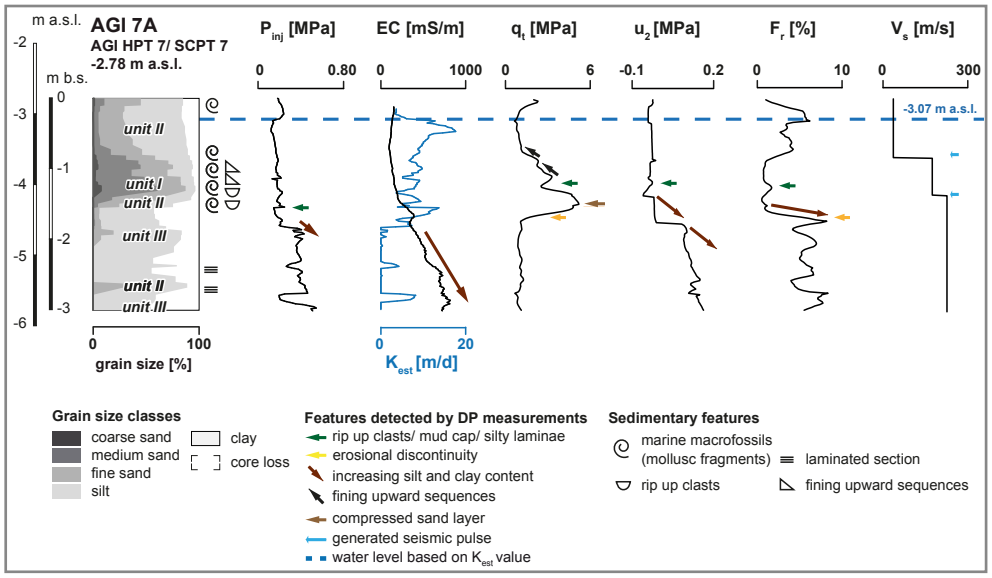

Fig. 4.14: Detailed stratigraphy of the upper section of vibracore AGI 7A compared to cumulative grain size data and results of DP HPT (P_{inj}, EC, $K_{est.}$) and DP SCPT measurements (q_t, u_2, F_r, V_s). See text for further explanations.

The transition from unit II to unit III at 1.54 m blow surface is marked by a sudden increase of F_r and a distinct decrease of q_t, indicating an erosional contact on the top of soft fine-grained sediments. Similar sharp contacts for u_2 and F_r were observed at 2.68 to 262 m below surface for the intersecting unit II layer. DP data show that the upper unit II layer seems to be characterized by a higher plasticity. The transition to predominantly fine-grained material with increasing depth is also marked by decreasing $K_{est.}$ to almost zero. Intersecting coarse-grained layers within unit III sediment were found at 1.99 to 1.63 m below surface, 2.39 to 2.30 m below surface and 2.69 to 2.58 m below surface. All those intercalations are marked by higher $K_{est.}$ and lower P_{inj} and F_r. However, the latter show a slight depth offset between vibracoring and DP data due to coring effects. Fig. 4.15 shows a compilation of selected DP data for AGI SCPT 7 and AGI HPT 7. SBT classification was conducted after Robertson (1990). Soil behaviour type (SBT) data reveal two distinct layers of SBT (7) 'gravelly sand to sand' in topcore position, both followed by SBT (6) 'clean sands to silty sands' reflecting the cyclic fining upward within unit I already described above. Further downcore, SBT classification shows a transition to finer grained SBT (5) 'silty sand to sandy silt' and SBT (4) 'clayey silt to silty clay', corresponding to unit II and unit III sediments, respectively. Furthermore, the varying sand content observed for vibracore AGI 7A is well reflected by SBT classes and corroborates repeated alteration between unit II and unit III. Moreover, irregular q_t, F_r and V_s curve shapes indicate changing grain size compositions from 7.98 to 1.54 m below surface. At 3.57 m below surface there is a transition to SBT (3) 'clay to silty clay' that continues down to 11.29 m below surface, partly intersected by SBT 4 'clayey silt to silty clay'. However, from 6.14 to 4.50 m below surface, the u_2 log slightly decreases to values comparable to those measured for unit II sediments in the upper section. Further evidence for a coarse-grained layer is given by increased V_s and partly increased $K_{est.}$ and decreased F_r values. Homogenous curve shapes document a homogenous grain size composition from 11.29 to 7.98 m below surface.

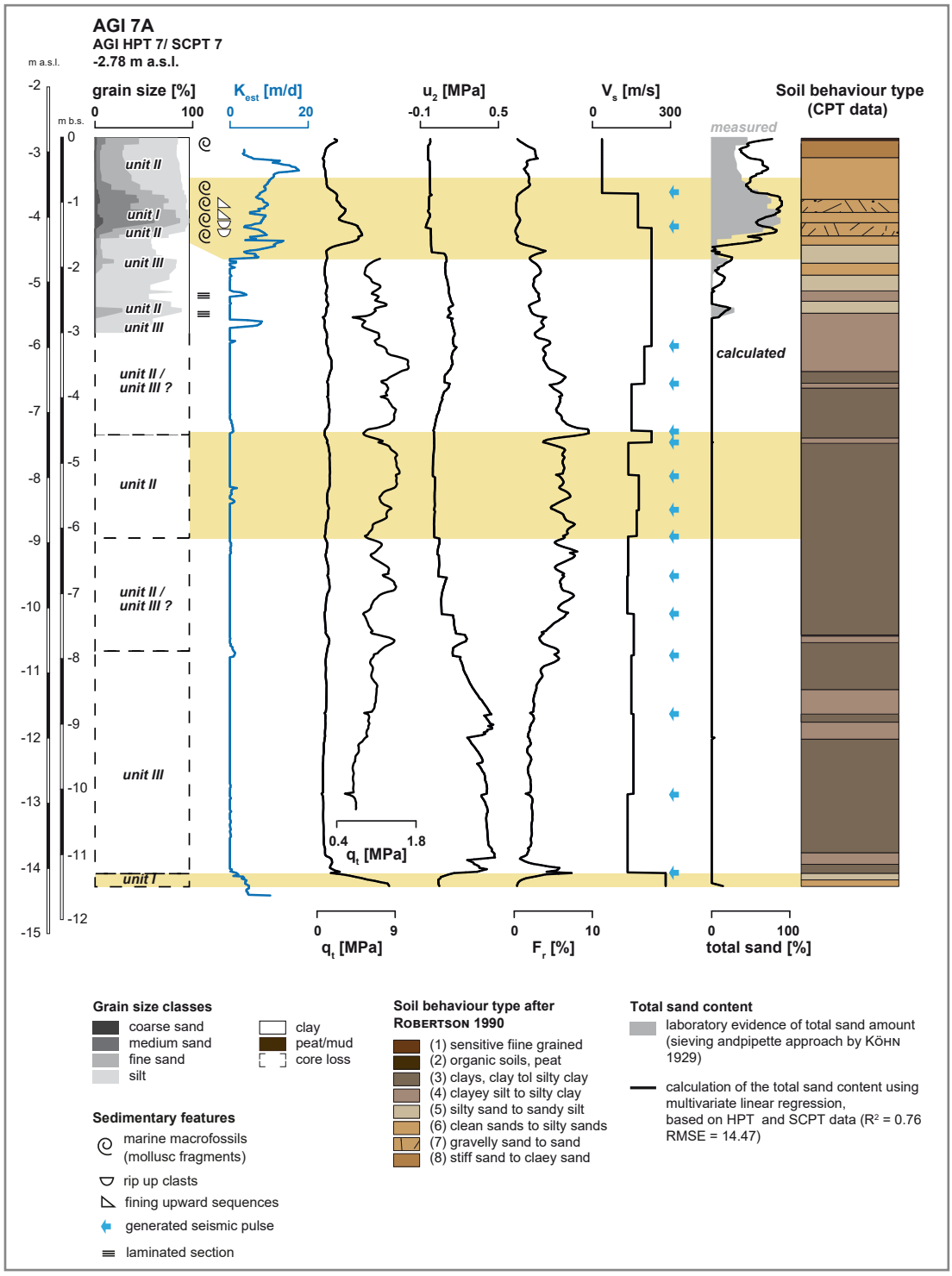

Fig. 4.15: Grain size data (measured after Köhn 1929) obtained for vibracore AGI 7A compared to modelled grain size data based on DP HPT and DP SCPT results and classification into soil behaviour types (SBT) based on CPT data using the approach after Robertson (1990). See text for further explanations.

At 11.29 m below surface, a strong shift and signal is reflected by all parameters and SBT. Further, downward, q_t and V_s reach maximum values and u_2 and F_r minimum values. According to SBT classification, these values correspond to 'clean sands to silty sands' (SBT 6) that document compact basal sands. Based on DP HPT and DP SCPT data and KÖHN (1929) grain size data, the total sand content was calculated using a multivariate regression approach. The resulting multivariate regression equation is:

Eq. (3) total sand content (AGI 7A) = $78.12 - 177.10*u_2 - 1863*f_t - 1.98*F_r + 0.05*V_s - 0.01*P_{inj}$

Quality criteria $R^2 = 0.76$ and RMSE = 14.47 document that the measured total sand content can be reliably estimated using DP HPT and DP SCPT data allowing a thorough discrimination between coarse-grained and fine-grained sections of the Holocene stratigraphic record. However, slight overestimating and underestimating effects regarding the real total sand content can be observed for the upper 3 m. Moreover, at 0.47 m below surface, maximum values for $K_{est.}$ were found and an increased total sand content was calculated using Eq. (3) which is not reflected by grain size data. This seems due to the fact that the corresponding sediment core section was not sampled. Furthermore, three sandy intercalations within unit III between 2.70 m and 1.63 m below surface were calculated and correlate well with $K_{est.}$, P_{inj} and F_r data and SBT classification results. Between 4.78 and 4.60 m below surface, individual DP data only yield a slight increase of sand, whereas V_s data and SBT classification results clearly document an intersecting thin sand layer. At 11.41 m below surface, the transition from SBT (5) to coarser SBT (6) correlates well with an increasing calculated total sand content. To sum up, combined DP HPT and DP CPT data turn out to be a reliable tool to approximate the total sand content in the Aghios Ioannis study site with high precision. Additional seismic velocity data (DP SCPT) further increased the detection quality with respect to allochthonous sand sheets deposited in mud-dominated coastal environments in conjunction with tsunami impacts. The reflection seismic profile conducted across site AGI 7A is depicted in Fig. 4.16.

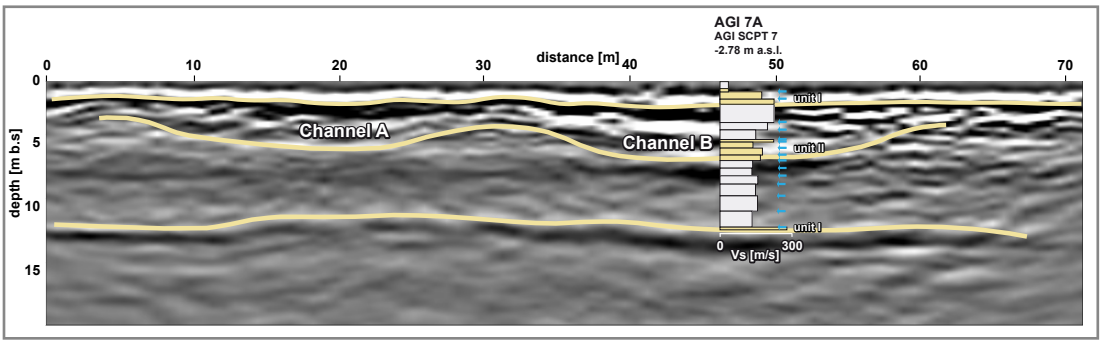

Fig. 4.16: Seismic reflection data migrated with SCPT Vs data showing unit I layers as distinct reflectors as well as two erosional channels. Blue arrows mark depths where seismic pulses were generated. See text for further explanations.

Based on vertical DP SCPT data, reflection seismic data were migrated (see chapter 4.3.2) and depth converted down to 20 m below surface allowing for the correlation of the AGI 7A stratigraphy with surface-based seismic data. The seismogram clearly shows two horizontal reflectors. The first reflector is located near ground surface at c. 1.50 m below surface corresponding to the transition from unit I to unit II. The second seismic anomaly lies between 11 m and 12 m below surface and indicates a distinct change of grain size composition that fits well to the basal unit I found at site AGI 7A. Further, two channel-like structures are illustrated along the seismic profile between distances of 10 to 30 m (channel A) and 40 to 60 m (channel B). At site AGI 7A, the position of the basis of channel B is in a good accordance with the lower end of a section with considerably fluctuating q_t, F_r and V_s values at c. 7.98 m below surface (Fig. 4.15).

4.5 Discussion

4.5.1 Identification of tsunami traces using direct push *in situ* sensing techniques coupled with surface-based geophysical data

The potential of direct push (DP) sensing to identify tsunami sediments was tested at two lagoonal sites along the Gulf of Kyparissia for which sedimentary, geochemical and macrofaunal evidence for tsunami impact as well as results of numerical simulation of tsunami inundation were presented by previous studies (Röbke et al. 2012, 2013, 2015, 2016, Koster et al. 2015, Willershäuser et al. 2015a). This study complemented DP data with sediment coring for a local calibration with regard to sediment behaviour and geophysical characteristics of different grain size units. Altogether, four grain size units were classified based on laboratory data (see chapter 4.4). Unit I is characterized by dominant medium-grained sand and reflects two different types of facies described for the Kaiafa and the former Mouria lagoons, namely tsunami-related event deposits and a basal littoral to shallow marine sand layer. The latter contains palaeo-beach deposits near the Kaiafa Lagoon (Koster et al. 2015) and shallow marine deposits in the area of the former Mouria Lagoon (Willershäuser et al. 2015a). The tsunami- related unit I shows a very good grade of sorting at the Kaiafa Lagoon (KAI 1C and KAI 14A), whereas a clear silt and fine sand component was additionally found at the former Mouria Lagoon.

According to Lunne et al. (2002) sandy materials show relatively low F_r and increasing q_t values of <2% and >8 MPa, respectively. The resulting SBT classification clearly allows the differentiation between coarse-grained and fine-grained sections within the DP CPT log. Therefore, using DP-based SBT classification to identify sandy high-energy layers within a mud-dominated coastal sedimentary sequence seems to be a powerful tool in palaeotsunami research. However, facies with similar grain size distributions overlap on the Robertson (1990) classification chart resulting in the fact that both tsunami sands and basal unit I sands show the same SBT. To overcome this problem, the relative position on the SBT chart must be considered to discriminate between different facies (Amorosi & Milli 2001, Styllas 2014, Missiaen et al. 2015). Unit I deposits of the presented study show F_r values varying from 0.30 to 2.3% and q_t values varying from up to 8 to 14 MPa for tsunami-related sands and the

basal unit I, respectively. Comparable results were found with regards to the seismic studies. Seismic profile AGI SEIS 1 shows a high reflection for both the tsunami-related section and the basal unit I sands. In contrast, DP SCPT measurements reveal maximum V_s values for the basal sands. Therefore, the latter show differing sediment behavior due to compaction effects and increased shear strength which allows to clearly differentiate between these two facies within sediment unit I.

Also in view of the identification of individual tsunami-specific sedimentary features, DP *in situ* sensing turned out to be a highly appropriate and powerful instrument. Abrupt changes in sedimentary conditions such as those caused by high-energy events are marked by a sharp contact between unit I and unit II at all DP sites for the parameters q_t, F_r, P_{inj}, K_{est} and EC documenting a sudden environmental impact (McCall 2011, Styllas 2014). Moreover, q_t data collected at site AGI 7A revealed two consecutive fining-upward sequences showing decreasing q_t values towards the top (Fig. 4.14). Amorosi & Marchi (1999) also report the possibility of detecting fining-upward tendencies using DP CPT measurements for transgressive sand sheets and Campo et al. (2017) were able to detect fining-upward sequences within a fluvial record. The two fining-upward sequences presented in this study at site AGI 7A were proved by laboratory evidence using grain size analysis after Köhn (1929) (see chapter 4.3.3) and are typical of successive wave impacts during tsunami inundation (Bondevik et al. 1997, Kortekaas & Dawson 2007, Röbke & Vött 2017). On the contrary, q_t measurements at site KAI 1C at the Kaiafa Lagoon imply two consecutive coarsening-upward tendencies within high-energy unit I by cyclically increasing q_t values towards the top indicating increasing flow velocities during the recorded inundation phases (Fig. 4.17). Coarsening- upward tendencies within a tsunami record are also known as an indicator for high density flow or long duration of tsunami inundation (Costa et al. 2015). Following these analyses, a multiphase tsunami impact associated with the input of extremely large amounts of sediment must be assumed resulting in the deposition of a massive unit I sand layer at site KAI 1C (Fig. 4.17).

Moreover, the shapes of DP CPT and DP HPT curves within unit I are partly interrupted by distinct peaks that perfectly correlate with clayey rip-up clasts, mud caps and intersecting silt laminae found within the sediment cores. All of these features underline the high-energy tsunami character of unit I deposits (Dawson & Stewart 2007) and show the powerful diagnostic capacities of DP sensing within the framework of palaeotsunami research.

The differentiation between unit II and unit III sediments was successfully based on differences in the DP CPT parameter u_2, the pore pressure showing a stepwise increase with increasing clay content due to decreasing permeability at all study sites (Sellwood et al. 2005, McCall et al. 2014). On the contrary, P_{inj} and EC show high values for both units II and III. Relative grain size frequency documents poor to moderate sorting for unit II with a dominance of coarse silt but still a distinct component of medium-grained sand. Therefore, moderate to high-energy transport must be assumed for unit II.

Unit III shows highest clay contents reflecting lagoonal facies described by Koster et al. (2015) for the Kaiafa Lagoon and by Willershäuser et al. (2015a) for the former Mouria Lagoon. DP HPT data underline the fine-grained character of unit III by increasing F_r, P_{inj} and EC and very

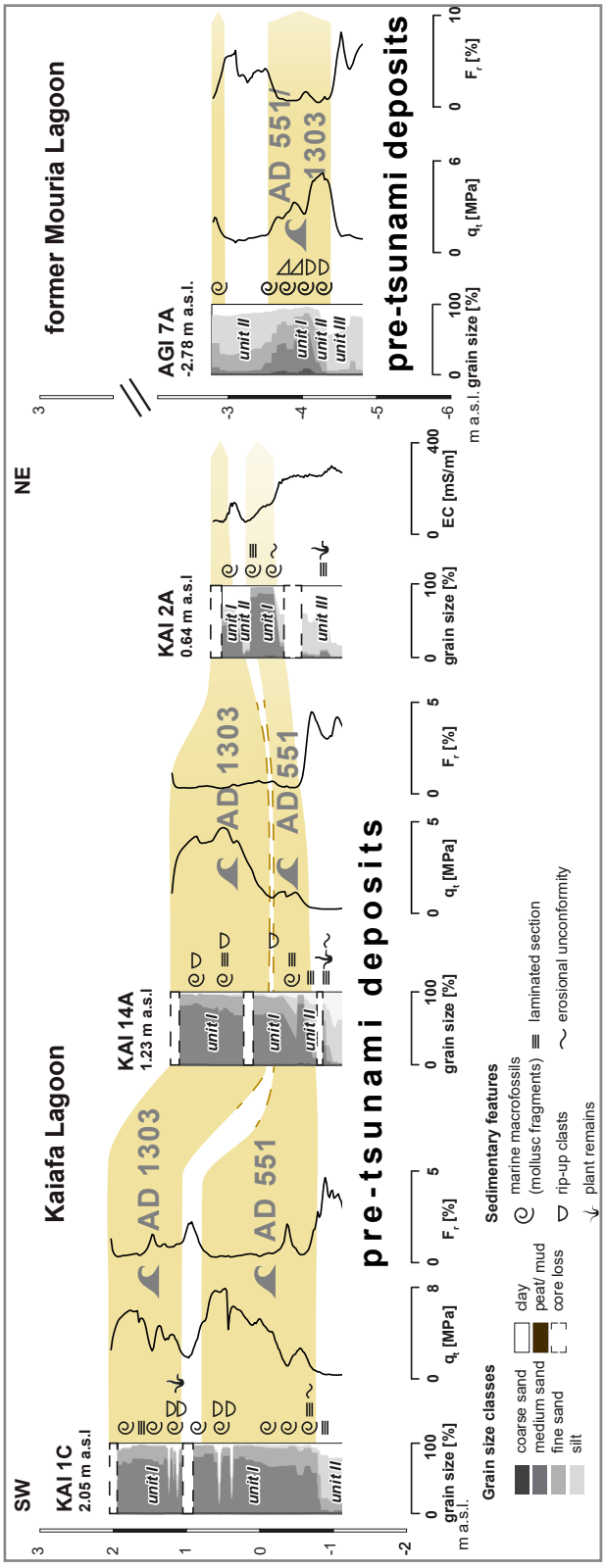

Fig. 4.17: Stratigraphic cross-section on vibracore and grain size data as well as selected DP data, indicating a twofold tsunami impact at the Kaiafa Lagoon and former Mouria Lagoon by tsunami events AD 551 and AD 1303.

low $K_{est.}$, reflecting low permeability but high conductivity of the material.

Further, increasing F_r values are described by Styllas (2014) as typical of prodelta, lagoonal and floodplain facies. However, unit III shows poor (AGI 7A) to moderate (KAI 1C and KAI 14A) sorting that does not reflect a completely quiescent waterbody. Vibracoring site AGI 7A is located at the immediate vicinity of the former lagoonal shore. Therefore, poor sorting may be due to different sediment transport processes including enrichment of lagoonal shore material as well as input of wind-blown sediments.

Poor sorting effects in the stratigraphic record of AGI SCPT 7 seem to be present down to 7.98 m below surface in the form of fluctuating q_t and F_r values. Since silt and clay show nearly identical q_t and F_r values (Lafuerza et al. 2005), a clear allocation of this section to unit II or unit III is difficult. However, it is very likely that there are intersecting coarser grained layers in an overall fine-grained matrix as decreasing F_r correlates well with increasing q_t and V_s. The latter indicate a higher shear strength related to coarser grained sediments (Robertson et al. 1986). These variations therefore most probably reflect lamination structures and alternating unit II and unit III layers (AGI 7A; 7.98 to 1.54 m below surface).

Comparing the seismic reflection profile AGI SEIS I and the DP data AGI (S)CPT/HPT 7 show that the heterogeneous stratigraphy out of unit II and III sediments form the infilling of channel B, the base of which was detected at c. 8 m below surface (Fig. 4.16; Results of direct push and seismic measurements at vibracoring site AGI 7A). The formation and incision of tsunami-related channels in coastal areas may be indicative of backwash dynamics during tsunami events as described by Bahlburg & Spiske (2012) for the 2010 Chile tsunami. However, it is also conceivable that erosional features recognized in conjunction with tsunami impacts is caused by high-energy landward flow of tsunami waters (Vött et al. 2009b, Willershäuser et al. 2015a). Clear evidence for increased transport energy is well-documented by decreasing u_2 values from 6.14 to 4.50 m below surface, defined as unit II at site AGI 7A. The stratigraphy of adjacent vibracore AGI 5 drilled by Willershäuser et al. (2015a) shows a diagnostic tsunami layer, 1.30 m thick, at the same depth (Fig. 4.12) where at site AGI 7A revealed a relatively increased unit II sand content compared to overlying and underlying units. Therefore, this study concludes that the erosion channel depicted in Fig. 4.16 was formed by tsunami impact that left moderate to high-energy (fluctuating) signals in the DP records. From c. 9 m below surface downward, channel sediments are underlain by a section of increasing u_2, decreasing q_t, low F_r and continuously low $K_{est.}$ values (Fig. 4.15) indicating low permeability within this unit. These sediments are most probably fine-grained lagoonal unit III deposits.

According to the SBT classification of units II and III at the Kaiafa Lagoon, sediments from these units are interpreted as dominated by silt and clay (SBT 3 and SBT 4) leading to an underestimation of the real sand content especially for unit II (Figs. 4.10 and 4.11). Since increasing contents of silt and clay cause higher plasticity, the SBT is controlled by the fine-grained component (Robertson 2009). Furthermore, thin intercalations within a sedimentary sequence are often difficult to identify using the SBT method because differences in stiffness may result in underestimation of the sediment strength in the case of intercalated sand layers and overestimation in the case of intercalated clay layers (Lunne et al. 2002). Hence, the SBT-

based classification of sedimentary units II and III and their layering becomes problematic because of increased contents of fine-grained sediments and complex (sub-)layering.

At the Kaiafa Lagoon site, distinct peat layers were part of the stratigraphic record of all vibracores. Comparing sediment cores and SBT classification, the SBT classification reveals a distinct underestimation of peat thickness; peat is also wrongly classified as 'clayey silt to silt'. The DP CPT-based classification of peat usually reveals low q_t values for amorphous peat and higher q_t values for peat with abundant fibres (Landva et al. 1983, Long & Boyland 2012). However, fibrous peat, as found in this study, is often falsely grouped into the SBT category 'mixed silt with clay' (Missiaen et al. 2015). Nevertheless, unit IV peat is clearly depicted in the DP CPT log by highest F_r values reaching up to 14% (Missiaen et al. 2015). Further, DP HPT data helped to detect unit IV by a noticeable increase of P_{inj} and EC within the peat section. The latter was also observed by Hausmann et al. (2016).

Modelling the total sand content by means of a linear regression equation based on DP HPT and DP (S)CPT data worked well and allows the identification of sand-dominated sections within the sedimentary record. Measured total sand contents were best approximated for vibracoring site KAI 14A with a R^2 of 0.97 and a RMSE of 6.87 of the corresponding linear regression equation. At vibracoring site KAI 1C, the real total sand content for unit I and partly unit II were slightly underestimated. This may be due to the differences in sampling numbers between unit I and units II and III (Fig. 4.5). Actually, the calculated sand content displays well the medium sand content that dominates the grain size composition of unit I. For the Mouria Lagoon site, the total sand content was mostly slightly overestimated with regard to vibracore AGI 7A. Conclusively, there is a local variability from sediment core to sediment core so that DP data cannot be globally used to estimate the absolute total sand content.

However, the DP-based calculation of the total sand content using Eqs. (1) to (3), allows the detection of intercalating sand layers within unit II (AGI 7A) and unit IV (KAI 1C and KAI 14A) that were not detected through core description and grain size analysis. Calculated data are supported by the descriptions of Koster et al. (2015) who found clastic sediment layers embedded within the peat at those depths where DP-based calculations show higher contents within cores KAI 1C and KAI 14A (Fig. 4.8). Further, the sharp contact to basal unit I is well depicted by the calculated total sand content at all sites. The basal unit I fine sand (Willershäuser et al. 2015a) at site AGI 7A is indicated by the increase of $K_{est.}$ compared with values measured for hanging units. Compared to the Mouria Lagoon, the stratigraphic record of the Kaiafa Lagoon is better suited to calibrate DP data. Good sorting of unit I, a wider variety of different sedimentary units within the stratigraphic record and a larger data set due to deeper coring result in higher accuracy regarding the calculation of the total sand content. Consequently, the statistical quality related to the identification of sand layers using a multivariate linear regression will be all the better, the more DP data are available and the better the degree in sorting and the higher the variability in grain sizes. Concerning DP SCPT, increasing the number of generated seismic impulses would certainly improve data resolution and the reconstruction of differences in grain size. For future studies, the authors recommend starting with DP HPT measurements as a base to determine target depths for seismic signals within the course of a subsequent DP SCPT log. Linear regression results solely

based on DP EC data (KAI 2A, KAI 6A and KAI 8A) revealed that the quality of the linear relation between grain size and EC is very site specific. It is thus problematic to reliably calculate the total sand content or to detect differences in the grain size distribution without having further information on the chemical composition and mineralogical characteristics of the subground material and the water content. The total sand content can only be reliably modelled based on additional DP-parameters such as DP CPT and DP HPT data, as was shown for the Kaiafa Lagoon and the former Mouria Lagoon.

4.5.2 Event chronostratigraphy

4.5.2.1 The Kaiafa Lagoon

Concerning the event chronostratigraphy for Kaiafa Lagoon, Koster et al. (2015) presented radiocarbon dating results for vibracore KAI 5A (Fig. 4.8). These authors conclude a *terminus post quem* of 432 to 540 cal AD (maximum age) and a *terminus ante quem* of 1291 to 1326 cal AD (minimum age) for tsunami impact on the Kaiafa coast as recorded in core KAI 5A. Sedimentary characteristics and absolute elevation of the tsunami deposits described by Koster et al. (2015) are strongly consistent with tsunami-related unit I presented in this study. Stratigraphic results by Koster et al. (2015) indicate two distinct tsunami- related layers separated by an intermittent fine-grained layer (Fig. 4.8). Similar findings in comparable depths are documented by vibracore KAI 2A showing two distinct high-energy layers separated by a silty clay layer. The embedded clay layer is documented by increasing EC values (Fig. 4.8). Moreover, sedimentary and DP CPT data retrieved from site KAI 1C show repeated coarsening upward cycles within unit I (Figs. 4.6 and 4.17) which is interpreted as caused by multiple tsunami impact. Both layers further show a thinning inland tendency along vibracore transect KAI 1C to KAI 14A to KAI 2A (Figs. 4.8). Fining inland of grain sizes due to decreasing flow velocity with increasing distance to the coastline are often reported for tsunami deposits (Moore et al. 2007, Higman & Bourgeois 2008, Szczucinski et al. 2012, Chagué-Goff et al. 2015).

At vibracoring site KAI 8A, a thick peat sequence repeatedly intersected by silt-dominated unit III sediments was found, the latter may represent the maximum landward inundation during tsunami landfall events at the Kaiafa Lagoon. At site KAI 8A, a *terminus post quem* of 800 to 771 cal BC and a *terminus ad* or *ante quem* of 625 to 655 cal AD were obtained for the possibly tsunami-related unit III layer from 3.35 to 2.40 m below surface (Fig. 4.8). A subsequent peat layer, indicating stable environmental conditions, is covered by another unit III layer (2.12 to 1.67 m below surface) for which an age of 561 to 603 cal AD was found. This age is regarded in this study as being related to a reworked sample because the following peat unit revealed a t*erminus ante quem* of 1523 to 1645 cal AD for the underlying fine-grained, clast dominated section at site KAI 8A.

Comparing the results of this study with the data presented by Koster et al. (2015), it is suggested that the sandy tsunami layer encountered at vibracoring site KAI 5A (Koster et al. 2015) and unit III deposits found at vibracoring site KAI 8A were deposited by the same event-related process. This study also further supports the idea of a two-fold tsunami impact at the Kaiafa Lagoon because the set of allochthonous clast deposits can be differentiated into

two event layers; separated by a thin layer of fine-grained deposits at sites KAI 5A and KAI 2A and by a peat layer at site KAI 8A (see above and Fig. 4.8). With regard to the entire transect and considering sandwich dating aspects, the age of the elder tsunami event (A) that hit the coast at the Kaiafa Lagoon can be time-bracketed between 432 to 540 cal AD (KAI 5) and 625 to 655 cal AD (site KAI 8A). This time window is highly consistent with the time-period for which outstanding historical earthquakes and associated tsunamis are reported, namely the AD 521/ 522 and AD 551 events (Guidoboni et al. 1994, Ambraseys 2009). For the same time-period, sedimentary evidence for tsunami landfall was found near Cape Katakolon and the adjacent ancient harbour of Pheia, located in the northwestern part of the Gulf of Kyparissia (Vött et al. 2011b). Also, Willershäuser et al. (2015a) presented evidence of a tsunami impact on the Mouria Lagoon in the northern central Gulf of Kyparissia that may fall into the same time-period. The findings of the current study suggest that the Gulf of Kyparissia was strongly hit by a major tsunami event (A) which is most possibly associated with the AD 551 earthquake for which various historical reports exist (Fig. 4.8).

With regard to the dating of the younger tsunami event (B), this study used the radiocarbon age obtained from vibracore KAI 5A, namely 1291 to 1326 cal AD maximum age. This is in contrast to Koster et al. (2015) and is explained as follows. The corresponding radiocarbon sample was collected from the uppermost part of the tsunami deposits (Koster et al. 2015: Fig. 4.8) so that the given age may rather be considered as *terminus ad* or *post quem* for tsunami impact due to possible reworking effects. Moreover, the age obtained from a sample retrieved from vibracore KAI 8A, namely 1523 to 1645 cal AD, has to be considered as *terminus ante quem* for the same event. Consequently, this gives a time window for event B which is defined as between 1291 to 1645 cal AD. Also for this time-period, there is reliable historical information on a major earthquake and tsunami impacts on the coasts of western Greece. Among other events, the current study focused on major earthquake and tsunami event that occurred in AD 1303 and for which considerable damage is reported (Guidoboni et al. 1994, Ambraseys 2009, Papadopoulos et al. 2014a). Tsunami candidate layers possibly corresponding to this major event are known from several coastal sections along the southern and western Peloponnese (Vött & Kelletat 2015). Based on this and the fact that the given radiocarbon time window for event B covers the beginning of the 14th Century, findings of this study suggest that the Gulf of Kyparissia may also have been hit by the AD 1303 event.

4.5.2.2 The former Mouria Lagoon

At the former Mouria Lagoon, tsunami deposits encountered in vibracore AGI 7A were not dated because appropriate datable organic material was not found. However, the age of the tsunamite can be estimated based on radiocarbon age data published by Willershäuser et al. (2015a) in conjunction with a vibracore transect across the former Mouria Lagoon (Fig. 4.12). These authors found that there are four different tsunami impacts, all with sedimentary, geochemical and microfaunal signals that can be detected in the corresponding coastal sequences. The youngest tsunami layer encountered (tsunami generation IV in Willershäuser et al. 2015a: Fig. 4.3) is stratigraphically consistent with the allochthonous tsunami sands detected at site AGI 7A (Fig. 4.12). The latter was cored in close proximity to coring site AGI 5 at the former lagoonal shore and can thus be easily integrated into the

transect reported by Willershäuser et al. (2015a). Age estimation for this tsunami impact is based on a radiocarbon sample retrieved from the tsunami unit itself at site AGI 6 and dated to 232 to 327 cal AD (Fig. 4.12; Willershäuser et al. 2015a; recalibrated to 235 to 329 cal AD). This age is considered as *terminus ad* or *post quem* for the associated tsunami event. Due to the strong stratigraphic consistencies and the fact that the site is subject to the same regional setting, it is concluded that this event is identical with event A or event B identified within the coastal deposits at the eastern shore of the Kaiafa Lagoon. Conclusively, this study suggests that the tsunami signal in core AGI 7A was also triggered by one of the two mentioned young historical earthquakes, either in AD 551 or in AD 1303.

4.6 Conclusions

Using direct push (DP) techniques within the framework of palaeotsunami research at the shores of the Gulf of Kyparissia, this study demonstrated the great potential of DP data in detecting stratigraphic units crucial in the identification of tsunami-related layers. DP data accurately reflect *in situ* lithostratigraphic information and changes of grain size with a resolution of 2 cm. Provided that a reference sediment core was drilled to define sedimentary units and calibrate DP data, DP techniques can be easily and efficiently used to collect high-resolution proxy data from wide areas.

Using this approach at two different study sites, namely at the Kaiafa and the former Mouria Lagoon, this study was able to trace and easily delimit sediment layers out of allochthonous sand intersecting silt-dominated lagoonal and backbeach swamp sequences. Allochthonous sand layers are interpreted as being deposited within the course of high-energy tsunami inundation. The soil behavior type (SBT) classification after Robertson (2009) was applied as a convincing tool for tracing tsunami signatures based on cone penetration test (DP CPT) data. Moreover, a multivariate linear regression function was derived from DP HPT and DP CPT data in order to model the total sand amount. This approach was tested and compared to measured grain size data. Both SBT classification as well as sand modelling based on DP data turned out to be extremely valuable tools to reliably recognize tsunami-related sand sheets and to estimate the total sand content. However, the method was not helpful to differentiate between tsunami-borne sand sheets on the one hand and basal littoral to marine sands on the other hand. Therefore, additional criteria were used to adequately distinguish between these different sedimentary facies. A qualitative data analysis of DP results allowed the recognition of erosional contacts and abrupt increase in grain size caused by tsunami inundation. Further, highly resolved DP data (CPT and HPT) such as EC, P_{inj}, $K_{est.}$, q_t, u_2 and F_r helped to identify typical features due to high-energy flooding processes such as fining and coarsening upward tendencies, muddy rip-up clasts embedded in a sandy sediment matrix, lamination of sediment layers. Direct push data also allowed the estimation of the degree of sediment sorting.

Direct push EC data and ERT measurements collected along a transect across a washover fan at the Kaiafa Lagoon documented a tsunami-related sand sheet over a distance of c. 260 m. In a further step, DP data was combined with surface-based ERT (Kaiafa Lagoon) and

seismic (former Mouria Lagoon) investigations. By this approach, it was possible to detect typical thinning inland characteristics of the tsunami-related sand sheet as well as subsurface erosional channels that were produced by high-energy impacts during tsunami landfall.

In summary, DP *in situ* sensing techniques are a very efficient, helpful and reliable tool within palaeotsunami research to detect sand-dominated tsunami layers emplaced within mud-dominated lagoonal and/or backbeach sedimentary environments. Beyond palaeotsunami research, the major advantages of using DP techniques in geomorphology and geosciences are as follows. The technique allows the collection of highly reliable and reproducible *in situ* stratigraphic data with a high-resolution of ≤2 cm without any gaps compared to core loss sections as they occur while coring. Moreover, DP techniques do not produce any compaction of the sediment during measurements. Also, DP techniques are several times quicker and less costly than coring. Finally, once combined with key sediment cores, DP techniques are highly useful to improve the significance of surface-bound geophysical prospection methods.

Using the DP techniques and based on further sedimentary data, sedimentary signatures of two young tsunami impacts that hit the Kaiafa Lagoon were detected. Radiocarbon age control allowed the identification of these tsunami layers as candidates for the AD 551 and AD 1303 earthquake and tsunami events. For these events, there is reliable historical data on major damage on infrastructure in western Greece and on the Peloponnese. At the former Mouria Lagoon, corroborating tsunami traces were found.

5. Synthesis

5.1 Evaluation of a combined approach using selected non-invasive and minimal-invasive methods for site characterization

The present study focuses on the applicability of non-invasive and minimal-invasive geophysical methods and their combination with stratigraphic data towards an improved characterization of the subsurface. Altogether, four different case studies were presented. The findings demonstrate that in Geoarchaeology and Quaternary Science, it is decisive to apply methods specifically adjusted to the individual research objective and to obtain a collection of valuable data. Furthermore, it was shown that combining different surface-based geophysical methods and especially surface-based geophysical methods with DP *in situ* logging clearly improve the information value of each method concerning the reconstruction of site formation processes (Fig. 5.1).

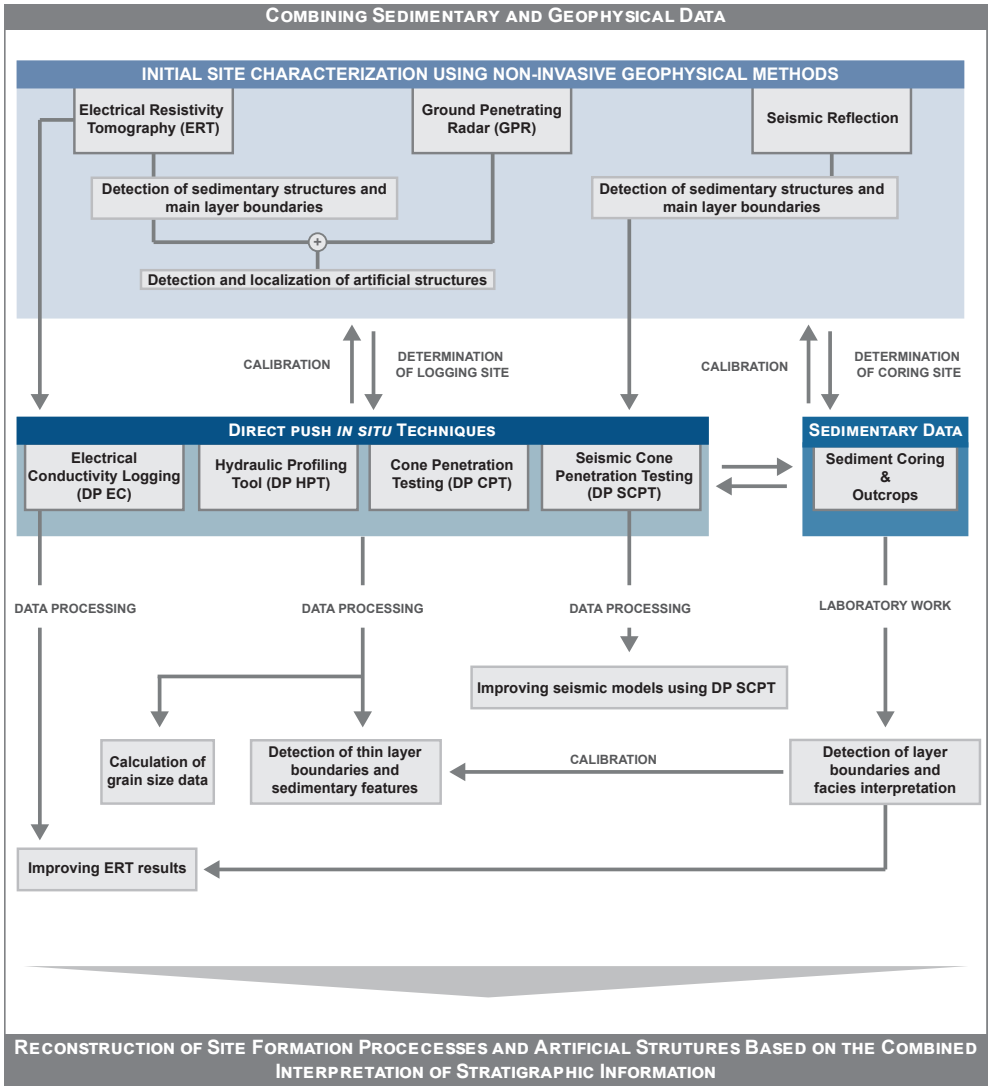

Fig. 5.1: Flow-chart of a combined application of non-invasive and minimal-invasive methods for reconstructing site formation processes.

The first case study (Chapter 2) focused on the detection of buried archaeological remains based on surface-related geophysical data. Geological information were deduced from geological maps on the one hand and inferred, on the other hand, from dominating sand- and siltstone formations visible at several outcrops. Variations in electrical resistivity values could be unambiguously assigned to differences in bedrock material while zones of extreme high electrical resistivity values were interpreted as air-filled intact cavities. In addition, the combination and cross-check of ERT with GPR data allowed for the detection and localization of chamber tombs, so far unknown (Fig. 5.1). Finally, comparing ERT results of three different burial sites enabled the differentiation between intact and collapsed chamber tombs. The investigations at Mageiras-Kioupia, Epitalio and Dartisa showed that non-invasive geophysical methods provide highly relevant data of archaeological context, at the same time preventing unnecessary costs and reducing impacts to the landscape. Subsequent archaeological excavations can thus be focused on geophysically detected structures most likely reflecting archaeological features.

For the complex stratigraphy of the Großkrotzenburg, floodplain ERT data alone did not allow for detailed reconstruction of the landscape evolution. ERT depth sections revealed adequate resolution to reconstruct the overall structure of the shallow subsurface and to detect a palaeochannel running parallel to the Roman fort. Similar findings were obtained at the Kaiafa Lagoon where ERT transects helped to identify the spatial extent of washover fans but did not resolve their internal structures and/or underlying sediment layers. Seismic reflection data deduced from surface-based prospection at the former Mouria Lagoon shows a better resolution compared to ERT studies. They allow for the detection of layer interfaces and an erosional channel. However, the difficulty of deriving the distinct grain size fractions from shear wave velocities still exists (Schön 2015, Wunderlich et al. 2018b). In all the cases studied, a better resolution of vertical data is crucial to reconstruct the local landscape evolution. An increased vertical resolution can be achieved by sediment coring. However, layer boundaries detected by surface-based geophysical methods are not necessarily caused by varying grain size composition (Fischer et al. 2016a, Wunderlich et al. 2018a). Therefore, non-invasive investigations were coupled with DP geophysical sensing techniques to obtain further information on the local stratigraphy. DP logging enable the collection of geophysical parameters in a vertical direction that can be directly linked to surface-based geophysical data and used as constraints for the geophysical model (e.g. electrical conductivity, seismic velocity).

The surface-related approach in geoarchaeological prospection was enlarged by DP EC logging and sediment coring within the framework of the Großkrotzenburg floodplain case study. It was further expanded by DP HPT and DP (S)CPT logging as far as concerns the Kaiafa and former Mouria Lagoon case study.

Doing so, non-invasive methods were useful to select representative DP sensing locations and to define the maximum sounding depth in order to depict e.g. channel structures and the entire sediment record. In addition, DP EC data combined with sediment cores allowed for an improved calibration of ERT depth sections as already pointed out by previous studies (Hausmann et al. 2013, Fischer et al. 2016a). Based on vertical stratigraphic information

deduced from DP sensing it was possible to differentiate between the ERT signal of bedrock material and bed load deposits of an active palaeo-river channel at the Großkrotzenburg floodplain. However, the investigations at Großkrotzenburg showed that the electrical conductivity (or resistivity) is not necessarily the ideal method to detect the Holocene basis. DP EC data required calibration by sediment cores due to variations of the weathering degree of Tertiary bedrock material which resulted in a large range of electrical conductivity. In contrast, changing stratigraphic conditions associated with fluctuations in grain size composition within the Holocene record were perfectly represented by DP EC data. Alltogether, the joint interpretation of non-invasive ERT data and direct investigations by sediment analysis and DP EC logging allowed for the reconstruction of former river channels, a possible Roman harbour situation and the impact of historic flood events on the overall floodplain evolution.

The advantage of using multiple DP techniques to detect small-scale sedimentary features and to reduce laboratory sediment analysis was further demonstrated by case study sites conducted at the Gulf of Kyparissia. Here, DP EC measurements were complemented by DP HPT (EC, P_{inj}, $K_{est.}$) and DP (S)CPT (V_s, q_t, f_t, u_2) investigations at the Kaiafa and former Mouria lagoons to improve the knowledge on the local stratigraphic architecture. Both methodological approaches produce reliable data to define layer boundaries with a vertical resolution of 2 cm as each parameter is a function of material behavior and/or grain size fluctuations (Robertson 2009, Leven et al. 2011, Geoprobe 2015). Furthermore, it became evident that the parameters q_t, f_t, F_r, P_{inj} and $K_{est.}$ show a high resolvability of thin layers such as laminated sequences within the investigated archives. Changes in the coarse-grained sediment fractions were best represented by q_t and V_s. Conversely, variations of fine-grained components were well represented by u_2. Finally, the application of DP techniques allowed for the estimation of sediment sorting by variable values of P_{inj}, q_t and F_r within one stratigraphic section. This large range of parameters improved the detection of layer boundaries considering high-energy tsunami sands, quiet reach silt and clay as well as peat units and small-scale sedimentary features (Figs. 5.1 & 5.2).

The collection of a comparable high-resolution data set solely based on DP EC or sediment coring is almost impossible and would require extreme small sampling intervals followed by costly laboratory investigations. In addition, the parameters q_t and f_t are not only functions of grain size composition but do also represent e.g. shear strength, bulk density and stiffness (Eslami & Fellenius 2004). Thus, it was possible to detect a multiphase tsunami impact at the Kaiafa and former Mouria Lagoon based on DP CPT values that were not indicated by grain size data presented in this study. In summary, the qualitative analysis of DP data clearly improved the knowledge on the local stratigraphic architecture since the combination of DP HPT and DP (S)CPT data produced an almost one-to-one image of the stratigraphic record.

Moreover, seismic DP *in situ* data can be compared with grain size data as well as other DP parameters. By this, a clear relation between the seismic signal and grain size composition was shown. The high correlation of specific, especially coarse-grained sediment units and seismic velocities was also shown by Wunderlich et al. (2018b) for surface-based seismic measurements. However, these authors discuss the problem of coarse resolution resulting in overestimated layer thickness. It is also difficult to deduce layer boundaries from DP SCPT

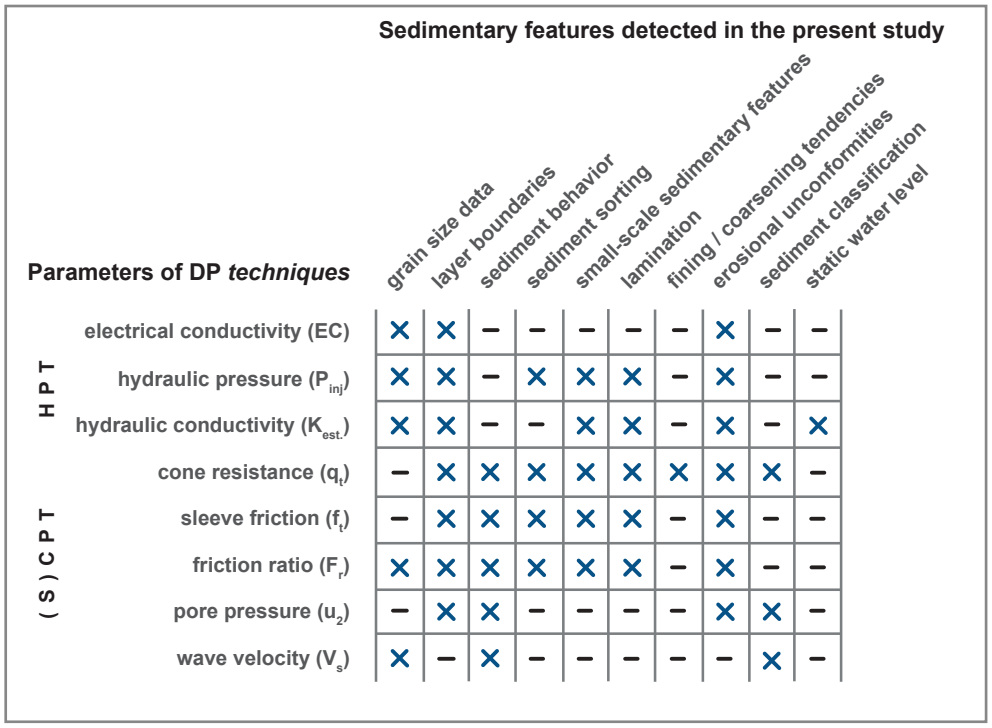

Fig. 5.2: Overview of sedimentary characteristics found within this study using DP HPT and DP (S)CPT measurements.

data since seismic velocities are measured between each generated seismic impulse that are defined by the user. To obtain the best result, the vertical resolution of DP SCPT logging should be determined depending on the thickniss of local stratigraphic units. Based on the present results it is suggested to conduct DP SCPT investigations subsequent to DP HPT logging, using the DP HPT results to define focus depths for seismic impulses. This is very coastly and time consuming in the case of complex stratigraphies and great logging depth. However, DP SCPT data turned out to be very useful to derive a depth function for the migration and depth conversion of surface-based seismic data. This allows for the correct allocation of depth and surface-based seismic velocities and a depth-specific correlation with grain size and DP *in situ* parameters. This information enables the interpretation of seismic profile signals even for lower sediment units where no core data were collected.

DP CPT data were additionally used to derive SBT classification after Robertson (1990). According to Eslami & Fellenius (2004) this soil chart is sufficiently developed to identify sediment types correctly. SBT classification were tested in the present study against grain size measurements of corresponding sediment cores, the analysis of individual DP CPT parameters and compared with results of a local multivariate linear regression to calculate the total sand content based on DP HPT and DP (S)CPT data. The results show great usability of SBTs to differentiate between coarse-grained and fine-grained sections. However, SBT classification is not appropriate for the identification of peat sections within the framework of our case studies. The method does not reflect variations in stiffness and therefore partly does not represent small-scale variations of grain size, particularly regarding the contents

of stilt and clay. Comparing laboratory grain size composition and SBT results for the Kaifa Lagoon and the former Mouria Lagoon, it is striking that the reliability of SBT decreases with decreasing degree of sediment sorting. KOSTER (2016) suggest the application of the ROBERSTON (1990) soil chart adjusted to the local lithology at the example of the Netherlands where a great number of DP CPT data are freely available from a national database. To evaluate a comparable local soil chart for the Kaiafa Lagoon and former Mouria Lagoon a significant increase of DP CPT data density would be necessary. Moreover, DP data obtained at the Gulf of Kyparissia underline the site-specific variations of each measured parameter even on a regional scale. Thus, a calibration of geophysical parameters by sediment data as it has been previously recommended by other authors (FISCHER et al. 2016a, WUNDERLICH et al. 2018a, 2018b) remains essential for each study site. Doing so, main grain size changes can be calculated based on a quantitative analysis of DP HPT and DP (S)CPT data. However, the qualitative analysis of single DP HPT and DP (S)CPT parameters is more favorable concerning the detection of small-scale variations within the stratigraphic record (Fig. 5.2).

Within the present study, each DP log were coupled with sediment core data for a detailed analysis on the relation between single DP HPT and DP CPT parameters and changes in grain size composition. For future investigations we recommend a reduction of the number of sediment cores as main grain size fluctuations can even be reliably estimated based on DP EC measurements. Based on the present results the following data acquisition is suggested to identify the best-possible idea of site formation processes in Geoarchaeology and Quaternary Science: An initial site characterization should be realized using surface-based geophysical methods to detect subsurface stratigraphic and possible man-made structures. If the stratigraphic architecture is of main interest, this approach should be followed by selected DP loggings. The geophysical parameters measured by DP logging should be at least correspond to the parameters measured by surface-based geophysical methods to improve the information value of geophysical models. For a detailed study on the sediment architecture a combination of different DP parameters is recommendend. Finally, sediment coring is needed to calibrate the geophysical data (Fig. 5.1).

Using DP sounding to a greater extent than sediment coring, data acquisition can be significantly accelerated as several sounding sites can be completed within one day. Furthermore, DP techniques may replace sediment coring in the case of sandy material where boreholes tend to collaps and coring progress is difficult. The application of different DP techniques is recommended since subsurface stratigraphies and structures can be better understood based on a bundle of different parameters. For example, additional DP CPT measurements at the Großkrotzenburg floodplain would have simplified the detection of bedrock. Moreover, the specific grain size composition and different sediment types can only be estimated by the combination of different geophysical DP parameters. Most DP probes, such as (S)CPT or HPT, are equipped with more than one sensor and different parameters can be recorded within one measurement. Furthermore, the spectrum of DP parameters of the DP system can be expanded at a later time by additional DP probes.

The number of sediment cores required for a reliable calibration of DP data strongly depends on the heterogeneity of the sediment structure and should be deduced from surface-based

geophysical data. Additional, sediment coring might be conducted when DP sounding was completed to select key sites for further analysis. In this way, facies interpretation and understanding of landscape formation processes can be improved.

Further, the horizontal correlation of layer boundaries derived from DP data along transects does not replace the necessity to proved geochronological control of landscape evolution. The geomorphogenetic interpretation of sediment units based on DP data for the case studies shown was realized on a solid base of stratigraphic, geochemic and geochronological data.

Beside the great advantages of using DP techniques for site characterization there are also a number of disadvantages (Tab. 5.1). The acquisition of DP equipment is very expensive as well as the maintenance of wear material. Furthermore, the sole application of DP logging is not advisable to reconstruct site formation processes. Therefore, the transport of many items is necessary when combining surface-based geophysical methods, different DP techniques and sediment coring. For this purpose, appropriate vehicles and authorized personnel are needed. Furthermore, DP logging can be only realized hen the terrain of interest is accessible by the DP machine (e.g. drill rig).

A technical problem still existing when comparing DP data with core data is the fact, that core data show depth offset due to compaction effects during the coring procedure. HAUSMANN et al. (2018) propose height correction by stretching sediment data within each 1 m long core section according to DP data. In our opinion, compaction effects are very specific in terms of material composition and the applied coring technique. Thus, height inaccuracies remain crucial and correction may end up in an additional source of errors. Therefore, we did not conduct height correction but used the DP data to identify disturbed sediment sections within sediment cores and to determine sampling intervals during core description.

	Pros	Cons
Direct push techniques	• time- *a*nd cost-efficient data collection • *in situ* measurement of several parameters • gapless and high-resolution data • increasing the maximum exploration depth • reduction of the number of sediment cores • improvement of geophysical models • reduction of laboratory analyses	• high aquisition costs of DP equipment • high maintenance costs • terrain accessible for DP machine • point information of stratigraphic architecture • calibration with sedimentary information • coastly transport

Tab. 5.1: Pros and cons of using DP techniques for site characterization.

5.2 Perspectives

The application of DP CPT sensing has become increasingly important for geo-scientific research during the last years (Campo et al. 2007, Amorosi et al. 2015, Missiaen et al. 2015, Delvoi et al. 2016, Zhang et al. 2018). Detailed DP CPT studies were undertaken to collect stratigraphic information with high significance for landscape reconstructions. Like the present PhD study, most of the published DP CPT investigations associate DP data with information deduced from sediment cores and combine this point information with surface-based geophysical investigations. Following this approach, the Holocene record and correlation of stratigraphic units were studied for fluvial and coastal areas in the Mediterranean (Amorosi & Marchi et al. 1999, Lafuerza et al. 2005, Campo et al. 2007, Styllas 2014). The stratigraphy at each of these sites is characterized by a succession of different facies that are separated from each other by a sharp change of grain size composition and therefore changing geotechnical behavior. DP CPT measurements in a tidal system of the eastern coastal plain in China were carried out by Zhang et al. (2018). All authors confirm the usability to differentiate between facies with changing mechanical behavior but point out the difficulties regarding the recognition of individual sediment layers when a sharp lithologic contrast is missing. An increasing complexity of data processing bound to decreasing differences between sediment units and the decreasing degree in sediment sorting was also shown for the Kaiafa Lagoon and the former Mouria Lagoon within the present study. However, the effectiveness of DP HPT data to detect small-scale changes in grain size such as thin layering was also demonstrated. The application of DP HPT measurements in hydraulic engineering is popular but the use in geo-scientific research is almost non-existent.

To underline the high potential for detecting different geomorphological and geoarchaeological features based on combined DP parameters, Fig. 5.3 presents unpublished DP HPT and DP CPT data sets obtained at different sites within the last year. A first study was carried out to detect the pre-Holocene topography presents near Accumersiel (North Sea coast, Germany) (Fig. 5.3A). The study site is located in the West Frisian marshland c. 2 km distant from the present back-barrier tidal basin of the Wadden Sea. The stratigraphic sequences of the wider area are characterized by Pleistocene glacial and fluvio-glacial deposits (Geest) overlain by Holocene sediments of varying thickness. The latter contain the typical sedimentary sequence of basal peat formation (unit I) followed by shallow quiet water (unit II) and finally tidal flat deposits (IV). All units are partly intersected by high-energy deposits (unit III). The upper stratigraphic section represents the development of the present marshland (unit V) (Chang et al. 2006, Bungenstock & Schäfer 2009, Wartenberg & Freund 2012, Wartenberg et al. 2013). The Holocene sequence of Accumersiel yields overall low q_t values due to the smooth behavior and loose packing of the sediments. However, the subdivision of different sediment units described for the wider study area can be easily derived from both q_t and DP EC logs. The Holocene-Pleistocene contact is marked by a distinct increase of q_t by a factor of c. 16 compared to mean Holocene q_t values (located at - 5.96 m a.s.l.). Styllas (2014) also used DP CPT data to detect a basal unit of late Pleistocene age showing similar results with maximum resistance for Pleistocene gravels. Beside DP CPT, DP EC measurements turned out to be a useful tool to map the Holocene-Pleistocene boundary of unconsolidated material at

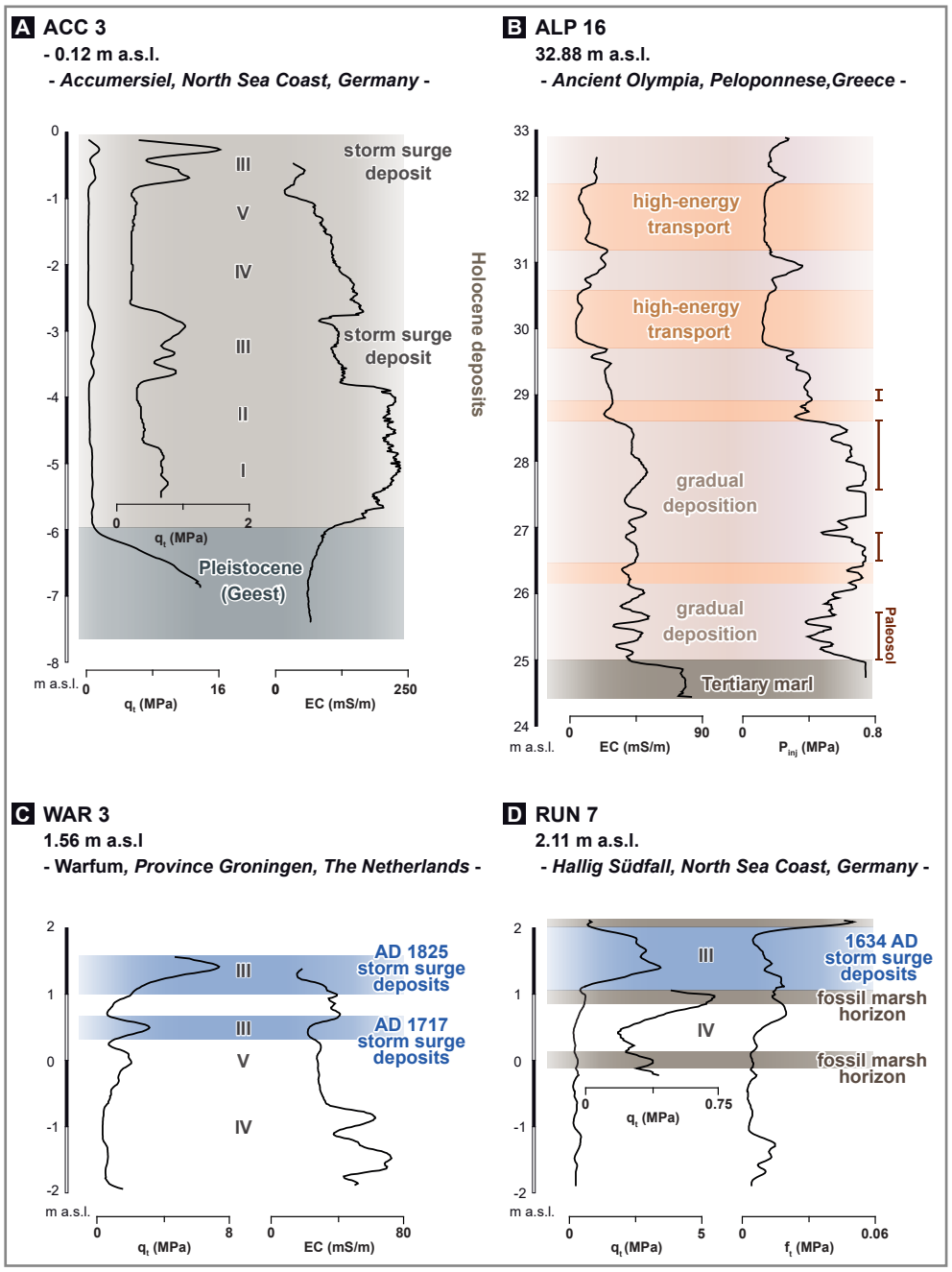

Fig. 5.3: Examples for further applications of DP HPT and DP CPT techniques. Note: Unit I – basal peat, Unit II – quiet reach deposit, Unit III – high-energy deposit, Unit IV – tidal flat deposit, Unit V – tidal marsh deposit.

Accumersiel. In contrast to DP CPT results, the transition zone is marked by a sharp decrease of DP EC values indicating the onset of low conductive Pleistocene sands.

The second exemplary data set depicted in Fig. 5.3B represents a sediment sequence of the so-called Olympia terrace (Vött 2013) near the sanctuary of ancient Olympia. Here, the Holocene base-level is shown by an abrupt increase of DP EC and P_{inj} values marking the transition to very stiff but conductive Tertiary marl (IGME 1982) at 25.01 m a.s.l. These examples emphasize once more the need of interpreting DP data in the context of local geological and geomorphological conditions. The example from Olympia was chosen to demonstrate the potential of DP HPT measurements to differentiate phases of gradual deposition at stable environmental conditions and short term high-energy impact triggered by changes in the overall geomorphodynamics. The evolution of the Olympia terrace is strongly influenced by sediment accumulation during high-energy flood events that mainly dominate the Holocene landscape evolution of the wider study area (Vött 2013, Vött et al. 2018a). These event layers are separated from each other by overbank deposits dominated by silt and clay showing partly thick palaeosols. High-energy sediment accumulation is marked by overall decreased DP EC and P_{inj} values. In contrast, fine-grained deposits are characterized by fluctuating but overall increased DP values. The fluctuation is caused by floodplain dynamics and the presence of ceramics and gravels within the palaeosol sequence. In accordance to the relation of flow velocity and grain size, silt and clay are generally accumulated under low-energy conditions and show higher conductivities compared to coarse-grained sediments (Wunderlich et al. 2013). In contrast, sand and gravels are characterized by a larger pore size compared to fine-grained sediments resulting in decreased hydraulic pressure and conductivity. Therefore, the interruption of gradual sediment accumulation by the impact of high-energy transport can be identified using DP HPT data independly from site specific sedimentary conditions.

The third example deals with another approach to use DP sensing techniques as a base for fast and reliable geo-scientific prospection. Storm surge signatures of the AD 1717 Christmas flood and the AD 1825 February flood (Meier 2011) in the Province of Groningen (West Frisia, The Netherlands) were investigated. Both storm events caused numerous dike failures the location of which was reconstructed based on historical records and topographic data. Studies were realized in the landward side of known dyke breaches ensuring that high-energy sedimentary features are directly linked to the AD 1717 AD or AD 1825 flood. Following this approach, sedimentary records at four dyke failure locations along a c. 35 km long coastal section as well as storm surge impact on the barrier island Ameland were investigated within 5 days only. Fig. 5.3C shows exemplary results for the Warfum site which is located at the landward site of a dyke breach of the AD 1825 flood. DP EC and q_t data indicate two inundation events by the storm surge (unit III: 0.32-0.67 m a.s.l, 1.09- 1.56 m a.sl.). Comparing DP data with the stratigraphy deduced from sediment cores, the lower sediment unit contains tidal flat deposits (uni IV, low q_t and high EC values) followed by a tidal marsh sequence (unit V, low q_t and decreasing EC values). A sharp contact with a significant increase of q_t and decrease of EC values indicates the accumulation of sand. This section is associated with the AD 1717 storm surge. After the storm, tidal marsh environmental conditions were re-established showing a fine-grained, laminated section (varying EC values). Further sediment accumulation was then

prevented by the emplacement of the dyke line in seaward direction. The uppermost unit is characterized by a second sharp increase to maximum q_t values indicating the dike failure caused by the AD 1825 storm surge resulting in the accumulation of sandy deposits.

The last case study represents DP meaasurements carried out at Hallig Südfall (North Sea coast, Germany) in order to detect historical land surfaces (Fig. 5.3D). The historical administrative district of *Edomsharde* was located within this area and since the 12th cent. AD, the settlement of *Rungholt* developed on the medieval marshland. Detailed geomorphological and geoarchaeological studies on the local landscape evolution and the impact of large historical storm surges were published by Hadler & Vött (2017) and Hadler et al. (2018). The authors found evidence for a fossil marsh associated with the cultural landscape of *Rungholt*. These marsh deposits are covered by storm deposits of the 1st Grote Mandrenke that took place in AD 1362. By the impact of this storm, the marshland was largely destroyed and transformed into a tidal flat environment (Hadler et al. 2018). The stratigraphic sequence at Hallig Südfall comprises a second phase of marsh formation that is intersected by another storm surge deposit associated with the 2nd Grote Mandrenke that occurred in AD 1634. Geochemical analyses of fossil marsh layers showed distinct features of weathering and soil formation (Hadler et al. 2018). Testing the potential of DP sensing to recognize the palaeo marsh surface, DP CPT sounding was conducted at coring site RUN 7A. DP CPT data show a clear signal associated with storm surge deposits (unit III: 1.07-2.01 m a.s.l.). In addition, the fossil marsh is depicted by significantly increasing q_t and decreasing f_t values compared to tidal flat deposits (-0.12-0.12 m a.s.l., 0.85- 1.05 m a.sl.). Obviously, the fossil marsh horizons are characterized by strong compaction and soil formation, these features producing clear DP CPT signals.

To sum up, beside DP CPT sounding, the use of DP SCPT, DP EC, reflectance spectra (VIS-NIR-EC) and colour logging (DP CLT) as well as combining different DP techniques are used for detecting archaeological features and palaeotopography reconstructions (Dalan et al. 2011, Matney et al. 2014, Koster et al. 2015, Missiaen et al. 2015, 2018, Fischer et al. 2016a, Hausmann et al. 2018). Despite the high potential and information value of DP HPT and DP CPT data in geoarchaeological and geomorphological research, the integration of additional parameters based on DP would allow for an improved characterization of sedimentary features.

The interpretation value of DP parameters used in this study could be enhanced by the complementary use of an acoustic measuring device for a more precise analysis of grain size composition (Chadwick & Arias 2014). An acoustic sound is generated by rolling and sliding of sediment grains as well as rearranging and crushing of particles during the penetration process of the DP CPT cone (Houlsby & Ruck 1998, Lunne et al. 2002). The audible noise is influenced by the grain size composition, sediment porosity, mineralogy and sand structure (Menge & van Impe 1995). The acoustic noise generally increases with increasing mean grain size and yields reliable information on layer boundaries and sediment properties, especially within the sand fraction (Tringale & Mitchel 1982, Lunne et al. 2002). To detect the acoustic noise during the penetration process, a DP CPT probe including a microphone within the tip is used. Houlsby & Ruck (1998) suggest to analyze the acoustic signal of the 13 kHz to 25 kHz

spectrum as sediment characteristics appear mostly within this range. Measurements within higher frequencies hold the risk of collecting background noise. By combining the acoustic signal with q_t, f_t and pore pressure, even thin silt and sand layers of different grain sizes (fine, medium, coarse) can be detected and the internal structure of sandy sections can be estimated (Menge & van Impe 1995). Therefore, the application of acoustic measurements would be very useful to distinguish between different energetic conditions in environments dominated by silts and sands as shown for the former Mouria Lagoon (Chapter 4).

However, for landscape reconstruction geochemical and microfaunal analyses are required for a reliable facies interpretation. This was realized for the Großkrotzenburg floodplain (colour, XRF; Chapter 2). So far, only few investigations on *in situ* geochemical testing were undertaken. Dalan et al. (2011) coupled a surface-based geophysical survey with DP color tests and downhole measurements (magnetic susceptibility, magnetic viscosity, conductivity) to map the depth of archaeological features and stratigraphic layers. The high potential of a spectrographic survey using *in situ* optical spectra to differentiate between subsurface archaeological features and the surrounded soil and sediment is presented by Matney et al. (2014). Sediment color can be used to obtain geochemical properties associated with specific depositional environments (e.g. oxidative/ reductive conditions) as well as mineralogy, organic matter and moisture content due to defined spectral response in the visible wavelength spectrum (Scheinost & Schwertmann 1999, Viscarra Rossel et al. 2006, Hausmann et al. 2016). Hausmann et al. (2016) present a dataset of combined DP color (CLP) and DP CPT log data with sediment information which improves the detection of small scale lithologic changes. DP CLP logging was also applied by Hausmann et al. (2018) presenting an impressive 2D cross-section of a buried historic canal structure (*Fossa Carolina*, Germany) with a vertical resolution of 5 mm. DP CLP data were calibrated by sediment and DP EC data verifying the Carolingian base level of the canal structure deduced from DP CLP sounding (Hausmann et al. 2018). However, to reconstruct the palaeolandscape and prevailing depositional conditions, *in situ* measurement of geochemical elements would be extremely suitable (Kabata-Pendias 2011, Chagué-Goff et al. 2017). X-ray fluorescence spectroscopy is a well-established technique for characterization of palaeo-environmental records providing a wide spectrum of chemical elements (Aldstadt & Martin 1997). High-resolution XRF data is given by *ex situ* measurements using portable XRF isntruments or a XRF core scanner (e.g. Richter et al. 2006, Weltje &Tjallingii 2008, Bloemsma et al. 2018) but the information on *in situ* conditions is limited due to sediment loss, disturbance or compaction during the drilling process (Hausmann et al. 2018). XRF *in situ* implementation using a DP CPT probe has been developed for investigations on contaminants to reduce both, the human health risk and exploration costs. The system contains a window on the side of the DP CPT probe allowing a continuous measurement of element concentration (Kurup et al. 2017). However, any application in geo-scientific investigations is missing so far.

A further step towards a better understanding of local palaeoenvironmental conditions based on DP data is the transmission of point information on a lateral scale using joint processing of DP information and surface-based geophysical data. Hunter et al. (2002) used seismic velocities to predict ground motions in response to earthquake events. The authors underline

that supplementing non-invasive seismic data with minimal-invasive DP SCPT data results in more accurate measurements of vertical shear wave velocities. This was confirmed by the present study using DP SCPT data to migrate and convert surface-based seismic reflection data to depth. The results enabled a much more detailed interpretation of the seismic profile at the Mouria Lagoon concerning the detection of subsurface structures and the relation of seismic velocities and grain size distribution (Chapter 4). Schmelzbach et al. (2011) present a similar approach using DP CPT, DP HPT and DP dielectric measurements in combination with sediment cores to refine depth accuracy of surface-based GPR data. Conversely, 3D GPR data was used as a constraint for horizontal interpolation of 1D direct investigations (Schmelzbach et al. 2011). To analyze ERT data, DP results were qualitatively integrated in the data processing of electrical resistivity at the Großkrotzenburg floodplain (Chapter 3) and the Kaifa Lagoon (Chapter 4). A further step would be the application of a quantitative approach using stratigraphic data as the base for calculating mathematical constraints for ERT computation (Fischer et al. 2016). The integration of DP EC values in the ERT inversion process increases the vertical resolution of ERT depth sections. Furthermore, Fischer et al. (2016) underline the need of DP techniques to enhance ERT models (Fischer et al. 2016). Sediment data or other geophysical data (e.g. seismic, GPR), commonly used as numerical constraints (Hausmann et al. 2013, Zhou et al. 2014, Wunderlich et al. 2018b), do not necessarily represent layer boundaries of electrical resistivity (Wunderlich et al. 2018a). According to Wunderlich et al. (2018a), most reliable ERT inversion is obtained using local lithologic and blocked DP EC data (Davis & Christensen 2013) as mathematical constraints resulting in a very accurate ERT image. The integration of additional DP parameters indicating for example porosity, pore pressure, density or even chemical composition might be helpful for further development of geophysical models when combing indirect and direct geo-scientific methods.

6. Conclusions

The PhD thesis at hands showed the essential need to combine non-invasive and minimal-invasive methods in Geoarchaeology and Quaternary Science and underlined the high potential of DP techniques for understanding complex stratigraphies and enable landscape reconstructions. Based on the results the following conclusions can be made:

I) The combination of different geophysical methods clearly improve the detection of near surface stratigraphic and man-made structures as the joint interpretation of geophysical parameters, measured by different suface-based methods, enable a cross-check of detected subsurface anomalies. In a further step, high-resolution minimal-invasive geophysical parameters deduced from DP in situ data, such as DP EC or seismic velocities, allowed for a verification of layer boundaries depicted by non-invasive surface-based methods.

II) Sedimentological characteristics and geophysical information can be directly linked to each other. In this way a detailed reconstruction of the subsurface structure can be realized providing valuable information on the palaeoenvironment.

III) The application of DP techniques clearly improves the reconstruction of landscape formation processes concerning geomorphodynamic conditions. The transition from a low to a high-energy environment for example produces a neat signal in DP HPT and DP CPT logs due to changing grain sizes. Further, detailed analyses of DP parameters lead to significantly improved stratigraphic interpretations of the shallow sub-surface, for example the detection of small-scale sedimentary features.

IV) The use of DP techniques for site characterization increases both the cost and time efficiency. Several DP logs can be realized within one day providing high-resolution data. Once a calibration of DP data with sedimentary data is achieved, DP techniques are highly useful to identify sedimentary conditions and spatial variabilities. The application of DP techniques improve data processing of surface-based geophysical models resulting in a more precise interpretation of lateral subsurface conditions.

References

A

Ad-hoc-AG Boden (eds.) (2005): Bodenkundliche Kartieranleitung. – Schweizerbart, pp. 438, Stuttgart.

Aldstadt, J.H. & Martin A.F. (1997): Analytical Chemistry and the Cone Penetrometer: In Situ Chemical Characterization of the Subsurface. – Microchimica Acta **127**: 1-18.

Ambraseys, N. (2009): Earthquakes in the Mediterranean and Middle East. A multidisciplinary study of seismicity up to 1900. – Cambridge University Press, pp. 947, Cambridge.

Ambraseys, N. & Synolakis, C. (2010): Tsunami catalogues for the Eastern Mediterranean, revisited. – Journal of Earthquake Engineering **14**: 309-330.

Amorosi, A. & Marchi, N. (1999): High-resolution sequence stratigraphy from piezocone tests: an example from Late Quaternary deposits of the southeastern Po Plain. – Sedimentary Geology **128**: 67-91.

Amorosi, A. & Milli, S. (2001): Late Quaternary depositional architecture of Po and Tevere river deltas (Italy) and worldwide comparison with coeval deltaic successions. – Sedimentary Geology **144**: 357-375.

Anthony, E.J. (2014): Deltas. – In: Masselink, G & Gehrels, R. (eds.): Coastal Environments & Global Change. – John Wiley & Sons Ltd., pp. 155-166, New York.

Asselman, N.E.M & Middelkoop, H. (1998): Temporal variability of contemporary floodplain sedimentation in the Rhine-Meuse delta, the Netherlands. – Earth Surface Processes and Landforms **23**: 595-609.

Astin, T., Eckardt, H. & Hay, S. (2007): Resistivity Imaging Survey of the Roman Barrows at Bartlow, Cambridgeshire, UK. – Archaeological Prospection **14**: 24-37.

Athanassas, C. & Fountoulis, I. (2013): Quaternary neotectonic configuration of the southwestern Peloponnese, Greece, based on luminescence ages of marine terraces. – Journal of Earth Sciences **24**: 410-427.

Avramidis, P., Gerada, M., Lazarova, M. & Kontopoulos, N. (2013): Holocene record of environmental changes and palaeoclimatic implications in Alykes Lagoon, Zakynthos Island, western Greece, Mediterranean Sea. – Quaternary International **293**: 184-195.

B

Baginska, I., Janecki, W. & Sobótka, M. (2013): On the interpretation of seismic cone penetration test (SCPT) results. – Studia Geotechnica et Mechanica **XXXV**: 3-11.

Bahlburg, H. & Spiske, M. (2012): Sedimentology of tsunami inflow and backflow deposits: key differences revealed in a modern example. – Sedimentology **59**: 1063-1086.

Baker, V.R. (1987): Palaeoflood hydrology and extraordinary flood events. – Journal of Hydrology **96**: 79-99.

Baker, V.R., Webb, R.H. & House, P.K. (2002): The scientific and societal value of palaeoflood hydrology. – In: House, P.K., Webb, R.H., Baker, V.R. & Levish, D.R. (eds.): Ancient floods, Modern Hazards: Principles and Applications of Palaeoflood Hydrology. – American Geophysical Union, Water Science and Application Series, pp. 1-19, Washington, DC.

Barsch, H., Billwitz, K. & Bork, H.-R. (eds.) (2000): Arbeitsmethoden in Physiogeographie

und Geoökologie. – Klett Verlag, pp. 612, Stuttgart.

Bates, M.R., Bates, C.R. & Whittaker J. (2007): Mixed Method Approach to the Investigation and Mapping of Buried Quaternary Deposits: Examples from Southern England. – Archaeological Prospection **14**: 104-129.

Becker, T. (2014): Neue Forschungen zur Umwehrung des Kastells Großkrotzenburg. In: Henrich, P. (ed.): Der Limes in Raetien, Ober- und Niedergermanien vom 1. bis 4. Jahrhundert. Beiträge zum Welterbe Limes 8. – K. Theiss Verlag, pp. 149-163, Darmstadt.

Benito, G., Sánchez-Moya, Y. & Sopeña, A. (2003): Sedimentology of high-stage flood deposits of the Tagus River, Central Spain. – Sedimentary Geology **157**: 107-132.

Benito, G. & Thorndycraft, V.R. (2005): Palaeoflood hydrology and its role in applied hydrological sciences. – Journal of Hydrology **313**: 3-15.

Benito, G. & Díez-Herrero, A. (2015): Palaeoflood Hydrology: Reconstruction Rare Events and Extreme Flood Discharge. – In: Shroder, J.F., Paron, P. & Di Baldassarre, G. (eds.): Hydro-Meteorological Hazards, Risks, and Disasters. – Elsevier, pp. 65-105, Amsterdam.

Berktold, A., Biltgenbach, T., Greinwald, S., Illich, B., Jacobs, F., Kolodziey, A.W., Lange, G., Maurer, H.M., Prdcser, E., Pfeiffer, B., Pretzschner, C., Radic, T., Schaumann, G., Rezessy, G., Sebulke, J., Seidel, K., Szabaavary, L., Vertesy, L., Vogt, R., Weidelt, P., Weller, A. & Wolff, U. (2005): Geoelektrik. – In: Knödel, K., Krummel, K., Lange, G. (eds.): Handbuch zur Erkundung des Untergrundes von Deponien und Altlasten. – Springer, pp. 71-241, Berlin, Heidelberg.

Berner, Z.A., Bleeck-Schmidt, S., Stüben, D., Neumann, T., Fuchs, M. & Lehmann, M. (2012): Floodplain deposits: A geochemical archive of flood history - A case study on the River Rhine, Germany. – Applied Geochemistry **27**: 543-561.

Bigman, D.P. (2014): Mapping social relationships: geophysical survey of a nineteenth-century American slave cemetery. – Archaeological and Anthropogenical Science **6**: 17-30.

Blindow, N. (2006): Ground penetrating radar. – In: Kirsch, R. (ed.): Groundwater Geophysics. – Springer, pp. 227-252, Berlin, Heidelberg.

Bloemsma, M., Croudace, I., Dalyc, J.S., Edwards, R.J., Francus, P., Galloway, J.M., Gregory, B.R.B., Huang, J.-J. S., Jones, A.F., Kylander, M., Löwemark, L., Luo, Y., Maclachlan, S., Phlendorf, C., Patterson, R.T., Pearce, C., Profe, J. & Turner, J.N. (2018): Practical guidelines and recent advances in the Itrax XRF core-scanning procedure. – Quaternary International, in press. doi: https://doi.org/10.1016/j.quaint.2018.10.044.

Bondevik, S., Svendsen, J.I. & Mangerud, J. (1997): Tsunami sedimentary facies deposited by Storegga tsunami in shallow marine basins and coastal lakes, western Norway. – Sedimentology **44**: 1115-1131.

Bonhoff, M., Harjes, H.O. & Meier, T. (2005): Deformation and stress regimes in the Hellenic subduction zone from focal Mechanisms. – Journal of Seismology **9**: 341-366.

Booth, A.D., Szpakowska, K., Pischikova, E. & Griffin, K. (2015): Structure of an Ancient Egyptian Tomb Inferred from Ground-Penetrating Radar Imaging of Deflected Overburden Horizons. – Archaeological Prospection **22**: 33-44.

Boyd, M.J. (2002): Middle Helladic and Early Mycenaean Mortuary Practices in the Southern and Western Peloponnese. – Archaeopress, pp. 259, Oxford.

Brázdil, R. Glaser, R., Pfister, C., Dobrovolný, P., Antoine, J.-M., Barriendos, M., Camuffo, D., Deutsch, M., Enzi, S., Guidoboni, E., Kotyza, O. & Sanchez Rodrigo, F. (1999): Flood events of selected European rivers in the sixteenth century. – Climatic Change **43**: 239-285.

Brázdil, R., Kundzewicz, Z.W., Benito, G., Demarée, G., Mcdonald, N. & Roald, L.A. (2012): Historical floods in Europe in the past millennium. – In: Kundzewicz, Z.W. (ed.): Changes in Flood Risk in Europe. – CRC Press, pp. 121-166, Wallingford, Oxfordshire.

Brown, A.G. (1997): Alluvial geoarchaeology: floodplain archaeology and environmental change. – Cambridge University Press, pp. 374, New York.

Brückner H. (2007): Holozäne Umweltrekonstruktion und Geoarchäologie. – Zeitschrift für Geomorphologie N.F., Supplementary Issue **148**: 55-58.

Brückner, H., Vött, A. (2008): Geoarchäologie – eine interdisziplinäre Wissenschaft par excellence. In: Kulke, E., Popp, H. (eds.): Umgang mit Risiken. Katastrophen – Destabilisierung – Sicherheit. 56. Deutscher Geographentag 2007. – Tagungsband herausgegeben im Auftrag der Deutschen Gesellschaft für Geographie, pp. 181-202, Berlin, Bayreuth.

Bumberger, J., Paasche, H. & Dietrich, P. (2015): Systematic description of direct push sensor systems: A conceptual framework for system decomposition as a basis for the optimal sensor. – Journal of Applied Geophysics **112**: 210-217.

Bungenstock. F. & Schäfer, A. (2009): The Holocene relative sea-level curve for the tidal basin of the barrier island Langeoog, German Bight, Southern North Sea. – Global Planetary Change **66**: 34-51.

Buske, S., Gutjahr, S. & Sick, C. (2009): Fresnel volume migration of single-component seismic data. – Geophysics **74**: WCA47-WCA55.

Butler, D.K. (2008): Detection and Characterization of subsurface cavities, tunnels and abounded mines. – Near Surface Geophysics and Human Activity: 578-581.

C

Campanella, R.G. & Weemees, I. (1990): Development and use of an electrical resistivity cone for groundwater contamination sites. – Canadian Geotechnical Journal **27 (5)**: 557-567.

Campo, B., Amorosi, A. & Vaiani, S.C. (2017): Sequence stratigraphy and late Quaternary paleoenvironments evolution of the Northern Adriatic coastal plain (Italy). – Palaeogeography, Palaeoclimatology, Palaeoecology **466**: 265-278.

Cardarelli, E., Cercato, M., Cerreto, M. & Di Filippo, D. (2010): Electrical resistivity and seismic refraction tomography to detect buried cavities. – Geophysical Prospection **58**: 685-695.

Casten, U. (2008): Geophysikalische Erkundungsmethoden in der Archäologie. – In: Hauptmann, A. & Pingel, V. (eds.): Archäometrie. Methoden und Anwendungsbeispiele. – Schweizerbart'sche Vergalsbuchhandlung, pp. 221-236, Altenburg.

Chadwick, D.B. & Arias, E. (2014): Demonstration of an In-Situ Friction-Sound Probe for Mapping Particle Size at Contaminated Sediment Sites. – Technical Report 2040, SSC Pacific, pp. 77, San Diego.

Chagué-Goff, C., Goff, J., Wong, H.K.Y. & Cisternas, M. (2015): Insights from geochemistry and diatoms to characterise a tsunami's deposits and maximum inundation limit. – Marine Geology **359**: 22-34.

Chagué-Goff, C., Szczucinski, W. & Shinozaki, T. (2017): Applications of geochemistry in tsunami research: A review. – Earth-Science Reviews **165**: 203- 244.

Chang, T.S., Flemming, B.W., Tilch, E., Bartholomä, A., Wöstmann, R. (2006): Late Holocene stratigraphic evolution of a back-barrier tidal basin in the East Frisian Wadden Sea,

southern North Sea: transgressive deposition and its preservation potential. – Facies **52**: 329-340.

Chen, R., Tian, G., Zhao, W., Wang, Y & Yang, Q. (2018): Electrical Resistivity Tomography with angular separation for characterization of burial mounds in Southern China. – Archaeometry **60 (5)**: 1122-1134.

Claerbout, J.F. (1985): Imaging the Earth's Interior. – Blackwell Scientific Publications, pp. 274, Oxford.

Cita, M.B. & Rimoldi, B. (1997): Geological and geophysical evidence for a Holocene tsunami deposit in the Eastern Mediterranean deep-sea record. – Journal of Geodynamics **24**: 293-304.

Conyers, L.B. (2006): Ground-penetrating Radar Techniques to Discover and Map Historic Graves. – Historical Archaeology **40**: 64-73.

Conyers, L.B. (2013): Ground-Penetrating Radar for Archaeology. – AltaMira Press, pp. 241, Lanham, New York, Toronto, Plymouth.

Costa, P.J.M., Andrade, C., Cascalho, J., Dawson, A.G., Freutas, M.C., Paris, R. & Dawson, S. (2015): Onshore tsunami sediment transport mechanisms inferred from heavy mineral assemblages. – The Holocene **25**: 1-15.

Costa, P.J.M., Costas, S., González-Villanueva, R., Oliveira, M.A, Roelvink, D., Andrade, C., Freitas, M.C., Cunha, P.P., Martins, A., Buylaert, J.-P. & Murray, A. (2016): How did the AD 1755 tsunami impact on sand barriers across the southern coast of Portugal? – Geomorphology **268**: 296-311.

Csibri, T., Lácny, A., Putiška, R., Dostál, I. & Kušnirák, D. (2018): The depth range and possible continuation of the Havranická jaskyňa cave system revealed by geological methods and electrical-resistivity tomography (ERT), the Malé Karpaty Mts., Slovakia. – Mineralia Slovaca **50**: 37-46.

Cuven, S., Paris, R., Falvard, S. & Miot-Noirault, E. (2013): High-resolution analysis of a tsunami deposit: Case-study from the 1755 Lisbon tsunami in southwestern Spain. – Marine Geology **331**: 98- 111.

D

Dalan, R.A., Bevan, B.W., Goodman, D., Lynch, D., de Vore, S., Adamek, S., Martin, T., Holley, G. & Michlovic, M. (2011): The Maesurement and Analysis of Depth in Archaeological Geophysics: Tests at the Biesterfeldt Site, USA. – Archaeological Prospection **18**: 245-265.

Dawson, A.G. & Stewart, I. (2007): Tsunami deposits in the geological record. – Sedimentary Geology **200**: 166-183.

De Martini, P.M., Barbano, M.S., Smedile, M.S., Geradi, F., Pantosti, D., Del Carlo, P. & Pirrotta, C. (2010): A unique 4000 year long geological record of multiple tsunami inundations in the Augusta Bay (eastern Sicily, Italy). – Marine Geology **276**: 42-57.

Deiana, R., Leucci, G. & Martorana, R. (2018a): New Perspectives on Geophysics for Archaeology: A Special Issue. – Surveys in Geophysics **39 (6)**: 1035-1038.

Deiana, R., Bonetto, J. & Mazzariol, A. (2018b): Integrated Electrical Resistivity Tomography and Ground Penetrating Radar Measurements Applied to Tomb Detection. – Surveys in Geophysics **39**: 1081-1105.

Delvoi, S., Boulvain, F., Charlier, R., Collin, F. (2016): Detailed characterization of the Late

Pleistocene loess sequence stratigraphy of Remicourt (Hesbaye region, Belgium) with cone penetration tests. – Geologica Belgica **19 (3-4)**: 281-289.

Demuth, D., Bumberger, J. & Paasche, H. (2015): Evaluation of direct push probes: Sensor interface analysis of DC resistivity probe. – Journal of Applied Geophysics **122**: 218-225.

Dickinson, O.T.P.K. (1983): Cist graves and Chamber Tombs. – The Annual of the British School at Athens **78**: 55-67.

Dietrich P. & Leven C. (2006): Direct Push-Technologies. – In: Kirsch, R. (ed.): Groundwater Geophysics. – Springer, pp. 321-340, Berlin, Heidelberg.

Dietrich, P., Butler, J.J. & Feiss, K. (2008): A Rapid Method for Hydraulic Profiling in Unconsolidated Formations. – Ground Water **46 (2)**: 323-328.

Dikau, R., Moldenhauer, K.-M., Badehäsing, J. (eds.) (2007): Die Erdoberfläche – Lebens- und Gestaltungsraum des Menschen. – Zeitschrigt für Geomorphologie **148**: 1-192.

Dikau, R. (2007): Potenziale neuer Methoden für die Geomorphologie. – Zeitschrift für Geomorphologie N.F., Supplementary Issue **148**: 102-103.

Direct Image (2008): Electrical Conductivity (EC) Logging. Standard Operating Procedure. – Direct Image, Salina, KS.

Dominey-Howes, D., Cundyc, A. & Croudacec, I. (2000): High energy marine flood deposits on Astypalaea Island, Greece: possible evidence for the AD 1956 southern Aegean tsunami. – Marine Geology **163**: 303-315.

Doolittle, J.A. & Bellantoni, N.F. (2010): The search for graves with ground-penetrating radar in Connecticut. – Journal of Archaeological Science **37**: 941-949.

Doran, G.H. (2013): Excavating wet sites. – In: Menotti, F., O'Sullivan, A. (eds.), The Oxford Handbook of Wetland Archaeology. – Oxford University Press, pp. 483-494, Oxford.

Drexel, F. (1910): Das Kastell Stockstadt. – In: Fabricius, E., Hettner, F. & von Sarwe, O. (eds.): Der Obergermanisch-Raetische Limes des Roemerreiches des Römerreichs, Heft A3/33. Otto Petters, pp. 32-38, Heidelberg, Berlin, Leipzig.

E

Eitel, B. (ed.) (2006): Holocene Landscape Development and Geoarchaeological Research. – Zeitschrift für Geomorphologie **142**: 1-388.

Ellwood, B.B. (1990): Electrical Resistivity Surveys in Two Historical Cemeteries in Northeast Texas: A Method for Delineating Unidentified Burial Shafts. – Historical Archaeology **24**: 91-98.

Ernston, K. & Kirsch, R. (2006): Geoelectrical methods. – In: Kirsch, R. (ed.): Groundwater Geophysics. – Springer, pp. 85-119, Berlin, Heidelberg.

Eslami, A. & Fellenius, H. (2004): CPT and CPTu data for soil profile interpretation: Review of methods and a proposed new approach. – Iranian Journal of Science & Technology **28**: 69-86.

F

Finkler, C., Fischer, P., Kaika, K., Rigakou, D., Metallinou, G., Hadler, H. & Vött. A. (2018a): Tracing the Alkinoos Harbor of ancient Kerkyra, Greece, and reconstructing its paleotsunami history. – Geoarchaeology **33**: 24-42.

Finkler, C., Baika, K., Rigakou, D., Metallinou, G., Fischer, P., Hadler, H., Emde, K. and Vött, A.

(2018b): Geoarchaeological investigations of a prominent quay wall in ancient Corcyra – implications for harbour development, palaeoenvironmental changes and tectonic geomorphology of Corfu island (Ionian Islands, Greece). – Quaternary International **473 A**: 91-111.

Finkler, C., Baika, K., Rigakou, D., Metallinou, G., Fischer, P., Hadler, H., Emde, K. & Vött, A. (2018c): The sedimentary record of the Alkinoos Harbour of ancient Corcyra (Corfu Island, Greece) – geoarchaeological evidence for rapid coastal changes induced by co-seismic uplift, tsunami inundation and human interventions. – Zeitschrift für Geomorphologie N.F., Supplementary Issue **62**: 001-050. doi: https://doi.org/10.1127/zfg_suppl/2018/0514.

Fischer, P., Wunderlich, T., Rabbel, W., Vött, A., Willershäuser, T., Baika, K., Rigakou, D. & Metallinou, G. (2016a): Combined electrical resistivity tomography (ERT), direct-push electrical conductivity logging (DP-EC) and coring – a new methodological approach in geoarchaeological research. – Archaeological Prospection **23 (3)**: 213-228.

Fischer, P., Fibkler, C., Röbke, B.R., Baika, Kalliopi, Hadler, H., Willershäuser, H., Rigakou, D., Metallinou, G. & Vött, A. (2016b): Impact of Holocene tsunamis detected in lagoonal environments on Corfu (Ionian Islands, Greece): Geomorphological, sedimentary and microfaunal evidence. – Quaternary International **401**: 4-16.

Foulds, S.A., Griffiths, H.M., Macklin, M.G. & Brewer, P.A. (2014): Geomorphological records of extreme floods and their relationship to decadal-scale climate change. – Geomorphology **216**: 193-207.

Fountoulis, I. & Mariolakos, I. (2008): Neotectonic folds in the central-western Peloponnese, Greece. – Zeitschrift der deutschen Gesellschaft für Geowissenschaften **159**: 485- 494.

Frederick, C. (2001): Evaluating Causality of Landscape Change: Examples from Alluviation. – In: Goldberg, P., Holliday, V.T. & Ferring, C.R. (eds.): Earth Science and Archaeology. – Kluwer Academic/ Plenum Publischer, pp. 55-77, New York, Boston, Dordrecht, London, Moscow.

G

Gębica, P., Starkel, L., Jacyšyn, A. & Krąpiec, M. (2013): Medieval accumulation in the Upper Dniester river valley: The role of human impact and climate change in the Carpathian Foreland. – Quaternary International **293**: 207-218.

Gębica, P., Jacyšyn, A., Krąpiec, M., Budek A., Czumak, N., Starkel, L., Andrejczuk, W. & Ridush, B. (2016): Stratigraphy of alluvia and phases of the Holocene floods in the valleys of the Eastern Carpathians foreland. – Quaternary International **415**: 55-66.

Geoprobe (2015): Geoprobe Hydraulic Profiling Tool (HPT) System. Standard Operating Procedure. – Geoprobe Technical Bulletin **MK313**: 1-22.

Gerlach, R. (1995): Die hydrologischen und klimatischen Bedingungen des Wassernetzes im römischen Germanien. – Archäologische Korrespondenzblatt **25**: 97-106.

Gerlach, R. & Meurers-Balke, J. (2014a): Wo wurden römische Häfen am Niederrhein angelegt? Die Beispiele Colonia Ulpia Traiana (Xanten) und Burginatium (Kalkar). – In: H. Kennecke (ed.): Der Rhein als europäische Verkehrsachse. Die Römerzeit. – Bonner Beiträge zur Vor- und Frühgeschichtlichen Archäologie 16. Rheinische Friedrich-Wilhelms-Universität, pp. 199-208, Bonn.

Gerlach, R. & Meurers-Balke, J. (2014b): Der Prallhang als Standortvorteil – der römische Rhein bei Burginatium. – Archäologie Rheinland 2013: 114-117.

Glaser, R. (2012): Historische Klimatologie Mitteleuropas. Europäische Geschichte Online (EGO). URL: http://www.ieg-ego.eu/glaserr-2012-de, (24/06/2017).

Glaser, R. (2013): Klimageschichte Mitteleuropas. 1200 Jahre, Wetter, Klima, Katastrophen. – Wissenschaftliche Buchgesellschaft, pp. 272, Darmstadt.

Glaser, R. & Hagedorn, H. (1990): Die Überschwemmungskatastrophe von 1784 im Maintal. Eine Chronologie ihrer witterungsklimatischen Voraussetzungen und Auswirkungen. – Die Erde **121**: 1-14.

Glaser, R., Riemann, D., Schönbein, J., Barriendos, M., Brázdil, R., Bertolin C., Camuffo, D., Deutsch, M., Dobrovolný, P., van Engeln, A., Enzym, S., Halicková, M., Koenig, S.J., Kotyza, O., Limanówka, D., Macková, L., Sghedoni, M., Martin, B. & Himmelsbach, I. (2010): The variability of European floods since AD 1500. – Climatic Change **101**: 235-256.

Goldberg, P. & Macphail, R. I. (2006): Practical and theoretical geoarcharchaeology. Blackwell Publishing, pp. 454, Singapore.

Goldberg, P. & Aldeias, V. (2018): Why does (archaeological) micromorphology have such little traction in (geo)archaeology? – Archaeological Anthropological Science **10**: 269-278.

Goodmann, B.N. & Austin, J.A. Jr. (2015): Deterioration of Israel's Caesarea Maritima's ancient harbor linked to repeated tsunami events identified in geophysical mapping of offshore stratigraphy. – Journal of Archaeological Science: Reports **3**: 444-454.

Gouramanis, C., Switzerab, A.D., Polivka, P.M., Bristow, C.S., Jankaew, K., Dat, P.T., Pile, J., Rubin, C.M., Yingsin, L., Ildefonso, S.R. & Jole, H.M. (2015): Ground penetrating radar examination of thin tsunami beds — A case study from Phra Thong Island, Thailand. – Sedimentary Geology **329**: 14-165.

Guccione, M.J. (2008): Impact of the alluvial style on the geoarchaeology of stream valleys. – Geomorphology **101**: 378-401.

Guidoboni, E., Comastri, A. & Traina, G. (1994): Catalogue of ancient earthquakes in the Mediterranean area up to the 10th century. Volume 1. – ING-SGA, pp. 504, Bologna.

Gündel, F. (1922): Die römische Mainbrücke bei Frankfurt a.M. – Germania **6 (2)**: 68-77.

H

Hadler, H. & Vött, A. (2017): Der Handelsplatz Rungholt und seine Zerstörung durch die 1. Grote Mandrenke im Jahr 1362. Geographische Rundschau **9**: 20-25.

Hadler, H., Willershäuser, T., Ntageretzis, K., Henning, P. & Vött, A. (2012): Catalogue entries and non-entries of earthquake and tsunami events in the Ionian Sea and the Gulf of Corinth (eastern Mediterranean, Greece) and their interpretation with regard to palaeotsunami research. – In: Vött, A. & Venzke, J.-F. (eds.): Beiträge der 29. Jahrestagung des Arbeitskreises, Geographie der Meere und Küsten", 28. bis 30. April 2011 in Bremen. – Bremer Beiträge zur Geographie und Raumplanung **44**: 1-15.

Hadler, H., Baika, K., Pakkanen, J., Evangelistis, D. Fischer, P., Ntageretzis, K., Röbke, B., Willershäuser, T. & Vött, A. (2015): Palaeotsunami impact on the ancient harbour site Kyllini (western Peloponnese, Greece) based on a geomorphological multi-proxy approach. – Zeitschrift für Geomorphologie N. F., Supplementary Issue **59 (4)**: 7– 41.

Hadler, H., Vött, A., Newig. J., Emde, K., Finkler, C., Fischer, P., Willershäuser, T. (2018): Geoarchaeological evidence of marshland destruction in the area of Rungholt, present-day Wadden Sea around Hallig Südfall (North Frisia, Germany), by the Grote Mandrenke

in 1362 AD. – Quaternary International **473**: 37-54.

Hadler, H., Fischer, P., Obrocki, L., Heinzelmann, M. & Vött, A. (2019): River channel evolution and tsunami impacts recorded in local sedimentary archives – The 'FiumeMorto'atOstia Antica (Tiber River, Italy). – Sedimentology, in press. doi: https://doi.org/10.1111/sed.12599.

Harrington, G.A., Hendry & M.J. (2006): Using direct-push EC logging to delineate heterogeneity in a clay-rich aquitard. – Ground Water Monitoring & Remediation **26 (1)**: 92-100. – Sedimentology.

Harry, M.J. (2008): Ground Penetrating Radar: Theory and Applications. – Elsevier, pp.509, Amsterdam.

Hansen, J.D., Pringel, J.K. & Goodwin, J. (2014): GPR and bulk ground resistivity surveys in graveyards: locating unmarked burials in contrasting soil types. – Forensic Science International **237**: e24-e25.

Hausmann, J. (2013): Parameterisation of the Near Surface by Combined Geophysical and Direct Push Techniques in the Frame of Geotechnical Site Investigation. – Unpublished PhD Thesis. Eberhard Karls University, Tübingen.

Hausmann, J., Dietrich, P., Vienken, T. & Werban, U. (2016): Technique, analysis routines, and application of direct push-driven in situ color logging. – Environmental Earth Science **75**: 1-21.

Hausmann, J., Zielhofer, C., Werther, L., Berg-Hobohm, S., Dietrich, P., Heymann, R. & Werban, U. (2018): Direct push sensing in wetland (geo)archaeology: High-resolution reconstruction of buried canal structures (Fossa Carolina, Germany). – Quaternary International **473**: 21-36.

Hecht, S. (2007): Sedimenttomographie für die Archäologie – Geoelektrische und refraktionsseismische Erkundungen für on-site und off-site studies. – In: Wagner, G. (ed.): Einführung in die Archäometrie. – Springer, pp. 96-112, Heidelberg.

Herget, J. (2007): Die direkten Einflüsse des Menschen auf die Reliefsphäre. – Zeitschrift für Geomorphologie N.F., Supplementary Issue **148**: 42-46.

Herget, J. (2012): Am Anfang war die Sintflut. Hochwasserkatastrophen in der Geschichte. Wissenschaftliche Buchgesellschaft, pp. 160, Darmstadt.

Herget, J. (ed.) (2017): Geoarchäologie vor Ort. – Geographische Rundschau **9**: 1-58.

Herget, J., Kaplan, A., Krell, M., Rustemeier, E., Simmer, C. & Wyss, A. (2015): The millennium flood of July 1342 revisited. – Catena **130**: 82-94.

Hessische Geologische Landesanstalt (ed.) (1922): Geologische Karte Hessen, Maßstab 1:25000. Blatt 5919: Seligenstadt, Darmstadt.

Higman, B & Bourgeois, J. (2008): Deposits of the 1992 Nicaragua Tsunami. – In: T. Shiki, Y. Tsuji, T. Yamazaki & K. Minoura (eds.): Tsunamiites. – Elsevier, pp. 81-105, Amsterdam.

Hill, C.L. (2014): Rivers. Environmental archaeology. – In: Encyclopedia of Global Archaeology. Springer, pp. 6343-5351, New York.

Hoffmann, N., Master, D. & Goodman-Tschernov. B. (2018): Possible tsunami inundation identified amongst 4-5th century BCE archaeological deposits at Tel Ashkelon, Israel. – Marine Geology **396**: 150-159.

Holliday, V. T. (2001): Quaternary Geoscience. – In: Goldberg, P., Holliday, V.T. & Ferring, C.R. (eds.): Earth Science and Archaeology. – Kluwer Academic/ Plenum Publischer, pp. 3-37, New York, Boston, Dordrecht, London, Moscow.

Houlsby G.T. & Ruck, B.M. (1998): Interpretation of Signals from Acoustic Cone Penetrometer. – In: Robertson, P.K. & Mayen, PW. (eds.): Geotechnical Site Characterization. – Balkema, pp. 1075-1080, Rotterdam.

Hunter, J.A., Benjumea, B., Harris, J.B., Miller, R.D., Pullan, S.E., Burns, R.A. & Good, R.L. (2002): Surface and downhole shear wave seismic methods for thick soil site investigations. – Soil Dynamics and Earthquake Engineering **22**: 931-941.

I

Institute for Geology and Mineral Exploration (IGME) (1982): Geological map of Greece, 1:50,000, Olympia Sheet. – Athens.

J

Jones, G. (2008): Geophysical Mapping of Historic Cemeteries. – Technical Brief in Historical Archaeology **3**: 25-38.

K

Kabata-Pendias, A. (2011): Trace Elements in Soils and Plants. – CRC Press, p. 505, Boca Raton.

Kadereit, A., Dehner, U., Hansen, L., Pare, C. & Wagner, G.A. (2006): Geoarchaological studies of man-environment interaction at the Glauburg, Wetterau, Germany. – Zeitschrift für Geomorphologie, Supplement Volume **142**: 85-108.

Karkanas, P., Dabney, M. K., Angus, R., Smith, K. & Wright, J.C. (2012): The geoarchaeology of Mycenaean chamber tombs. – Journal of Archaeological Science **29**: 2722-2732.

Koppenjan, S. (2009): Ground Penetrating Radar Systems and Design. – In: Jol, H.M. (ed.): Ground Penetration Radar: Theory and Applications. – Elsevier, pp. 72-97, Amsterdam.

Katsambas, A. & Antoniou, C. (1996): Mineral water and spas in Greece. – Clinics in Dermatology **14**: 615 - 618.

Keller, R. (1979): Hydrologischer Atlas der Bundesrepublik Deutschland. – Deutsche Forschungsgemeinschaft, Bonn.

Kelletat, D. (1974): Beiträge zur regionalen Küstengeomorphologie des Mittelmeerraumes. Gargano/Italien und Peloponnes/Griechenland. – Zeitschrift für Geomorphologie, N. F., Supplementary Volume **19**: 161 pp.

Kempf, P., Moernaut, J., Van Daele, M., Vandoorne, W., Pino, M., Urrutia, R. & De Batist, M. (2017): Coastal lake sediments reveal 5500 years of tsunami history in south central Chile. – Quaternary Science Reviews **161**: 99-116.

Kirchner, A, Zielhofer, C., Werther, L., Schneider, M., Linzen, S., Wilken, D., Wunderlich, T., Rabbel, W., Meyer, C., Schmidt, J., Schneider, B., Berg-Hobohm & S., Ettel., P. (2018): A multidisciplinary approach in wetland geoarchaeology: Survey of the missing southern canal connection of the Fossa Carolina (SW Germany). – Quaternary International **473**: 3-20.

Kessler, A. (1962) Studien zur jüngeren Talgeschichte am Main und an der Mümling und über jüngere Formenentwicklung im hinteren Buntsandstein-Odenwald. – In: Kinzl, H., Kraus, Metz, T.F., Otremba, E., Schott, C. & Meynen, E. (eds.): Forschungen zur deutschen Landeskunde. – Veröffentlichungen des Zentralausschusses für deutsche Landeskunde und des Instituts für Landeskunde 33. Bundesanstalt für Landeskunde

und Raumforschung, pp. 25-33, Bad Godesberg.

Köhn, M. (1929): Korngrößenbestimmung mittels Pipettanalyse. – Tonindustrie-Zeitung **55**: 729-731.

Körber, H. (1962): Die Entwicklung des Maintals. – Würzburger Geographische Arbeiten 10, Würzburg.

Körber, R., Hornbruch, G., Leven, C., Tischer, L., Grossmann, J., Dietrich, P., Weiss, H. & Dahmke, A. (2009): Evaluation of Combined Direct-Push Methods Used for Aquifer Model Generation. – Ground Water **47**: 536-546.

Kortekaas, S. & Dawson, A.G. (2007): Distinguishing tsunami and storm deposits: An example from Martinhal, SW Portugal. – Sedimentary Geology **200**: 208-221.

Koster, K. (2016): Cone Penetration testing: A Sound Method for Urban Archaological Prospection. – Archaeological Prospection **23**: 55-69.

Koster, B. & Reicherter, K. (2014): Sedimentological and geophysical properties of a ca. 4000 year old tsunami deposit in southern Spain. – Sedimentary Geology **314**: 1-16.

Koster, B., Vött, A., Mathes-Schmidt, M. & Reicherter, K. (2015): Geoscientific investigations in search of tsunami deposits in the environs of the Agoulinitsa peatland, Kaiafas Lagoon and Kakovatos (Gulf of Kyparissia, western Peloponnese, Greece). – Zeitschrift für Geomorphologie N.F., Supplementary Issue **59 (4)**: 125-156.

Kraft, J.C., Rapp, G., Gifford, J.A. & Aschenbrenner, S.E. (2005): Coastal change and archaeological settings in Elis. – Hesperia **74 (1)**: 1-39.

Kurup, P., Sullivan, C., Hannagan, R., Yu, S., Azimi. H., Roberton, S., Ryan, D., Nagarajan, R., Ponrathnam, T. & Howe, G. (2017): A Review of Technologies for Characterization of Heavy Metal Contaminants. – Indian Geotechnical Journal **47**: 421-436.

Kwamme, K.L. (2001): Current Practices in Archaeogeophysics: Magnetics, Resistivity, Conductivity, and Grouund-Penetrating Radar. – In: Goldberg, P., Holliday, V.T. & Ferring, C.R. (eds.): Earth Science and Archaeology. – Kluwer Academic/ Plenum Publischer, pp.353-384, New York, Boston, Dordrecht, London, Moscow.

L

Lafuerza, S., Canals, M., Casamor, J.L. & Devincenzi, J.M. (2005): Characterization of deltaic sediment bodies based on in situ CPT/CPTU profiles: A case study on the Llobregat delta plain, Barcelona, Spain. – Marine Geology **222-223**: 497-510.

Landva, A.O., Korpijaakkoo, E.O. & Pheeney, P.E. (1983): Geotechnical classification of peats and organic soils. – In: Jarrett, O.M. (ed.): Testing of Peats and Organic Soil. – American Society for Testing and Materials, ASTM STP 20: pp. 37-51.

Lang, F. (2002): Klassische Archöologie. Eine Einführung in Methode, Theorie und Praxis. – A. Francke Verlag, pp. 333, Tübingen, Basel.

Leser, H. (2009): Geomorphologie. – Westermann, pp. 400, Braunschweig.

Lessoff, S.C., Schneidewind, U., Leven, C., Blum, P., Dietrich, P. & Dagan, G. (2010): Spatial characterization of the hydraulic conductivity using direct-push injection logging. Water Resources Research **46**: 1-9.

Leven, C., Weiss, H., Vienken, T. & Dietrich, P. (2011) Direct-Push-Technologien – Effiziente Untersuchungsmethoden für die Untergrunderkundung. – Grundwasser – Zeitschrift der Fachsektion Hydrologie **16**: 221-234.

Loke, M. H., Mcworth, I. & Dahlin, T. (2003): A comparison of smooth and blocky inversion methods in 2D electrical imaging surveys. – Exploration Geophysics **34**: 182-187.

Loke, M.H. (2012): Tutorials: 2D and 3D electrical imaging surveys. University Sains Malaysia. Pengang, Malaysia. – Unpublished revised course notes.

Long, M. & Boyland, N. (2012): In-situ testing of peat – a review and update on recent developments. – Geotechnical Engineering Journal **43**: 41-55.

Lunne, T., Robertson, P.K. & Powell, J.J.M. (2002): Cone Penetration Testing in Geotechnical Practice. – Taylor and Francis Group, pp. 312, London, New York.

M

Malagodi, S., Orlando, L., Piro, S. & Rosso, F. (1996): Location of Archaeological Structures using GPR Method: Three-dimensional Data Acquisition and Radar Signal Processing. – Archaeological Prospection **3**: 13-23.

Maliva, R.G. (2016): Direct-Push Technology. – In: Maliva, R.G. (ed.): Aquifer Characterization Techniques. Schlumberger Methods in Water Resources Evaluation Series No. 4. – Springer, pp. 383-402, Berlin, Heidelberg.

Mason, J., Reicherter, K. & Papanikolaou, I. (2015): The Lapithas Mountain faults and nearby archaeological damage, western Peloponnese, Greece. – Zeitschrift für Geomorphologie N.F., Supplementary Issue **59 (4)**: 189-213.

McCall, W. (2011): Application of Geoprobe HPT Logging System for geo-environmental investigations. – Geoprobe Technical Bulletin MK **3184**: 1-36.

McCall, W. & Christy, T.M. (2010): Development of hydraulic conductivity estimate for the hydraulic profiling tool. – Paper presented at the 2010 North American Environmental Field Conference & Exposition. Conference Program with Abstracts. Las Cruces, New Mexico: The Nielsen Environmental Field School.

McCall, W., Christy, T.M., Pipp, D., Terkelsen. M., Christensen, A., Weber, K. & Engelsen, P. (2014): Field application of combined membrane-interface probe and hydraulic profiling tool (MiHpt). – Groundwater Monitoring & Remediation **34**: 85-95.

McClusky, S., Balassanian, S., Barka, A., Demir, C., Ergintav, S., Georgiev, I., Gurkan, O., Hamburger, M., Hurst, K., Kahle, H., Kastens, K., Kekelidze, K., King, R., Kotzev, V., Lenk, O., Mahmoud, S., Mishin, A., Nadariya, M., Ouzounis, A., Paradissis, D., Peter, Y., Prilepin, M., Reilinger, R., Sanli, I., Seeger, H., Tealeb, A., Toksoz, M.N. & Veis, G. (2000): Global Positioning System Constraints on Plate Kinematics and Dynamics in the Eastern Mediterranean and Caucasus. – Journal of Geophysical Research, Solid Earth **105**: 5695-5719.

Mee, C.B. & Cavanagh, W.G. (1984): Mycenaen tombs as evidence for social and political organization. – Oxford Journal of Archaeology **3 (3)**: 45-64.

MEIER, D. (2011): Die Schäden der Weihnachtsflut von 1717 an der Nordseeküste Schleswig-Holsteins. – Die Küste **78**: 259–292.

Menge, P. & van Impe, W. (1995): The application of acoustic emission testing with penetration testing. Proceedings of the International Symposium on Cone Penetration testing, CPT '95. – Swedish Geotechnical Society: 49-54.

Meyers, S.R. (2014): Astrochron: a R Package for Astrochronology Version 0.6.5.

Milkereit, B. & Spencer, C. (1989): Noise suppression and coherency enhancement of seismic data. – In: Agterberg, F.P. & Bonham-Carter, G.F. (eds.): Statistical application in the

Earth Sciences. – Geological Survey of Canada **89 (9)**, pp. 243-248, Ottawa.

Minoura, K. & Nakaya, S. (1991): Traces of Tsunami Preserved in Inter-Tidal lacustrine and Marsh Deposits: Some Examples from Northeast Japan. – The Journal of Geology **99**: 265-287.

Mischke, S., Rajabov, I., Mustaeva, N., Zhang, C., Herzschuh, U., Boomer, I., Brown, E.T., Anderson, N., Myrbo, A., Ito, E. & Schudack, M.E. (2010): Modern hydrology and late Holocene history of Lake Karakul, eastern Pamirs (Tajikistan): A reconnaissance study. – Palaeogeography, Palaeoclimatology, Palaeoecology **289**: 10-24.

Missiaen, T., Verhegge, J., Heirman, K. & Crombé, P. (2015): Potential of cone penetration testing for mapping deeply buried palaeolandscapes in the context of archaeological surveys in polders. – Journal of Archaeological Science **55**: 147- 187.

Missiaen, T., Evangelinos, D., Claerhout, C., De Clercq, M., Pieters, M., Demerre, I. (2018): Archaeological prospection of the nearshore and intertidal area using ultra-high resolutionmarine acoustic techniques: Results from a test study on the Belgian coast at Ostend-Raversijde. – Geoarchaeology **33 (3)**: 386-340.

Moore, L.M, McAdoo, B.G. & Ruffman, A. (2007): Landward fining from multiple sources in a sand sheet deposited by the 1929 Grand Banks tsunami, Newfoundland. – Sedimentary Geology **200**: 336-346.

Morley, M.W. & Goldberg, P. (2017): Geoarchaeological research in the humid tropics: A global perspective. – Journal of Archaeological Science: **77**: 1-9.

Morton, R.A., Gelfenbaum, G. & Jaffe, B.E. (2007): Physical criteria for distinguishing sandy tsunami and storm deposits using modern examples. – Sedimentary Geology **200**: 184-207.

N

Nero, C., Acheampong Aning, A.A., Danuor, S.K., Noye, R. M. (2016): Delineation of graves using electrical resistivity tomography. – Journal of Applied Geophysics **126**: 138-147.

Neuhauser, K.R. (2009): An electrical resistivity survey of a small private cemetery, Lincoln County, Kansas, Texas. – Transactions of the Kansas Academy of Science **112 (1/2)**: 15-21.

Nikolentzos, K. (2011). Μυκηναϊκή Ηλεία: Πολιτική και Πολιτιστική Εξέλιξη, Εθνολογικά Δεδομένα και Προβλήματα. – Athens.

Noll, F.C. (1866): Der Main in seinem unteren Laufe: Physikalische und naturhistorische Verhältnisse dieses Flusses. – Hansebooks, Frankfurt am Main.

Ntageretzis, K., Vött, A., Fischer, P., Hadler, H., Emde, K., Röbke, B.R. & Willershäuser, T. (2015a): Traces of repeated tsunami landfall in the vicinity of Limnothalassa Moustou (Gulf of Argolis – Peloponnese, Greece). – Zeitschrift für Geomorphologie N.F., Supplementary Issue **59 (4)**: 301-317.

Ntageretzis, K., Vött, A., Fischer, P., Hadler, H., Emde, K., Röbke, B.R. & Willershäuser, T. (2015b): Palaeotsunami history of the Elos plain (Evrotas River delta, Peloponnese, Greece). – Zeitschrift für Geomorphologie N.F., Supplementary Issue **59 (4)**: 253-273.

Ntageretzis, K., Vött, A., Emde, K., Fischer, P., Hadler, H., Röbke, B.R. & Willershäuser, T. (2015c): Palaeotsunami record in near-coast sedimentary archives in southeastern Lakonia (Peloponnese, Greece). – Zeitschrift für Geomorphologie N.F., Supplementary Issue **59 (4)**: 275-299.

O

Obrocki, L., Becker, T., Mückenberger, K., Finkler, C., Fischer, P., Willershäuser, T., Vött, A. (2018a): Landscape reconstruction and major flood events of the River Main (Hesse, Germany) in the environs of the Roman fort at Großkrotzenburg. – Quaternary International, in press: 1-16. doi: htpps://doi.org/10-1016/j.quaint.2018.08.009.

Obrocki, L., Vött, A., Wilken, D., Fischer, P., Willershäuser T., Koster, B., Lang, F., Papanikolaou, I., Rabbel, W., Reicherter, K. (2018b): Tracing tsunami signatures of the AD 551 and AD 1303 tsunamis at the Gulf of Kyparissia (Peloponnese, Greece) using Direct Push in situ sensing techniques combined with geophysical studies. – Sedimentology, in press: 1-35. doi: 10.1111/sed.12555.

Obrocki, L., Eder, B., Gehrke, H.-J., Lang, F., Vött, A., Willershäuser, T., Rusch, K., Wilken, D., Hatzi-Spiliopoulou, G., Kolia, E.-I., Vikatou, O. (2019): Detection and localization of chamber tombs in the environs of ancient Olympia (Peloponnese, Greece) based on a combination of archaeological survey and geophysical prospection. – Geoarchaeology, in press: 1-13. doi: 10.1002/gea.21724.

Orlando, L. (2013): GPR to constrain ERT data inversion in cavity searching: Theoretical and practical applications in archaeology. – Journal of applied Geophysics **89**: 35-47.

P

Paasche, H., Werban, U. & Dietrich, P. (2009): Near-surface seismic traveltime tomography using a direct push source and surface geophones. – Geophysics **74 (4)**: G17-G25.

Pantazis, T. (2010): The use and application of handheld and portable XRF spectrometers. – X-Ray Spectrometry **39 (2)**: 90-97.

Papadopoulos, G.A., Gràcia, E., Urgeles, R., Sallares, V., De Martini, P.M., Pantosti, D., González, M., Yalciner, A.C., Mascle, J., Sakellariou, D., Salomon, A., Tinti, S., Karastathis, V., Fokaefs, A., Camerlenghi, A., Novikova, T. & Papageorgiou, A. (2014a): Historical and pre-historical tsunamis in the Mediterranean and its connected seas: Geological signatures, generation mechanism and coastal impacts. – Marine Geology **354**: 81-309.

Papadopoulos, G.A., Daskalaki, E., Fokaefs, A. & Novikova, T. (2014b): Tsunamigenic potential of local and distant tsunami sources threatening SW Peloponnese. – Bolletino di Geofisica Teorica ed Applicata **55**: 389-404.

Papadopoulos, N.G., Yi, M.-J., Kim, J.-H., Tsourlos, P. & Tsokas, G.N. (2010): Geophysical investigation of tumuli by means of surface 3D Electrical Resistivity Tomography. – Journal of Applied Geophysics **70**: 192-205.

Papanikolaou, D., Fountoulis, I. & Metaxas, C. (2007): Active faults, deformations rates and Quaternary palaeogeography at Kyparissiakos Gulf (SW Greece) deduced from onshore and offshore data. – Quaternary International **171-172**: 14-30.

Papazachos, B.C. & Dimitriu, P.P. (1991): Tsunamis In and Near Greece and Their Relation to the Earthquake Focal Mechanisms. – Natural Hazards **4**: 161-170.

Papoulia, J., Nicolich, R., Makris, J., Mascle, J., Papadopouloa, G., Anagnostou, Ch., Camera, L., Daskalaki, E., Faskoulaka, Ch., Fokaefs, A., Fountoulis, I., Garcia, J., Gülkan, P., Mariolakos, I., Pomonis, A., Santulin, M., Tsambas, A., Warell, N. & Yalciner, A. (2014): A new seismogenic model for the Kyparissiakos Gulf and western Peloponnese (SW Hellenic Arc). – Bollettino di Geofisica Teorica ed Applicata **55**: 405-432.

Peters, R. & Jaffe, B. (2010): Identification of tsunami deposits in the geologic record;

developing criteria using recent tsunami deposits. – U.S. Geological Survey Open-File Report 2010-1239, pp. 39.

Pfister, C. (1999): Wetternachhersage. 500 Jahre Klimavariationen und Naturkatastrophen (1496-1995). – Hauptverlag, pp. 304, Bern, Stuttgart.

Pillay, T.V.R. (1966): A preliminary survey of the lagoon fisheries of the western Peloponnesus, Greece, September 1964. - Economic survey of the western Peloponnesus, Greece. – FAO Fishery Circular **108 (3)**: 207-224.

Putiška, R., Sabol, M., Kušnirák, D. & Dostál, I. (2016): Geophysical Research at the Prepoštská Cave and Čertova Pec Cave Neanderthal Sites (Western Slovakia). – Archaological Prospection **24**: 119-131.

Q

R

R Core Team (2014) R: A Language and Environment for Statistical Computing. – R Foundation for Statistical Computing, Vienna, Vienna.

Rabbel, W. (2006): Seismic methods. – In: Kirsch, R. (ed.): Groundwater Geophysics. – Springer, pp. 23-84, Berlin, Heidelberg.

Rabbel, W., Erkul, E., Stümpel, H., Wunderlich, T., Pasteka, R., Papco, J., Niewöhner, P., Baris, S., Cakin, O. & Peksen, E. (2015): Discovery of a Byzantine Church in Iynik/Nicaea, Turkey: an Educational Case Hostory of Geophysical Prospecting with Combined Methods in Urban Areas. – Archaeological Prospection **22**: 1-20.

Rabbel, W., Müller, C., Wilken, D., Berndt, C. (2016): Shallow 3D Reflection Seismic. – In: Beer M., Kougioumtzoglou I., Patelli E., Au IK. (eds): Encyclopedia of Earthquake Engineering. – Springer, Berlin, Heidelberg.

Rapp, Jr & Hill, C. L. (1998): Geoarchaeology. The Earth-Science Approach to Archaeology Interpretation. – Yale University Press, pp. 274, New Haven, London.

Raška, P., Emmer, A. (2014): The 1916 catastrophic flood following the Bílía desná dam failure: the role of historical data sources in the reconstruction of its geomorphologic and landscape effect. – Geomorphology **226**: 135-147.

Reimer, P.J., Bard, E., Bayliss, A., Beck, J.W., Blackwell, P.G., Ramsey, C.B., Buck, C.E., Cheng, H., Edwards, R.L., Friedrich, M., Grootes, P.M., Guilderson, T.P., Haflidason, H., Hajdas, I., Hatté, C., Heaton, T.J., Hoffmann, D.L., Hogg, A.G., Hughen, K.A., Kaiser, K.F., Kromer, B., Manning, S.W., Niu, M., Reimer, R.W., Richards, D.A., Scott, E.M., Southon, J.R., Staff, R.A., Turney, C.S.M., von der Pflicht, J. (2013): Intcal13 and Marine 13 radiocarbon age calibration curves 0-50,000 years cal BP. – Radiocarbon **55 (4)**: 1869-1887.

Reineck, H.R. & Singh, I-B. (1980): Depositional sedimentary environments. Springer, pp. 442, Berlin, Heidelberg.

Richter, T.O., van der Gaast, S., Koster, B., Vaars, A., Gieles, R., de Stigter, H.C., De Haas, H. & van Weering, T.C.E. (2006): The Avaatech XRF Core Scanner: technical description and applications to NE Atlantic sediments. – Geological Society **267**: 39-50.

Robertson, P.K., Campanella, R.G., Gillespie, D. & Rice, A. (1986): Seismic Cpt to Measure in Situ Shear Wave Velocity. – Journal of Geotechnical Engineering **122**: 791-803.

Robertson, P.K. (1990): Soil classification using the cone penetration test. – Canadian Geotechnical Journal **27**: 151-158.

Robertson, P.K. (2009): Interpretation of cone penetration tests – a unified approach. – Canadian Geotechnical Journal **46**: 1337-1355.

Robertson, P.K. (2016): Cone penetration test (CPT)-based soil behaviour type (SBT) classification system – an update. – Canadian Geotechnical Journal **53**: 1910-1927.

Röbke, B.R. & Vött, A. (2017): The tsunami phenomenon. – Progress in Oceanography **159**: 296-322.

Röbke, B.R., Schüttrumpf, H., Wöffler, T., Hadler, H., Willershäuser, T. & Vött, A. (2012): Tsunamis in the Gulf of Kyparissia (western Peloponnese, Greece) – risk assessment based on numeric simulation and field evidence. – In: Schüttrumpf, H. & Tomasicchio, R. (eds.): Proceedings of the 5th International Short Conference on Applied Coastal Research, 6th to 9th June, 2011. – Shaker, Aachen, pp. 560-569.

Röbke, B.R., Schüttrumpf, H., Theide Wöf, F., Fischer, P., Hadler, H., Ntageretzis, K., Willershäuser, T. & Vött, A. (2013): Tsunami inundation scenarios for the Gulf of Kyparissia (western Peloponnese, Greece) derived from numerical simulations and geoscientific field evidence. – Zeitschrift für Geomorphologie, N. F., Supplementary Issue **57 (4)**: 69 –104.

Röbke, B.R., Vött, A., Willershäuser, T., Fischer, P. & Hadler, H. (2015): Considering coastal palaeogeographical changes in a numerical tsunami model – a progressive base to compare simulation results with field traces from three coastal settings in western Greece. Zeitschrift für Geomorphologie N.F., Supplementary Issue, **59(4)**: 157-188.

Röbke, B.R., Schüttrumpf, H. & Vött, A. (2016): Effects of different boundary conditions and palaeotopographies on the onshore response of tsunamis in a numerical model – A case study from western Greece. – Continental Shelf Research **124**: 182-199.

Röbke, B.R., Schüttrumpf, H. & Vött, A. (2017): The Tsunami phenomenon. – Progress in Oceanography **159**: 296-322.

Roggenkamp, T. (2016): Der Rhein zur Römerzeit - Wasserstände und Abflüsse des Mittel- und Niederrheins. – Forschungen zur deutschen Landeskunde 264.

Roggenkamp, T. & Herget, J. (2014): Rekonstruktion römerzeitlicher Wasserstände und Abflüsse an Nieder- und Mittelrhein. – In: Bemmann, J., Brosseder & U. Joachim, H.-E. (eds.): Der Rhein als europäische Verkehrsachse. – Bonner Beiträge zur Vor- und frühgeschichtlichen Archäologie 16. Rheinische Friedrich-Wilhelms-Universität, pp. 25-63, Bonn.

S

Sachpazi, M., Hirn, A., Clément, C., Haslinger, F., Laigle, M., Kissling, E., Charvis, P., Hello, Y., Léppine, J.C., Spin, M. & Andorge, J. (2000): Western Hellenic subduction and Cephalonia Transform: local earthquakes and plate transport and strain. Tectonophysics **319**: 301-319.

Sageman, B.B., Lyons, T.W. & Joo, Y.Ji. (2013): Geochemistry of fine-grained, organic carbon-rich facies. In: Holland, H. & Turekian, K. (eds.), Treatise on geochemistry. Elsevier, pp. 141-179, Amsterdam.

Sarris, A., Kalayci, T., Moffat, I. & Manataki, M. (2017): An Introduction to Geophysical and Geochemical Methods in Digital Geoarchaeology. – In: Siart C., Forbriger M. & Bubenzer O. (eds.): Digital Geoarchaeology. Natural Science in Archaeology. – Springer, pp. 215-236, Cham.

Scheffers, A., Kelletat, D., Vött, A., May, S.M. & Scheffers, S. (2008): Late Holocene tsunami

traces on the western and southern coastlines of the Peloponnesus (Greece). – Earth Planetary Science Letters **269**: 271-279.

Scheinost, A.C & Schwertmann, U. (1999): Color identification of iron oxides and hydroxysulfates: use and limitations. – Soil Science Society of America Journal **63**: 1463-1471.

Schirmer, W. (1983): Die Talentwicklung an Main und Regnitz seit dem Hochwürm. – Geologisches Jahrbuch **A17**: 11-43.

Scheffer, N.A., Rico, M., Enzel, Y., Benito, G. & Grodek, T. (2014): The Palaeoflood record of the Gardon River, France: A comparison with the extreme 2002 flood event. – Geomorphology **98**: 71-83.

Schmelzbach, C., Tronicke, J. & Dietrich, P. (2011): Three-dimensional hydrostratigraphic models from ground-penetrating radar and direct-push data. – Journal of Hydrology **398**: 235- 245.

Schneeweiss, J. & Schatz, T. (2014): The impact of landscape change on the significance of political centers along the lower Elbe River in the 10th century A.D. – Quaternary International **324**: 20-33.

Schön, J.G. (2015): Physical properties of rocks: fundamentals and principles of petrophysics. Elsevier, pp. 512, Amsterdam.

Schreiner, M. & Kreysing, K. (1998): Geotechnik Hydrologie. – Springer, pp. 567, Berlin, Heidelberg, New York.

Schröder, B. & Hauptmann, A. (2008): Geoarchäologie. – In: Hauptmann, A. & Pingel, V. (eds.): Archäometrie. Methoden und Anwendungsbeispiele. – Schweizerbart'sche Vergalsbuchhandlung, pp. 183-200, Altenburg.

Schrott, L. & Hecht, S. (2007): Potenziale geophysikalischer Methoden in der Geomorphologie. – Zeitschrift für Geomorphologie N.F., Supplementary Issue **148**: 110-116.

Schrott, L., & Sass, O. (2008): Application of field geophysics in geomorphology: Advances and limitations exemplified by case studies. – Geomorphology **93**: 55-73.

Schüssler, C. (2004): Hochwasser und Überschwemmungen – Leben mit dem Main. – In: Rebentisch, D. & Hils-Brockhoff, E. (eds.): Stadt am Fluß – Frankfurt und der Main. – Archiv für Frankfurts Geschichte und Kunst, pp. 167-183, Frankfurt am Main.

Schulmeister, M.K., Butler Jr., J.J., Healey, J.M., Zheng, L., Wysocki, D.A. & McCall, G.W. (2003): Direct-push electrical conductivity logging for high-resolution hydrostratigraphic characterization. – Ground Water Monitoring & Remediation **23 (3)**: 52-62.

Sellwood, S., Healey, J.M., Birk, S. & Butler Jr, J.J. (2005): Direct-Push Hydrostratigraphic Profiling: Coupling Electrical Logging and Slug Test. – Ground Water **43**: 19-29.

Shabaan, F.A., Abbas, A.M., Atya, M.A. & Hafez, M.A. (2009): Ground-penetrating Radar Exploration for Ancient Monuments in the Valley of Mummies –Kilo 6, Bahariya Oasis, Egypt. – Journal of Applied Geophysics **68**: 194-202.

Shahack-Gross, R. (2017): Archeological formation theory and geoarchaeology: State-of-the-art in 2016. – Journal of Archaeological Science **79**: 36-43.

Shaw, B., Ambraseys, N.N., England, P.C., Floyd, M.A., Gorman, G.J., Higham, T.F.G., Jackson, J.A., Nocquet, J.-M., Pain, C.C. & Piggott, M.D. (2008): Eastern Mediterranean tectonics and tsunami hazard inferred from the AD 365 earthquake. – Natural Geoscience **1**: 268 – 276.

Sheriff, R.E. & Geldart, L.P. (1999): Exploration Seismology. Cambridge University Press, pp.

628, Cambridge.

Slejko, D., Santulin. M. & Garcia, J. (2014): Seismic hazard estimates for the area of Pylos and surrounding region (SW Peloponnese) for seismic and tsunami risk assessment. – Bolletino di Geofisica Teorica ed Applicata **55**: 433-468.

Sober, E. (1981): The Principle of Parisimony. The British Journal for the Philosophy of Science **32 (2)**: 145-146.

Soloviev, S.L. (1990): Tsunamigenic Zones in the Mediterranean Sea. Natural Hazard **3**: 183-201.

Soloviev, S.L., Solovieva, O.N., Go, C.N., Kim, K.S. & Shchetnikov, N.A. (2000): Tsunamis in the Mediterranean Sea 2000 B.C. – 2000 A.D. – Kluwer, pp. 237, Dordrecht.

Späth, H. (1979): Hydrogeographie. – In: Bayrisches Landesamt für Wasserwirtschaft (ed.): Das Mainprojekt. – Schriftreihe des Bayrischen Landesamtes für Wasserwirtschaft 7, pp. 31-33.

Stade, K. (1933): Die Mainlinie von Seligenstadt bis Miltenberg mit einem Nachtrage zur Abt. B Nr. 33 Kastell Stockstadt. – Der obergermanisch-Raetische Limes des Römerreiches, Heidelberg.

Starkel, L. (2002): Change in the frequency of extreme events as the indicator of climatic change in the Holocene (in fluvial systems). – Quaternary International **91 (1)**: 25-32.

Steidl, B. (2008): Welterbe Limes. Roms Grenze am Main. Mit Beiträgen von Ludwig Wamser und Horst Zimmerhackl. – In: Wamser, L. (ed.): Ausstellungskataloge der Archäologischen Staatssammlung 36. – Logo Verlag Eric Erfurth, pp. 79-123, Obernburg am Main.

Stein, J.K. (2001): A review of site formation processes and their relevance to geoarchaeology. – In: Goldberg, P., Holliday, V.T. & Ferring, C.R. (eds.): Earth Science and Archaeology. – Kluwer Academic/ Plenum Publischer, pp. 37-51, New York, Boston, Dordrecht, London, Moscow.

Styllas, M. (2014): A simple approach to define Holocene sequence stratigraphy using borehole and cone penetration test data. – Sedimentology **61**: 444-460.

Switzer, A.D. & Jones, B.G. (2008): Large-scale washover sedimentation in a freshwater lagoon from the southeast Australian coast: sea-level change, tsunami or exceptionally large storm?. – The Holocene **18**: 787– 803.

Szczucinski, W., Rachelewicz, G., Chaimanee, N., Saisuttichai, D., Tepsuwan, T. & Lorenc, S. (2012): 26 December 2004 tsunami deposits left in areas of various tsunami runup in coastal zone of Thailand. – Earth Plantes Space **64**: 843-858.

T

Tonkov, N. & Loke, M.H. (2006): A resistivity survey of a burial mound in the „Valley of the Thracian Kings“. – Archaeological Prospection **13**: 129-136.

Toonen, W.H.J., Winkels, T.G., Cohen, K.M., Prins, M.A. & Middelkoop, H. (2015): Lower Rhine historical flood magnitudes of the last 450 years reproduced from grain-size measurements of flood deposits using End Member Modelling. – Catena **130**: 69-81.

Tringale, P.T. & Mitchell, J.K. (1982): An acoustic cone penetrometer for site characterization. – Proceedings of the 2nd European Symposium on Penetration Testing, ESOPT-II: 9-14.

Tselentis, G.-A., Stavrakakis, G., Sokos, E., Gkika, F. & Serpetsidaki, A. (2010): Tsunami hazard

assessment in the Ionian Sea due to potential tsunamigenic sources - results from numerical simulations. – Natural Hazards and Earth System Sciences **10**: 1021-1030.

Tsokas, G.N., Panagiotis, I.T., Kim, J.-H., Yi, M.-J., Vargemezis, G., Lefantzis, M., Fikos, E. & Peristeri, K. (2018): ERT imaging of the interior of the tumulus of Kastas in Amphipolis (northern Greece). – Archaeological Prospection: 1-15, doi: 10.1002/arp.1718.

Turner, J.N., Jones, A.F., Brewer, P.A., Macklin, M.G. & Rasnner, S.M. (2015): Micro-XRF application in fluvial sedimentary environments of Britain and Ireland: progress and prospects. – In: Croudace, I.W. & Rothwell, R.G. (eds.): Micro-XRF studies of sediment cores. Applications of non-destructive tool for the environmental sciences. – Springer, pp. 227-267, Dordrecht, Heidelberg, London, New York.

U

Ullrich, B., Meyer, C. & Weller, A. (2007): Geoelektrik und Georadar in der archäologischen forschung: geophysikalische 3D-Untersuchungen in Munigua (Spanien). – In: Wagner, G. (ed.): Einführung in die Archäometrie. – Springer, pp. 76-95, Heidelberg.

Ulvrova, M., Paris, R., Nomikou, P., Kelfoun, K., Leibrandt, S., Tappin, D.R. & McCoy, F.W. (2016): Source of the tsunami generated by the 1650 AD eruption of Kolumbo submarine volcano (Aegean Sea, Greece). – Journal of Volcanology and Geothermal Research **321**: 125-139.

V

van Dinter, M., Cohen, K.M., Hoek, W.Z., Stouthamer, E., Jansma, E. & Middelkoop, H. (2017): Late Holocene lowland fluvial archives and geoarchaeology: Utrecht´s case study of Rhine river abandonment under Roman and Medieval settlement. – Quaternary Science Reviews **166**: 227-265.

van Dam, R.L. (2012): Landform characterization using geophysics – Recemt advances, applications, and emerging tools. – Geomorphology **137**: 57-73.

Van Dam, R.L. & Schlager, W. (2000): Identifying causes of ground-penetrating radar reflections using time-domain reflectometry and sedimentological analyses. – Sedimentology **47**: 435-339.

van Lanen, R.J. & Pierik, H.J. (2019): Calculating connectivity patterns in delta landscapes: Modelling Roman and early-medieval route networks and their stability in dynamic lowlands. – Quaternary International **501 (B)**: 393-412.

Vikatou, O. (2012a): Olympia und sein Umfeld während der mykenischen Zeit. – In: Heilmeyer, W.-D., Kaltsas, N., Gehrke, H.-J., Hatzi, G.E. & Bocher, S. (eds.): Mythos Olympia. Kult und Spiele. – Ausstellung Berlin 32. August 2012 bis 7. Januar 2013, pp. 69-73, Munich, London, New York.

Vikatou, O. (2012b): Olympia Katalog I – Das Heiligtum, sein Umfeld und seine historische Einbindung. – In: Heilmeyer, W.-D., Kaltsas, N., Gehrke, H.-J., Hatzi, G.E. & Bocher, S. (eds.): Mythos Olympia. Kult und Spiele. – Ausstellung Berlin 32. August 2012 bis 7. Januar 2013, pp. 293-331, Munich, London, New York.

Vikatou, O. (2012c): και «Ηλεία- από τον Πηνειό έως τον Αλφειό, Προϊστορικοί χρόνοι» στην Αρχαιολογία-Πελοπόννησος, pp. 374-377.

Vikatou, O. (2012d): Ηλεία. Ιστορικό και αρχαιολογικό περίγραμμα – Προϊστορικοί Χρόνοι» στην Αρχαιολογία-Πελοπόννησος, pp. 362-367.

Vikatou, O. (2013): Olympia and its Surroundings during the Mycenaean Period. στον τόμο Olimpics, Past and Present· – Qatar, pp· 38-43·

Vikatou, O. & Jung, R. (2018): Táfoi Mykinaíon Polemistón ston Mágeira Olympías, sto «Ta Nekrotafeía: Chorotaxikí orgánosi-Tafiká éthima, Teletourgíes». – In: Kountouri, E. & Gadolou, A. (eds.): Ta apotelésmata ton sostikón erevnón tis Archaiologikís Ypiresías. – TAPA, in press.

Vienken, T., Leven, C. & Dietrich, P. (2012): Use of CPT and other direct push methods for (hydro-) stratigraphic aquifer characterization – a field study. – Canadian Geotechnical Journal **49**: 197-206.

Viglione, A. & Rogger, M. (2015): Flood processes and hazards. – In: Shroder, J.F., Paron, P. & Di Baldassarre, G. (ed.): Hydro-Meteorological Hazards, Risks, and Disasters. – Elsevier, pp. 3-35, Amsterdam.

Viscarra Rossel, R.A., Minasny, B., Roudier, P. & McBratney, A.B. (2006): Colour space models for soil science. – Geoderma **133**: 320-337.

Vött, A. (2013): Neue geoarchäologische Untersuchungen zur Verschüttung Olympias. Eine Einführung in die Olympia-Tsunami-Hypothese (OTH). – 23. Trierer Winckelmannsprogramm 2011, Harrassowitz-Verlag, pp. 51, Wiesbaden.

Vött, A., Handle, M- & Brückner, H. (2002): Rekonstruktion holozäner Umweltbedingungen in Akarnanien (Nordwestgriechenland) mittels Diskriminanzanalyse von geochemischen Daten. – Geologica et Palaeontologica **36**: 123-147.

Vött, A., Brückner, H., Handle, M. & Schriever, A. (2006): Holocene palaeogeographies and the geoarchaological setting of the Mythicas coastal plain (Akarnania, NW Greece). – Zeitschrift für Geomorphologie, Supplement Volume **142**: 63-83.

Vött, A. & Kelletat, D. (2015): Holocene palaeotsunami landfalls and neotectonic dynamics in the western and southern Peloponnese. – Zeitschrift für Geomorphologie N.F., Supplementary Issue **59 (4)**: 1-5.

Vött, A., Brückner, H., May, S.M., Sakellariou, D., Nelle, O., Lang, F., Kapsimalis, V., Jahns, S., Herd, R., Handl, M. & Fountoulis, I. (2009a): The Lake Voulkaria (Akarnania, NW Greece) palaeoenvironmental archive – a sediment trap for multiple tsunami impact since the mid-Holocene. – Zeitschrift für Geomorphologie N.F., Suppl. Issue **53**: 1-37.

Vött, A., Brückner, H., Brockmüller, S., Handl, M., May, S.M., Gaki-Papanastassiou, K., Herd, R., Lang, F., Maroukian, H., Nelle, O. & Papanastassiou, D. (2009b): Traces of Holocene tsunamis across the Sound of Lefkada, NW Greece. – Global and Planetary Change **66**: 112 –128.

Vött, A., Lang, F., Brückner, H., Gaki-Papanastassiou, K., Maroukian, H., Papanastassiou, D., Giannikos, A., Hadler, H., Handl, M., Ntageretzis, K., Willershäuser, T. & Zander, A. (2011a): Sedimentological and geoarchaeological evidence of multiple tsunamigenic imprint on the Bay of Palairos-Pogonia (Akarnania, NW Greece). – Quaternary International **242**: 213-239.

Vött, A., Bareth, G., Brückner, H., Lang, F., Sakellariou, D., Hadler, H., Ntageretzis, K. & Willershäuser, T. (2011b): Olympia's harbour site Pheia (Elis, western Peloponnese, Greece) destroyed by tsunami impact. – Die Erde **142**: 259-288.

Vött, A., Fischer, P., Röbke, B.R., Werner, V., Emde, K., Finkler, C., Hadler, H., Handl, M., Ntageretzis, K. & Willershäuser, T. (2015): Holocene fan alluviation and terrace formation by repeated tsunami passage at Epitalio near Olympia (Alpheios River valley, Greece). – Zeitschrift für Geomorphologie N.F., Supplementary Issue **59 (4)**: 81-123.

Vött, A., Willershäuser, T. Röbke, B.R., Obrocki, L., Fischer, P., Hadler, H., Emde, K., Eder,

B., Gehrke, H.-J. & Lang, F. (2018a): Major flood events recorded in the Holocene sedimentary sequence of the uplifted Ladiko and Makrisia basins near ancient Olympia (western Pel-oponnese, Greece). – Zeitschrift für Geomorphologie N.F. Suppl. Issue, **62 (2)**, doi: https://doi.org/10.1127/zfg_suppl/2018/0499.

Vött, A., Bruins, H.J., Gawehn, M., Goodman-Tchernov, B.N., De Martini, P.M., Kelletat, D., Mastronuzzi, G., Reicherter, K., Röbke, B.R., Scheffers, A., Willershäuser, T., Avramidis, P., Bellanova, P., Costa, P.J.M., Finkler, C., Hadler, H., Koster, B., Lario, J., Reinhardt, E., Mathes-Schmidt, M., Ntageretzis, K., Pantosti, D., Papanikolaou, I., Sansò, P., Scicchitano, G., Smedile, A. & Szczuciński, W. (2018b): Publicity waves based on manipulated geoscientific data suggesting climatic trigger for majority of tsunami findings in the Mediterranean – Response to 'Tsunamis in the geological record: Making waves with a cautionary tale from the Mediterranean' by Marriner et al. (2017). – Zeitschrift für Geomorphologie N.F., Supplementary Issue, in press, doi: 10.1127/zfg_suppl/2018/0547.

Vött, A-, Hadler, H., Koster, H., Matthes-Schmidt, M., Röbke, B.R., Willershäuser, T., Reicherter, K. (2018c): Returning to the facts: Response to the refusal of tsunami traces in the ancient harbour of Lechaion (Gulf of Corinth, Greece) by 'non-catastrophists' – Reaffirmed evidence of harbour destruction by historical earthquakes and tsunamis in AD 69–79 and the 6th cent. AD and a preceding pre-historical event in the early 8th cent. BC. – Zeitschrift für Geomorphologie N.F. **61 (4)**, in press, doi: 10.1127/zfg/2018/0519.

W

Waldbaum, J.C. (1966): Philistine Tombs at Tell Fara and Their Aegean Prototypes. – American Journal of Archaeology **70**: 331-340.

Wartenberg, W. & Freund, H. (2012): Late Pleistocene and Holocene sedimentary record within the Jade Bay, Lower Saxony, Northwest Germany. New aspects for the palaeo-ecological record. – Quaternary International **251**: 31-41.

Wartenberg, W., Vött, A., Freund, H., Hadler, H., Frechen, M., Willershäuser, T., Schnaidt, S., Fischer, P. & Obrocki, L. (2013): Evidence of isochronic transgressive surfaces within the Jade Bay tidal flat area, southern German North Sea coast – Holocene event horizons of regional interest. – Zeitschrift für Geomorphologie **57 (4)**: 229-256.

Wasser- und Schifffahrtsverwaltung des Bundes, Generaldirektion Wasserstrassen und Schifffart (WSV) (2015): Streckenatlas des Main. Teil I von km 0 (Mainmündung) bis km 187 (Staustufe) Rothenfels. – Fachstelle für Geoinformationen Süd (FGS) beim Wasser- und Schifffahrtsamt, pp. 130, Regensburg.

Waters, M. R. (1992): Principles of Geoarchaeology: A North American Perspective. – Universiry of Arizona Press, pp. 398, Tucson.

Wawrzinek, C. (2014): In portum navigare. Römische Häfen an Flüssen und Seen. – De Gruyter, pp. 517, Berlin.

Weltje, G.J. & Tjallingii, R. (2008): Calibration of XRF core scanners for quantitative geochemical application. – Earth and Planetary Science Letters **274**: 423-438.

Werban, U., Leven, C., Reboulet, E., Leccese, M., Viotti, P. & Dietrich, P. (2007): Technologies for fast characterization of subsurface structures – An example from the Milano-Rho site. – Italian Journal of Engineering Geology and Environment **1**: 115-122.

Werner, V., Baika, K., Fischer, P., Hadler, H., Obrocki, L., Willershäuser, T., Tzigounaki, A., Tsigkou, A., Reicherter, K., Papanikolaou, I., Emde, K. & Vött, A. (2018a): The

sedimentary and geomorphological imprint of the AD 365 tsunami on the coasts of southwestern Crete (Greece) – Examples from Sougia and Palaiochora. – Quaternary International **473**: 66-90.

Werner, V., Baika, K., Tzigounaki, A., Reicherter, K., Papanikolaou, I., Emde, K., Fischer, P. & Vött, A. (2018b): Mid-Holocene tectonic geomorphology of northern Crete deduced from a coastal sedimentary archive near Rethymnon and a Late Bronze Age Santorini tsunamite candidate. – Geomorphology **326**: 167-189.

Willershäuser, T., Vött, A., Hadler, H., Henning, P. & Ntageretzis, K. (2012): Evidence of high-energy impact near Kato Samiko, Gulf of Kyparissia (western Peloponnese, Greece), during history. – Bremer Beiträge zur Geographie und Raumplanung **44**: 26-36.

Willershäuser, T., Vött, A., Hadler, H., Fischer, P., Röbke, B.R., Ntageretzis, K., Emde, K. & Brückner, H. (2015a): Geo-scientific evidence of tsunami impact in the Gulf of Kyparissia (western Peloponnese, Greece). – Zeitschrift für Geomorphologie N.F., Supplementary Issue **59 (4)**: 43-80.

Willershäuser, T., Vött, A., Hadler, H., Ntageretzis, K., Emde, K. & Brückner H.(2015b): Holocene palaeotsunami imprints in the stratigraphical record and the coastal geomorphology of the Gialova Lagoon near Pylos (southwestern Peloponnese, Greece). – Zeitschrift für Geomorphologie N.F., Supplementary Issue **59 (4)**: 15-252.

Witten, A.J. (2014): Handbook of Geophysics and Archaeology. Routlege, pp. 320, New York.

Wolf, D. & Faust, D. (2016): River braiding caused by rapid floodplain deformation – Insights from Holocene dynamics of the Jarama River in central Spain. – Quaternary International **407**: 126-139.

Wolff, G. (1903): Das Kastell Groß-Krotzenburg. – Der Obergermanisch-Raetische Limes des Roemerreiches, Heidelberg.

Wolff, G. (1929): Ziegelstempel als wichtige Denkmäler für die Chronologie der römischen Militärstationen im nördlichen Limesgebiete. Germania. – Korrespondenzblatt der Römisch-Germanischen Kommission des Deutschen Archäologischen Instituts **3**: 113-126.

Wright, J. (2008): Chamber Tombs, Family, and State in Mycenaean Greece. – In: Gallou, C., Georgiadis, M. & Muskett G. M. (eds.): Dioskouroi. Studies presented to W. G. Cavanagh and C. B. Mee on the anniversary of their 30-year joint contribution to Aegean Archaeology. – BAR-IS 1889, pp. 144-153, Oxford.

Wunderlich, J., Herbig, C., Marinova, E., Nowacki, D. & Röpke, A. (2012): Landschafts- und Flussgeschichte der unteren Donau im Umfeld des Siedlungshügels Magura Gorgana, Südrumänien. In: Stobbe, A. & Tegtmeier, U. (eds.): Verzweigungen. Eine Würdigung für A.J.Kalis und J. Meurs-Balke. Habelt Verlag, pp. 333-550, Bonn.

Wunderlich, J. (2007): Archive in Geographie und Geowissenschaften. In: Gebhardt, H. Glaser, G., Radtke, U. & Reuber, P. (eds.): Geographie. Physische Geographie und Humangeographie. Springer, pp. 549, München.

Wunderlich, T., Petersen, H., Attia al Hagrey, S. & Rabbel, W. (2013): Pedophysical models for resistivity and permittivity of partially water-saturated soils. – Vadose Zone Journal **12 (4)**: 1-14.

Wunderlich, T., Fischer, P., Wilken, D., Hadler, H., Erkul, E., Mecking, R., Günther, T., Heinzelmann, M., Vött, A. & Rabbel, W. (2018a): Constraining electrical resistivity tomography by direct push electrical conductivity logs and vibracores: An examplary study of the Fiume Morto silted Riverbed (Ostia Antica, Westerm Italy). – Geophysics **83**: B87-B103.

Wunderlich, T., Wilken, D., Erkul, E., Rabbel, W., Vött, A., Fischer, P., Hadler, H. & Heinzelmann, M. (2018b): The river harbour of Ostia Antica – stratigraphy, extent and harbor infrastructure from combined geophysical measurements and drillings. – Quaternary International **473 A**: 55-65.

X

Y

Z